LAVA FLOW FIELD EMPLACEMENT STUDIES OF MAUNA ULU (KILAUEA VOLCANO, HAWAI'I, USA) AND VENUS, USING FIELD AND REMOTE SENSING ANALYSES

by

Jeffrey Myer Byrnes

B.A., Case Western Reserve University, 1996

Submitted to the Graduate Faculty of

Arts and Sciences in partial fulfillment

of the requirements for the degree of

Doctor of Philosophy

University of Pittsburgh

2002

UNIVERSITY OF PITTSBURGH

FACULTY OF ARTS AND SCIENCES

This dissertation was presented

by

Jeffrey Myer Byrnes

It was defended on

July 15, 2002

and approved by

David A. Crown (Chairman)

Michael S. Ramsey

Ellen R. Stofan

William Harbert

William A. Cassidy

LAVA FLOW FIELD EMPLACEMENT STUDIES OF MAUNA ULU (KILAUEA VOLCANO, HAWAI'I, USA) AND VENUS, USING FIELD AND REMOTE SENSING ANALYSES

Jeffrey Myer Byrnes, Ph.D.

University of Pittsburgh, 2002

This work examines lava emplacement processes by characterizing surface units using field and remote sensing analyses in order to understand the development of lava flow fields. Specific study areas are the 1969-1974 Mauna Ulu compound flow field, (Kilauea Volcano, Hawai'i, USA), and five lava flow fields on Venus: Turgmam Fluctus, Zipaltonal Fluctus, the Tuli Mons/Uilata Fluctus flow complex, the Var Mons flow field, and Mylitta Fluctus.

Lava surface units have been examined in the field and with visible-, thermal-, and radar-wavelength remote sensing datasets for Mauna Ulu, and with radar data for the Venusian study areas. For the Mauna Ulu flow field, visible characteristics are related to color, glass abundance, and dm- to m-scale surface irregularities, which reflect the lava flow regime, cooling, and modification due to processes such as coalescence and inflation. Thermal characteristics are primarily affected by the abundance of glass and small-scale roughness elements (such as vesicles), and reflect the history of cooling, vesiculation and degassing, and crystallization of the lava. Radar characteristics are primarily affected by unit topography and fracturing, which are related to flow inflation, remobilization, and collapse, and reflect the local supply of lava during and after unit emplacement. Mauna Ulu surface units are correlated with pre-eruption

topography, lack a simple relationship to the main feeder lava tubes, and are distributed with respect to their position within compound flow lobes and with distance from the vent.

The Venusian lava flow fields appear to have developed through emplacement of numerous, thin, simple and compound flows, presumably over extended periods of time, and show a wider range of radar roughness than is observed at Mauna Ulu. A potential correlation is suggested between flow rheology and surface roughness. Distributary flow morphologies may result from tube-fed flows, and flow inflation is consistent with observed surface characteristics. Furthermore, the significance of inflation at Mauna Ulu and comparison of radar characteristics indicates that inflation may, in fact, be more prevalent on Venus than at Mauna Ulu. Although the Venusian flow fields display morphologies similar to those observed within terrestrial flow fields, the Venusian flow units are significantly larger.

Acknowledgements

I would foremost like to thank my advisor and committee chair, David Crown, for filling those two roles particularly well and for supporting me financially, intellectually, and academically throughout my graduate career. I am also thankful to the remainder of my dissertation committee, Mike Ramsey, Ellen Stofan, Bill Harbert, and Bill Cassidy, who have each contributed to my education and improved the quality of this dissertation. I would additionally like to acknowledge feedback received from Ed Lidiak and Bruce Hapke, who had both sat on earlier committees.

I appreciate all of the guidance and assistance with field observations and interpretations that I received from David, Mike, Scott Rowland, Puna Steve Anderson, and Brian Banks. I also highly value the opportunities that I have had to broaden my field experience that have been provided by Ralph Harvey and Mark Bulmer.

Additionally, this work has significantly benefited from scientific discussions and input from Jeff Plaut, Bruce Campbell, Tracy Gregg, Steve Baloga, Lori Glaze, and Misha Kreslavsky. Substantial technical assistance is appreciated from Sarah B.Z. McElfresh, Chris Eisinger, Duncan Young, Rick Wessels, Jen Piatek, Ellen O'Leary, and Tamara Misner, without which much of this work could not have been accomplished. I am also grateful to Darcy Hu of Hawai'i Volcanoes National Park for expediting sample permits, as well as Gordon, JoAnn, and Ki'i Morse at My Island B&B for accommodations during field research expeditions.

My graduate career has been enriched with additional academic input and support from many sources, especially Scott Mest, Tim Pierce, and Amy Snyder Hale. Significant administrative support from T.J. Lipple, Dolly Chavez, Philippa Carter, Candy Weller, and Todd

Bowers is also appreciated. Support from the Andrew W. Mellon Foundation is gratefully acknowledged, as is support from the National Aeronautics and Space Administration in the form of fellowships from the Pennsylvania Space Grant Consortium as well as grants NAG5-4037 and NAG5-10561 from the Planetary Geology and Geophysics Program to David Crown.

I am deeply grateful to Janette Steets for her patience and support, and for helping me maintain a certain level of sanity. Thanks also to the greater Skankin' Homer family, who provided entertainment away from academics and helped me maintain a certain level of insanity. I am also very appreciative of all of my other friends and family that have provided support, especially John Byrnes; Amy, Jessie, and Roscoe Crown; Jon Chase and Tiffany Knight; and Brian Seese and Kari Brandon. Lastly and leastly, I would like to thank the makers of chocolate milk, who helped to sustain me through this process.

TABLE OF CONTENTS

LIST OF TABLES

LIST OF FIGURES

Chapter 1

Introduction

Volcanism is the fundamental process in the solar system responsible for creating the surfaces of terrestrial bodies [e.g. BVSP, 1981; Francis, 1993]. Understanding the processes responsible for producing volcanic deposits is one of the principal goals of volcanology. This dissertation presents an examination of lava emplacement processes that have been completed in order to understand the development of lava flow fields in different planetary settings, accomplished through the detailed characterization of surface units. The specific study areas are the 1969-1974 Mauna Ulu compound flow field, located on the upper East Rift Zone of Kilauea Volcano (Hawai'i, USA), and five lava flow fields on Venus: Turgmam Fluctus, Zipaltonal Fluctus, the Tuli Mons/Uilata Fluctus flow complex, the Var Mons flow field, and Mylitta Fluctus. This introductory chapter provides an overview of the structure and content of the dissertation.

Chapter 2 presents an examination of the relationships between pahoehoe surface units, topography, and lava tubes within an initial study area at Mauna Ulu, originally published in the Journal of Geophysical Research [Byrnes and Crown, 2001]. It is reproduced herein by permission of American Geophysical Union. This study delineated varieties of tube-fed pahoehoe units that were identified in the field and described based on color, surface texture, and morphology. The units were mapped using high-resolution aerial photographs with an automated supervised classification technique. The distribution of units was then analyzed using Geographical Information Systems (GIS) analyses.

Chapter 3 extends the initial study both spatially and spectrally in order to cover the full range of surface units present within the Mauna Ulu flow field and incorporate the thermal-

infrared region of the electromagnetic spectrum. The study was accomplished through additional detailed field characterizations and analysis of recently acquired ASTER (Advanced Spaceborne Thermal Emission and Reflection Radiometer) and MASTER (MODIS/ASTER airborne simulator) datasets (MODIS is the Moderate Resolution Imaging Spectroradiometer). This work has been submitted to the Journal of Volcanology and Geothermal Research special issue "Volcanic Observations from Space: New Results from the EOS Satellite Instruments" [Byrnes et al., 2002].

Chapter 4 is an examination of the morphology, stratigraphy, and surface roughness properties of five Venusian lava flow fields. This study provides a contrast to the Mauna Ulu flow field, representing lava flow fields emplaced in a different planetary surface environment. Turgmam Fluctus, Zipaltonal Fluctus, the Tuli Mons/Uilata Fluctus flow complex, the Var Mons flow field, and Mylitta Fluctus represent the most recent resurfacing locally within the extensive Venusian plains (based on cross-cutting and superposition relationships) and display gross lava flow morphologies that are similar to terrestrial lava flows in many respects. This study is currently in press in the Journal of Geophysical Research – Planets [Byrnes and Crown, 2002]. It is reproduced herein by permission of American Geophysical Union.

Chapter 5 presents a radar analysis of the Mauna Ulu flow field that complements the visible- and thermal-wavelength characterizations presented in chapters 2 and 3 and provides a means to compare the Mauna Ulu flow field to the five Venusian lava flow fields examined in chapter 4. More generally, this study provides constraints on the types of interpretations that may reasonably be made using Magellan radar data to understand volcanism using radar data. This chapter is intended to serve as the basis for a manuscript to be submitted for publication.

Chapter 6 provides a synopsis of these examinations of lava flow field emplacement processes. Main conclusions of this research program and potential directions for future research are discussed.

Chapter 2

Relationships between pahoehoe surface units, topography, and lava tubes at Mauna Ulu

2.1. Introduction

Hawaiian volcanism produces two main types of lava flows: simple and compound [Walker, 1972]. Simple lava flows have single lobes or branch into a few main lobes and are typically characterized by 'a'a surface textures. Compound lava flows are emplaced in multiple overlapping and interfingering lobes that typically display pahoehoe textures. Pahoehoe lava flows are an important component of Hawaiian volcanism, comprising 81% of the surface of Kilauea Volcano [Holcomb, 1987], the youngest of the subaerial Hawaiian volcanoes. A detailed understanding of pahoehoe flow emplacement is necessary to provide constraints for modeling flow field development for accurate volcanic hazard assessment and remediation and may provide insight to lava flow emplacement in other planetary environments.

The overall objective of this research is to determine the factors governing the emplacement of compound lava flow fields, which are represented by complex patterns of surface units. The distribution and relationships between surface units reflect local emplacement conditions (i.e., lava rheology, cooling rate, flow rate, and underlying topography) within the flow field and thus provide critical information on flow field development. This study is an examination of surface units found within the Mauna Ulu flow field using remote sensing, field observations, and Geographical Information Systems (GIS) applications. The use of remotely acquired data sets significantly increases the ability to fully document the nature and variability of flow field surfaces. The Mauna Ulu pahoehoe surface units identified in this study exhibit dominant surface and morphologic characteristics that are indicative of different flow

emplacement processes; the relationship of these units to lava tubes and the pre-Mauna Ulu topography is analyzed to determine the degree to which surface unit distribution is controlled by these factors.

2.2. Background

The emplacement of compound flow fields is complex due to significant variations in emplacement processes with distance from the vent and over the duration of activity. These variations produce a wide range of textures, morphologies, and sizes for individual pahoehoe flow units. Swanson [1973] identified three intergradational pahoehoe types that illustrate the spatial variability of flows from the 1969-1971 Mauna Ulu eruptive sequence. High fountaining allowed significant degassing of lava, producing smooth-surfaced pahoehoe immediately adjacent to the vent. Lava that overflowed the lip of the vent and experienced minimal degassing prior to emplacement formed two varieties of shelly pahoehoe. Where the local topographic relief was greater than ~1 m, flow rates were relatively high and shelly pahoehoe took an amoeboid form, with large interior void spaces due to exsolution of volatiles. Local relief less than ~1 m caused lower flow velocities, resulting in a sheet flood morphologic variety characterized by folding of the crust followed by draining of the flow interior. Medial and distal portions of the Mauna Ulu flow field were found to be composed of dense, hummocky pahoehoe that was transported beneath the flow surface through a network of lava tubes from the vent to the flow front [see also Greeley, 1971; Peterson and Swanson, 1974; Holcomb, 1976, 1987]. Wilmoth and Walker [1993] characterized two types of tube-fed pahoehoe in the Mauna Ulu and Kupaianaha flow fields based on vesicle characteristics. S-type (spongy) pahoehoe [see also

Walker, 1989] is characterized by selvages (outer ~6 cm) that contain abundant, small, and approximately spherical vesicles. Vesicles typically comprise >40 vol % of the lava, and most are <4 mm in diameter. During and immediately following the emplacement of spongy pahoehoe, the uppermost portion of the glassy crust has been observed to spall off in flakes. P-type (pipe-vesicle bearing) pahoehoe [see also Philpotts and Lewis, 1987; Walker, 1987; Godinot, 1988] is less common and less vesicular, has a lower porosity and larger vesicles, and displays pipe vesicles near the base of each flow unit. P-type pahoehoe commonly displays a glassy crust, as spallation occurring during and immediately following emplacement is negligible. Differences between the two lava types result from P-type pahoehoe experiencing a longer storage time within the lava tube system, resulting in a greater degree of bubble coalescence and volatile loss prior to emplacement.

Studies of active flow fields show that the relative proportion of lava transported as surface flows versus that transported through tubes is variable over the time of flow field emplacement [Greeley, 1971; Moore et al., 1973; Swanson et al., 1979; Tilling et al., 1987]. Surface activity associated with breakouts from tubes typically increases with increased supply from the vent and also increases following eruptive pauses during which the tube system becomes clogged with collapsed material [Tilling et al., 1987; Kauahikaua et al., 1998]. Hon et al. [1994] observed that pahoehoe lobe morphologies may also change with time through the processes of coalescence and inflation [see also Walker, 1991; Cashman and Kauahikaua, 1997; Anderson et al., 1999]. Pahoehoe toes that are emplaced individually may coalesce with other toes to form broad, flat sheets; evidence of this is preserved in some localities where subdued ropes and partial toe margins are preserved on the surfaces of sheets [Byrnes and Crown, 1998]. Inflation, vertical growth due to continued influx of lava beneath the surface crust, is most

significant in portions of the flow field that have relatively horizontal (<2°) underlying slopes but occurs to various extents throughout the medial and distal portions of a flow field [Swanson, 1973; Hon et al., 1994]. Inflation at relatively small scales produces cracks and offsets in sheets and tilted slabs of surface crust in toey lobes. Pahoehoe flow fields also display tumuli, which are roughly domical inflation features typically several meters high and meters to tens of meters wide [Walker, 1991; Rossi and Gudmundsson, 1996; Anderson et al., 1999].

Primary pahoehoe morphologies include sheets, toes, and channels (Figure 2.1). These morphologies are indicative of local flow emplacement rate, which is influenced by local topography, rheology, and supply [Macdonald, 1953; Wentworth and Macdonald, 1953; Jones, 1968, 1969; Walker, 1972; Swanson, 1973; Swanson et al., 1979; Tilling et al., 1987; Hon et al., 1994; Keszthelyi and Denlinger, 1996; Kilburn, 1996; Crown et al., 1998; Crown and Baloga, 1999]. Broad, flat sheets occur where emplacement is unconfined, or may result from the coalescence and inflation of toes and/or small sheets. For example, Swanson [1973] observed that where amoeboid shelly pahoehoe encountered more subdued topography, it coalesced to form the sheet-flood variety. Hon et al. [1994] observed that toes on near-horizontal surfaces coalesce and are subject to subsequent inflation that subdues relief at toe margins. Pahoehoe toes form as discrete units due to breakouts of small volumes of lava; interconnected networks of pahoehoe toes form small to intermediate lobes. Crown and Baloga [1999] related toe network morphologies to local flow conditions and also showed that toes are gradational to small channels and sheets with higher local flow rates. Channels form when local flow rates are sufficiently high. For example, Greeley [1971] noted that channels (and subsequent lava tubes) formed within the zones of highest flow velocity in the Mauna Ulu flow field.

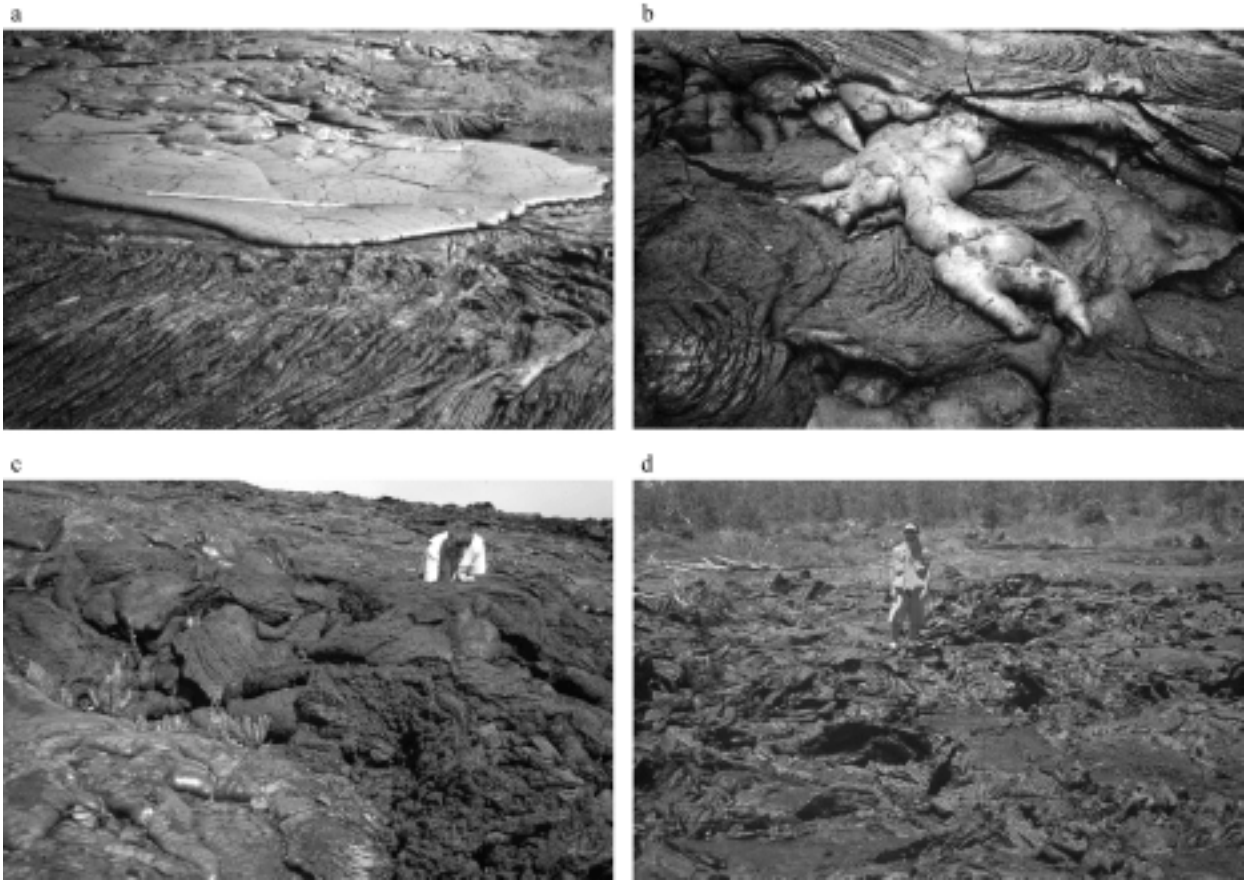

Figure 2.1. Examples of the four pahoehoe units defined in this study, exhibiting characteristic pahoehoe morphologies. (a) Mauna Ulu sheet of unit I (center) which grades (upflow) into coalesced toes (unit II, top), all of which overly a ropy channel (unit IV, bottom). Measuring rod on sheet is 2 m long. (b) Bright, glassy-surfaced toes of unit II extend from channel (top) and contrast with the underlying, darker surface. Scene is ~4 m across. (c) Rough breakout of unit III emanates from inflation feature above Holei Pali. Scene is ~7 m across. (d) Highly disrupted unit IV surface, located above Holei Pali. Scene is ~8 m across. See text for descriptions of units I-IV.

Pahoehoe surfaces may display ropy and slabby textures that result from deformation of the active, cooling surface. These textures are gradational to a clinkery 'a'a texture through changes in viscosity and rate of shear strain [Peterson and Tilling, 1980]. Other transitional pahoehoe textures include rough pahoehoe [Rowland and Walker, 1988] as well as toothpaste lava [Rowland and Walker, 1987], which is characterized by a high viscosity, a low volumetric flow rate, and a spinose surface containing longitudinal grooves and ridges (equivalent to "spiny pahoehoe" of Peterson and Tilling [1980]).

Secondary pahoehoe morphologies may result from remobilization and fracturing of a solidified pahoehoe crust, typically resulting in tilted, jumbled, and/or imbricated plates that preserve some of the original pahoehoe surface. Such morphologies have been described by Wentworth and Macdonald [1953] (slab pahoehoe) and Peterson and Tilling [1980] (suddenly activated 'a'a).

Flow fields display emplacement units over a range of scales from small toes to large channel and tube systems. On the basis of measurements of sizes and orientations of individual pahoehoe features, recent analyses indicate that toes (tens to hundreds of centimeters) are gradational to small channels and sheets (1 to tens of meters) [Crown and Baloga, 1999] and that emplacement processes within pahoehoe flows exhibit scale-dependent tendencies [Crown et al., 1998, 1999]. Orientations of pahoehoe features (i.e., toes and channels) within the Mauna Ulu flow field display greater variability at small scales. Within a given local network these features may occur at high angles to the overall downflow direction defined by the path from the vent to the flow field terminus. The increased variability in flow orientation at smaller scales is due to the higher relative variability in topography at the scale of toes compared to channels [Crown et

al., 1998, 1999]. Earlier studies had suggested that pahoehoe flow emplacement is fractal in nature based on measurements of flow margins [Bruno et al., 1992, 1994].

2.3. Study Area

The study area is within the Mauna Ulu flow field on the east rift zone of Kilauea Volcano (Figure 2.2). The Mauna Ulu satellitic shield was built during a period of prolonged volcanic activity from May 1969 to June 1974, and was extensively documented [Moore et al., 1973; Swanson, 1973; Holcomb, 1976, 1987; Swanson et al., 1979; Tilling et al., 1987]. Lava extruded during the Mauna Ulu eruptions built a 120-m-high shield, covered 61 km^2 of Kilauea's south flank and added 0.1 km^2 of new land along the coast [Holcomb, 1976, 1987]. Volcanic activity took place in two eruptive sequences, the first lasting from May 24, 1969, to October 15, 1971, and the second occurring from February 3, 1972, to July 22, 1974. At that time, these eruptions were the longest period of nearly continuous rift zone activity documented at Kilauea Volcano [Tilling et al., 1987]. Flows from the first Mauna Ulu sequence formed a compound flow field with two main branches that flowed over a series of pali (cliffs) and reached the coast at several points near Kahue Point [Swanson et al., 1979]. The second phase of eruptive activity widened the flow field by emplacing additional compound flows that overlap the outer margins of the previous flows and which reached the coast near Apua Point and Kaena Point [Tilling et al., 1987].

The current study focuses on an area within the Mauna Ulu flow field covering 6.16 km^2 on and below Holei Pali, 7 to 9 km from the Mauna Ulu vent. The study area contains pahoehoe

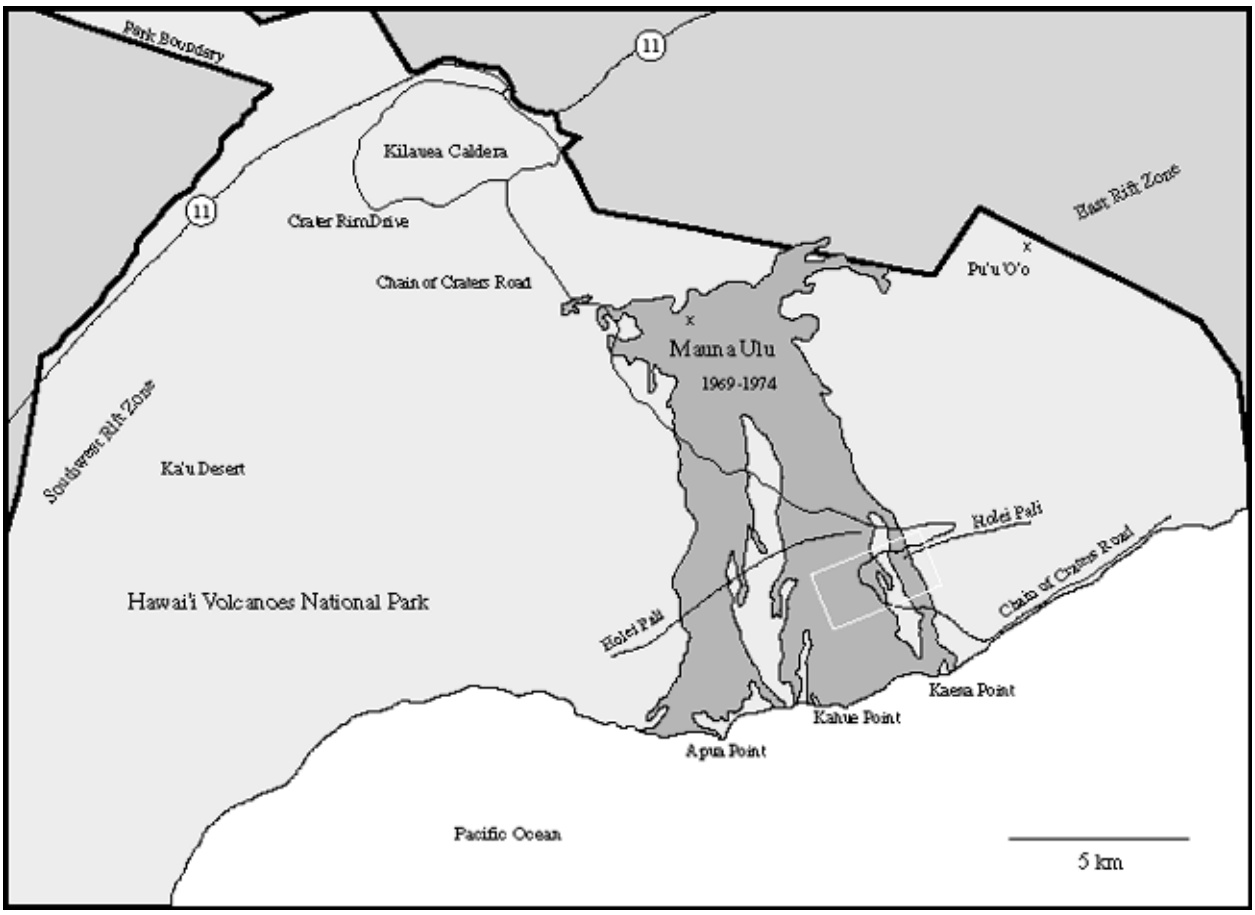

Figure 2.2. Sketch map showing the location of Mauna Ulu on the east rift zone of Kilauea Volcano and the extent of lava flows emplaced during the 1969-1974 eruptions. Study area is indicated by the white box.

that was mapped by Holcomb [1976] as tube-fed lava emplaced during 1970-1972. The flow field surface here is composed primarily of pahoehoe (classified as dense, hummocky pahoehoe by Swanson [1973]); distinct lobes of channel-fed 'a'a are also present.

2.4. Analysis of Mauna Ulu Pahoehoe Surface Units

Color high-resolution aerial photographs (Figure 2.3), taken during acquisition of NASA airborne NS001 (Landsat thematic mapper simulator) and Thermal Infrared Multispectral Scanner (TIMS) data in April 1985, were analyzed to determine the occurrence and distribution of pahoehoe surface units in the study area at Mauna Ulu. Preliminary classes of pahoehoe units were identified and mapped at approximately 1:4100 scale based on color variations evident in the aerial photographs. These preliminary maps were field checked to determine the meaning of the color variations and the accuracy of the mapping. Several localities were selected in the aerial photographs that display multiple units within close proximity to each other. Field observations were made of the dominant morphologies of, and contact relationships between, units. These observations indicate that the units delineated using the high-resolution aerial photographs represent flow units readily observable on the ground. Most importantly, these units represent different emplacement conditions, as reflected in their preserved flow morphologies and surface textures. On the basis of analysis of the aerial photographs and field observations, four pahoehoe surface units have been defined within the study area that are distinguished based on color, surface texture (roughness and presence or lack of glassy crust), and morphology (Figure 2.1). Additionally, these four units have characteristic morphologies,

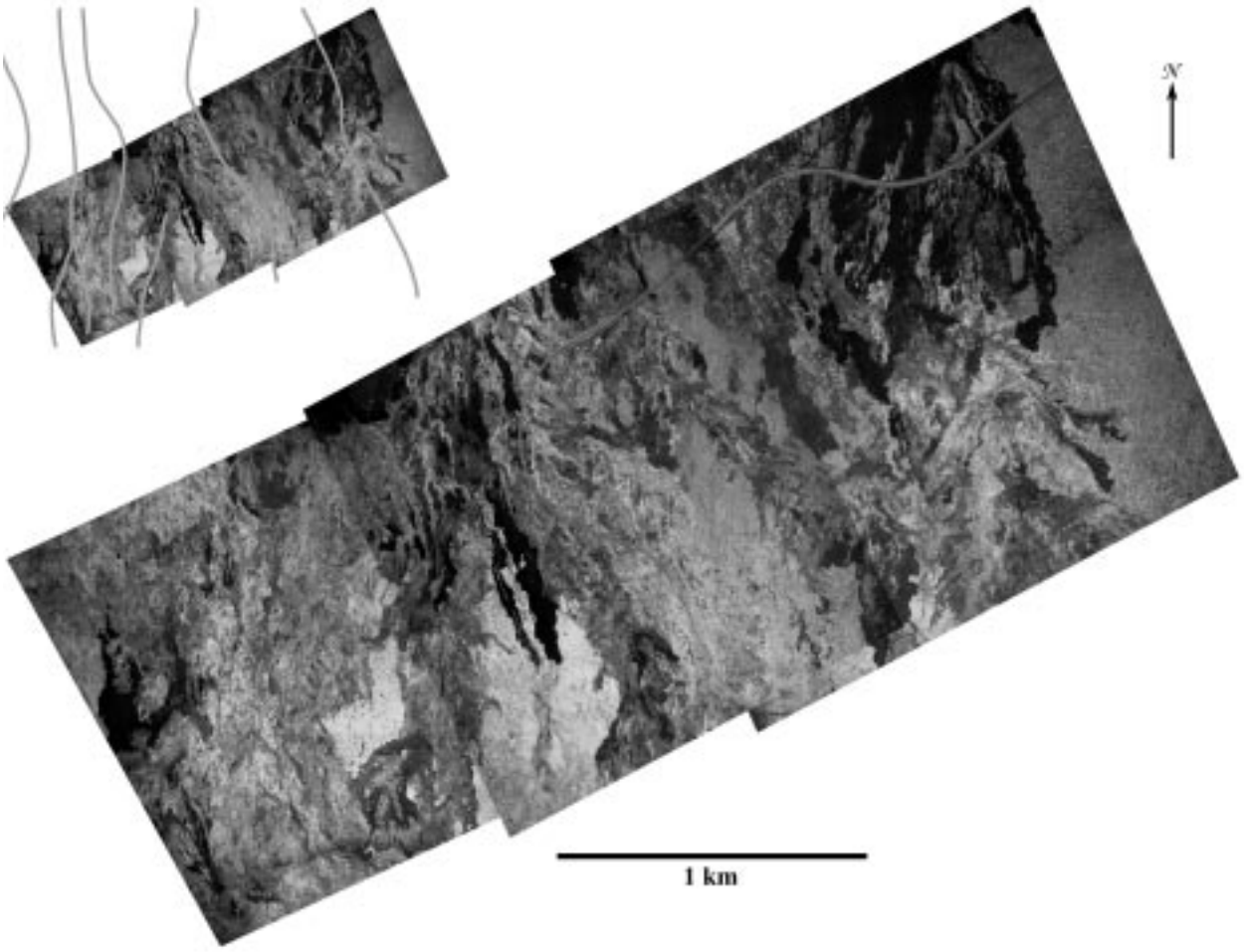

Figure 2.3. Mosaic of high-resolution color aerial photographs of the Mauna Ulu study area (shown in black and white) acquired in conjunction with airborne NS001 and TIMS data, April 1985 (frames 038, 040, and 042). Chain of Craters Road is visible winding through a portion of the study area. Inset shows the location of major tube segments mapped by Holcomb [1976].

orientations and scales that are a function of emplacement conditions (see following sections and Crown et al. [1998] and Crown and Baloga [1999]).

2.4.1. Description of Mauna Ulu Pahoehoe Units

Unit I (Figure 2.1a) typically consists of multiple adjacent pahoehoe sheets and displays few visible discrete toes in interior zones of the unit. Unit margins are primarily lobate and exhibit both discrete toes and smaller sheets. Unit I surfaces are smooth, have a bronze color, and possess a highly reflective glassy crust that is generally flat, although a subdued ropy texture is preserved in some areas. This unit appears white to mottled in the aerial photographs. These sheets commonly form through the coalescence of toes and smaller sheets whose margins become subdued due to inflation of the flow. Alternatively, sheets with flatter upper surfaces (lacking subdued toe margins) may be emplaced as primary flow units due to unconfined flow at relatively high rates over a smooth substrate. This type of unit I sheet occurrence is not as common within the study area as sheets that form due to coalescence of smaller features. Unit I lobes are typically up to a few tens of meters across, have lengths comparable to widths, and appear to have no preferred long-axis orientation relative to the overall downflow direction of the Mauna Ulu flow field.

Unit II (Figure 2.1b) is composed of networks of pahoehoe toes, including both smooth-surfaced and ropy-surfaced toes. Unit II surfaces have a light gray, mottled appearance in the aerial photographs. These toe networks display the same type of bronze glassy surface crust as unit I sheets, although the greater number and better definition of toes result in a more irregular upper surface. Unit II toe networks typically are 1 to tens of meters in length and have digitate margins. Within toe networks, branching occurs in the downflow and lateral directions with

little to no vertical superposition of toes within the active lobe [Crown and Baloga, 1999]. In some localities these toe networks display a weak preferred orientation downflow (i.e., long-axis roughly parallel to the overall downflow direction).

Units I and II are typically spatially associated with each other. These units are gradational at sheet margins, which tend to be toey due to decreased flow rate and less inflation (Figure 2.1a). They are also gradational over larger areas, with unit I sheet exposures reflecting an increased degree of local coalescence and/or inflation that causes toe margins to lose definition and decimeter-scale topography to become subdued. These reported small-scale effects of coalescence and inflation within the Mauna Ulu flow field are supported by observations of toe and sheet coalescence within the active Pu'u 'O'o flow field. Previous investigators have also reported the effects of coalescence and inflation of pahoehoe units [Swanson, 1973; Hon et al., 1994]. Local occurrences of ropy texture on flat areas of sheet surfaces are presumably sites where lava was initially emplaced as discrete toes. The gradational nature of the smooth glassy surfaces of units I and II creates a mottled appearance in some locales within the aerial photographs.

Unit III (Figure 2.1c) is also composed of networks of toes, but these toes lack a smooth glassy crust, commonly display ropy textures, and are rough on the millimeter scale due to vesicles exposed at the surface. Exposures of this unit are typically <10 m long, have lengths generally no more than a factor of 2 greater than widths, and appear to have no preferred orientation relative to the whole flow field. Margins tend to be sinuous, and the toe networks usually display a centrally ridged morphology, with significant vertical superposition within the emplacement network [Crown and Baloga, 1999]. Unit III appears medium gray in the aerial photographs. Unit III toe networks typically occur as breakouts from cracks in inflated portions

of other units and are the last stage of local flow emplacement. The unit most likely represents lava that was subjected to significant subsurface storage within the flow field prior to emplacement. The prolonged lava storage is reflected by relatively high viscosity during emplacement, as indicated by toes that tend to be shorter and more equant [Crown and Baloga, 1999] and by a high relative abundance of olivine phenocrysts on unit III surfaces [Byrnes et al., 2000].

Unit IV (Figure 2.1d) typically exhibits elongate channels with highly convoluted and sheared surfaces displaying an abundance of ropes and plates, although any highly disrupted surface displaying primary pahoehoe textures is considered unit IV. These irregular surfaces are rougher on the decimeter to meter scale than surfaces of the other pahoehoe units. Units I and III are gradational to unit IV; with increased flow rate, both units may be disrupted to yield a unit IV morphology. Channels of unit IV are typically <100 m in length, and widths are generally an order of magnitude smaller. These units display a strong downflow orientation. Unit IV surfaces appear dark gray in the aerial photographs, distinguishing unit IV from 'a'a which typically appears black, although these two units are not uniquely identified based strictly on color in the aerial photographs. Field observations show that unit IV exposures preserve abundant smooth pahoehoe textures on pieces up to tens of centimeters across. 'A'a surfaces are considered to be composed exclusively of clinkery textures. Unit IV is typically similar in appearance to the "slab pahoehoe" of Wentworth and Macdonald [1953] (see also "suddenly activated 'a'a" [Peterson and Tilling, 1980]).

It should be noted that typical unit exposure sizes and orientations identified above are based on field observations and are not well represented in the automated classification in which adjacent exposures of the same unit appear the same as a single continuous exposure. All four of

these Mauna Ulu pahoehoe units are classified by Swanson [1973] as dense, hummocky pahoehoe produced from lava tubes. The classification presented herein is based strictly on surface characteristics of the flow units, so the classification of Wilmoth and Walker [1993] that is based on vesicle characteristics is not directly applicable, although all the units are presumably related to S-type lava. P-type pahoehoe has been observed by the authors in the Mauna Ulu flow field, but no P-type pahoehoe has been observed within the study area.

2.4.2. Distribution of Mauna Ulu Pahoehoe Units

In order to classify surface units over the entire study area, the high-resolution color aerial photographs were scanned, georeferenced, and mosaiced. Georeferencing was conducted by identifying features apparent both in the aerial photographs and on the Holcomb [1976] flow map, and measuring the latitude and longitude (to the nearest ~0.4 arc min) on the map. Resampling necessary for the georeferencing (using a linear polynomial rectification with nearest neighbor resampling) yielded rectified images with a resolution of 1 m/pixel. Units were mapped using ERMapper™ with a maximum likelihood enhanced supervised classification. This classification technique utilized training areas selected to distinguish the four pahoehoe surface units and the pre-Mauna Ulu surface, which includes significantly weathered older flows and sparse vegetation (Plate 2.1a). This classification method assigns pixels to a class based on the distance to the mean value (of the training areas) weighted by the covariance matrix of the means. Parts of the classification containing 'a'a, the pre-Mauna Ulu surface, and Chain of Craters Road were masked to eliminate those portions of the scene not relevant to the analysis. Areal extents of the pahoehoe surface units (Table 2.1) were derived from the automated

classification: unit I dominates the study area (48.2% of exposed pahoehoe surfaces), and unit II is the second most abundant (28.0%), followed by unit III (12.9%) and unit IV (10.9%).

Visual inspection of the classification, combined with field observations, indicates the following relationships between the pahoehoe units: (1) Units I and II (glassy-surfaced sheets and toes) constitute the majority of flow field margins, although they may be found anywhere within the flow field. (2) Where unit I margins do not define the edge of the flow field, they primarily contact unit II. (3) Unit III is typically found in the interior of the flow field, presumably because late-stage breakouts are favored in these areas due to the nature of the subsurface distributary network [Hon et al., 1994]. (4) Unit IV is primarily found in interior portions of the flow field; this is attributed to three factors based on field relationships and the classification: (1) channels tend to form in interior portions of the flow field, where flow is concentrated; (2) channels transport lava that is emplaced as other units downflow from channel termini, causing terminal flow field margins to be composed of units I and II; and (3) lateral

Plate 2.1. (following) (a) Automated supervised classification of the study area. Inset shows ~6 m (20 foot) topographic contour data. Note prevalence of unit IV on the pali and dominance of unit I on flatter areas. 'A'a, Chain of Craters Road, and the pre-Mauna Ulu surface have been masked from the classification. (b) Comparison of (left) subscene of aerial photograph with (middle) corresponding maps compiled manually and (right) using the automated classification method. Area of each is 0.06 km^2. North is to the top.

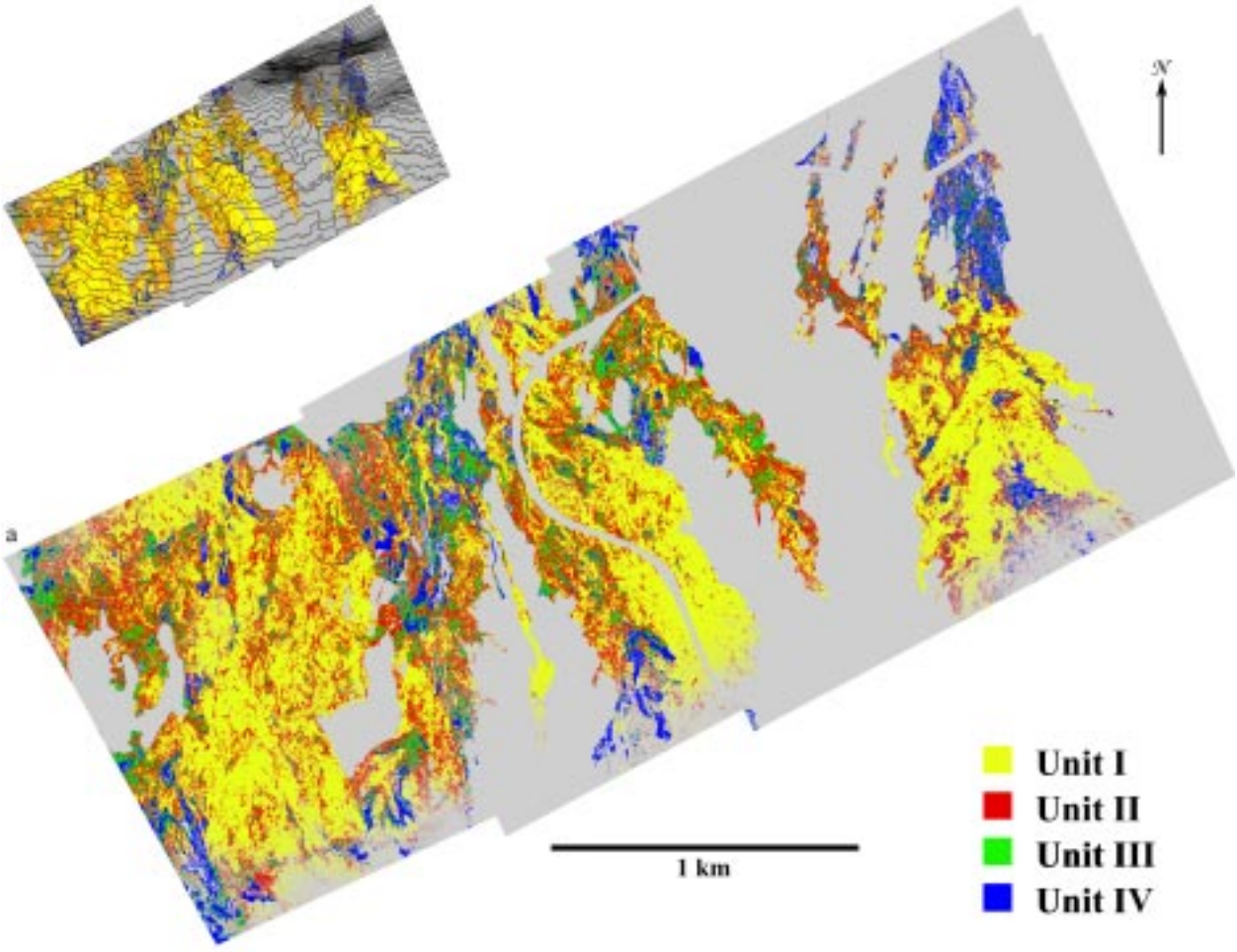
N
a
1 km
Unit I
Unit II
Unit III
Unit IV

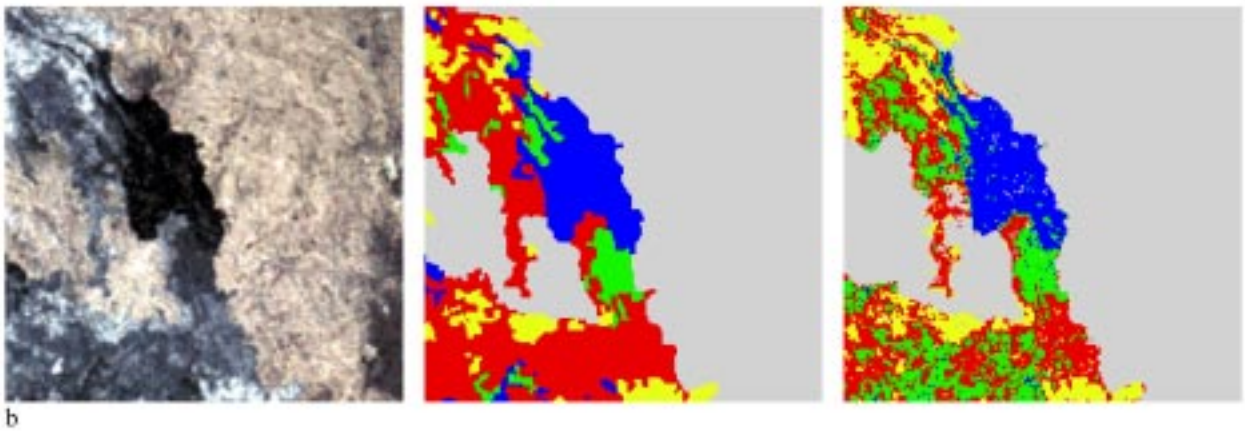
b

Table 2.1. Unit abundance and slope distribution

	Unit I	Unit II	Unit III	Unit IV	whole area
area					
pixels	1,342,821	778,452	358,367	304,726	6,156,447
km^2	1.34	0.78	0.36	0.30	6.16
percent of pahoehoe surfaces	48.2	28.0	12.9	10.9	—
slope data (()					
maximum slope	77.8	77.8	76.6	77.1	78.9
minimum slope	0.0	0.1	0.1	0.1	0.0
mean slope	14.2	15.2	15.9	22.2	19.5
standard deviation of mean	8.4	9.9	10.7	15.3	14.6
standard error on mean	0.007	0.011	0.017	0.028	0.006

overflows and breakouts from channels emplace sheets and/or networks of toes (units I and II) that widen the flow field and thus cause lateral flow field margins to be composed of units I and II.

2.4.3. Relationships to Topography

To assess the effects of slope on the emplacement of pahoehoe surface units, topographic contours representing the pre-Mauna Ulu surface [Holcomb, 1976] were digitized at a ~6 m (20 foot) contour interval. The digitized contours were used to generate a digital elevation model (DEM) in Arc/Info™ [Hutchinson, 1988, 1989, 1996] and calculate slope values over the study area at 1 m/pixel. Slope values were then extracted (using grid mathematics to isolate individual units) for each unit (Figure 2.4). Visual inspection of the topography and classification (Plate

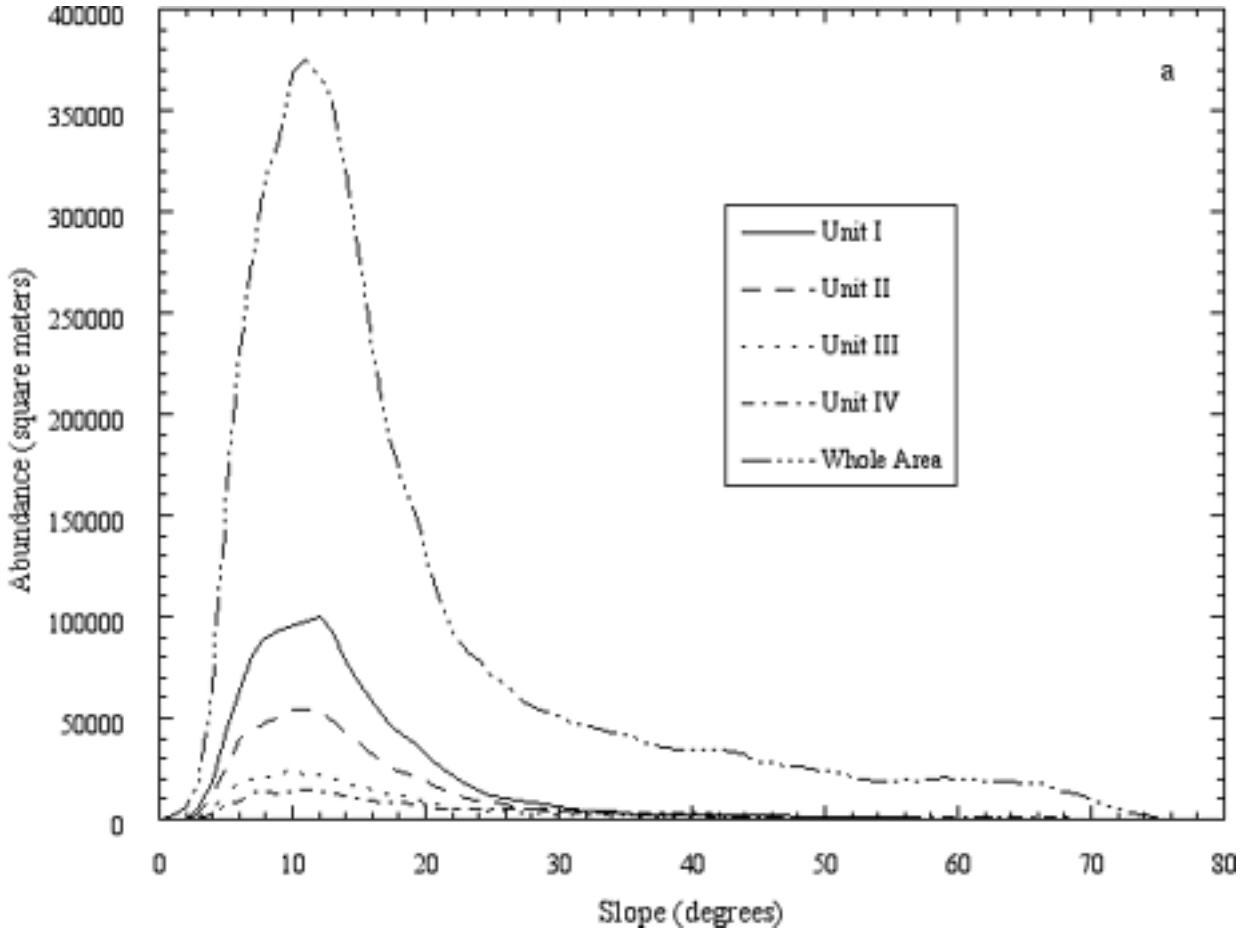

Figure 2.4. Unit abundance as a function of slope. (a) Unit data expressed as areal abundance versus slope, binned to 1° increments. Note the strong dependence on distribution of slopes found within the whole study area. (b) Unit data normalized to whole area data to remove the effects of regional slope abundances. This plot is produced by dividing each unit curve by the whole area curve (from Figure 2.4a).

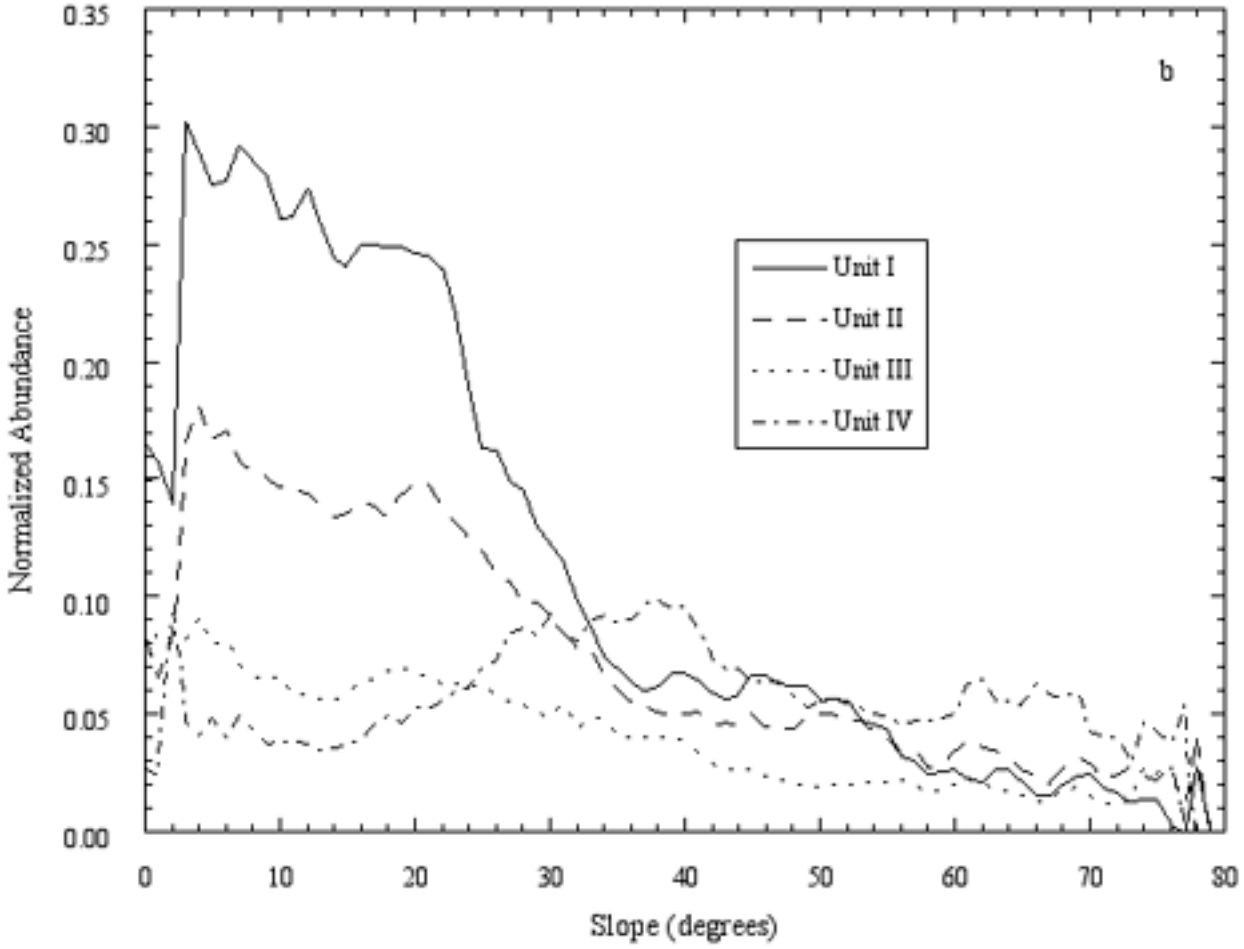

Figure 2.4. (continued)

2.1a) indicates that units I and II occur predominantly on the relatively flat plain below Holei Pali, whereas unit IV primarily occurs on and near the steep pali. Slope statistics are included in Table 2.1. Mean underlying slope values for the four pahoehoe surface units are 14.2 (for unit I), 15.2 (for unit II), 15.9 (for unit III), and 22.2 (for unit IV).

2.4.4. Relationships to Lava Tubes

To assess the relationship between lava tubes and pahoehoe surface units, the major lava tube segments mapped by Holcomb [1976] were digitized. Proportions of each unit within 10, 20, 50, 100, 200, and 500 m of a major lava tube were calculated and compared to the proportions of each unit for the whole study area. The results indicate that surface unit distributions do not vary significantly with distance from the main lava tubes; unit proportions change by an average of only <6% for all measured distances (Figure 2.5).

2.5. Discussion

2.5.1. Unit Classification Techniques

Field observations indicate that the four units distinguished in this study can be mapped reliably using the aerial photographs. This mapping is most difficult in large areas that have undergone inflation, in which precise contacts between unit I sheets and unit II toe networks are sometimes ambiguous in the aerial photographs and in the field. Visual inspection indicates that the automated classification closely reproduces the manual mapping of the pahoehoe surface units in areas that were both mapped using the aerial photographs and field checked. To provide

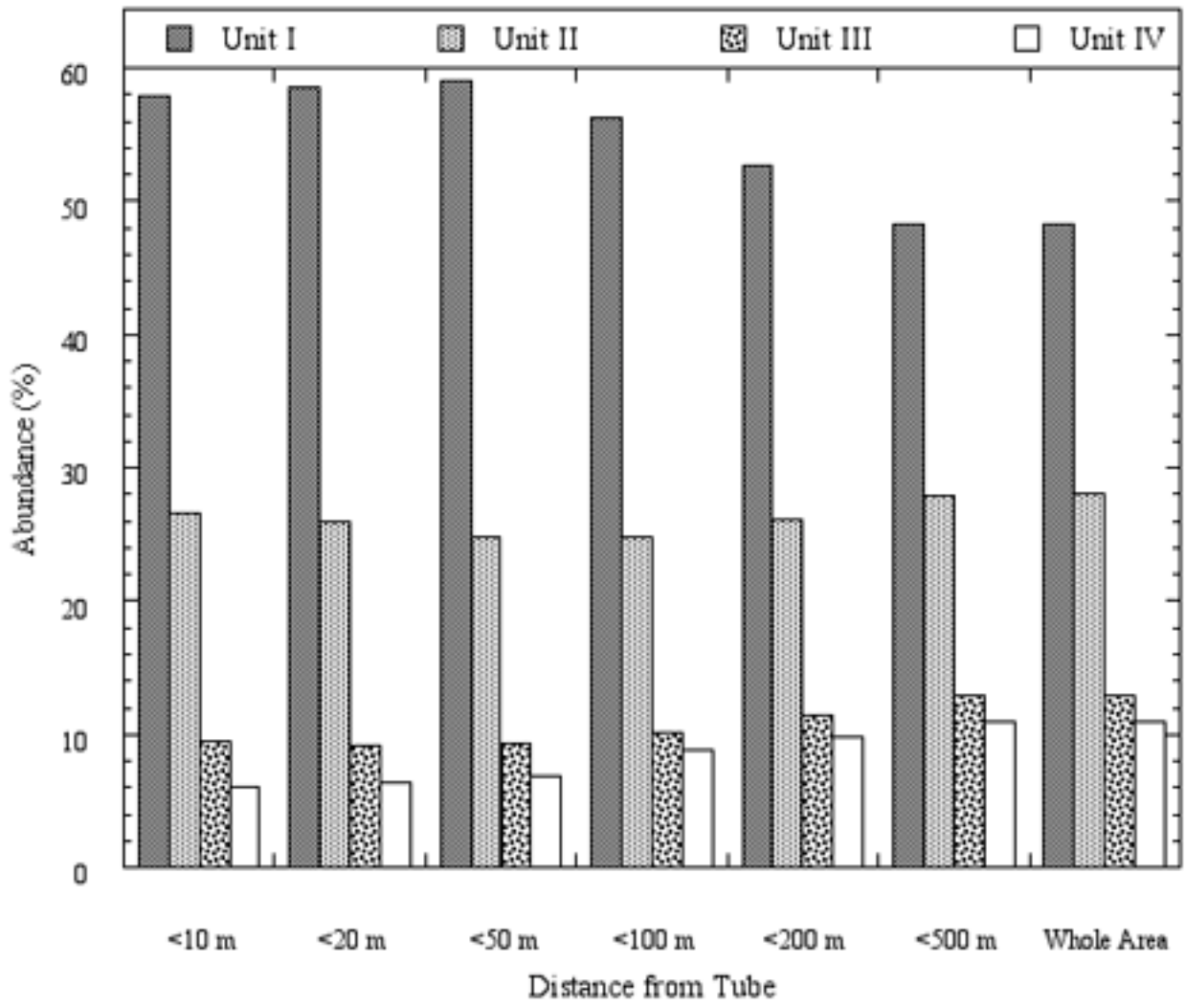

Figure 2.5. Pahoehoe surface unit distribution as a function of distance from the main lava tube segments.

a semiquantitative comparison of the mapping techniques, one portion of the study area (~1% of the automated classification, or ~60,000 pixels) was mapped by hand on the aerial photographs to compare to the automated classification (Plate 2.1b). Proportions of the four pahoehoe units vary by an average of ~10% between the two mapping methods, indicating that the automated classification technique provides a map comparable to that produced by traditional manual mapping.

Because the units are gradational in nature, the precise unit distinctions used in the classification are somewhat arbitrary. Although the classification provides a reasonable representation of the flow field surface, the subscene mapping comparison (Plate 2.1b) illustrates that discrepancies between the mapping techniques are evident and occur as speckle within individual unit exposures. Exposures consisting of various mixtures of units I and II are expected due to the gradational nature of these units and are consistent with field observations. The classification subscene (Plate 2.1b) shows small, irregular occurrences of unit III within a larger exposure of unit II. From the manually produced map it appears that unit III is overrepresented in the classification in this location; field observations confirm this and indicate that color differences alone can not be used to distinguish different types of pahoehoe toe networks in all cases. Speckled lobes consisting of units III and IV are consistent with the transition from unit III to the disrupted surfaces of unit IV observed in the field. Speckled exposures of unit IV and 'a'a were sufficiently problematic that the distribution of 'a'a is not mapped using the automated classification method. The automated classification technique classifies each individual pixel, mapping unit occurrences at the meter scale based solely on the color of each pixel in the scanned aerial photographs. Manual mapping identifies unit occurrences at a larger scale (1-2 orders of magnitude) but incorporates morphologic information

as well. In this way, manual classification is able to evaluate color pixels in the context of the flow field, whereas the automated classification evaluates pixels strictly on statistical parameters. The automated classification technique is used because it promotes mapping consistency and efficiency and will allow for mapping based on multispectral data in future studies. Minor changes in definition of the training areas change the classification and in turn affect units' proportions and mean slope values. However, repeated supervised classifications based on different training areas yield the same progression of mean slopes and do not significantly affect inferences made regarding flow field emplacement processes. Incorporation of thermal and radar data sets in future studies will provide a more comprehensive characterization of pahoehoe surfaces, as well as a means to include 'a'a textures in the classification methodology.

The ERMapper image processing software package offers several classification methods. A neighbor averaging method was initially used to reduce speckle in the data set. This approach was found to systematically eliminate small and narrow, elongate unit exposures, which caused units III and IV to be underrepresented in the classification. The maximum likelihood enhanced supervised classification technique was found to more accurately classify the units given the resolution of the data set and the scale of features identified. This classification method results in more speckle in the data set, although a significant amount of the noise is eliminated by masking out areas of the classification representing lobes of 'a'a, the pre-Mauna Ulu surface, and Chain of Craters Road. The remaining speckle observed within the flow field is consistent with field observations and the gradational nature of the units identified.

2.5.2. Unit Correlation to Topography

In general, the occurrence of the four pahoehoe surface units correlates with the pre-Mauna Ulu topography as expected. The sheet exposures of unit I have the lowest mean underlying slope presumably because coalescence and inflation, which produce the sheets of unit I, occur primarily on lower slopes [Hon et al., 1994; Cashman and Kauahikaua, 1997]. Primary sheets also tend to form on relatively horizontal surfaces because lateral and forward flow velocities become more equivalent as the underlying slope decreases [Hon et al., 1994]. Toe networks of unit II have a higher mean underlying slope because they occur in areas that were less subject to coalescence and inflation but were still flat enough to have low flow velocities. Toes form instead of sheets due to a decrease in supply and/or irregularities in the underlying surface. Field relationships indicate that viscous toe networks of unit III were emplaced primarily on other Mauna Ulu pahoehoe units and may therefore not be directly influenced by the pre-Mauna Ulu topography [Byrnes and Crown, 1999]. We speculate that the emplacement of unit III may be influenced by the pre-Mauna Ulu topography to the extent that the subsurface tube distributary network must locally experience sufficient pressure to force the higher-viscosity lava to breakout onto the surface. Unit IV exhibits ropy and platy channel surfaces that are commonly highly convoluted and sheared. This unit, with the highest mean underlying slope, results from high flow rates required to produce channels and their deformed surfaces. Unit abundance as a function of slope shows a strong dependence on the preexisting slopes present within the entire study area (Figure 2.4a). Normalizing each unit abundance curve to the whole area curve removes the bias due to the abundance of various slopes present within the study area, and shows that units I and II form preferentially on lower slopes, whereas unit IV dominates steeper areas (Figure 2.4b).

Although very low standard errors on the mean demonstrate a definite progression of mean slopes associated with the units, each of the four surface units is found on the full range of pre-Mauna Ulu slopes present in the study area (Table 2.1 and Figure 2.4). This is reflected in high standard deviations of the mean and can be attributed to three primary causes:

1. Flows are influenced by topographic features smaller than the minimum contour interval (~6 m), because advancing pahoehoe flows are typically <1 m thick.

2. Compound flows create their own small scale topography as they are emplaced, as witnessed in the active Pu'u 'O'o flow field. Small lobes of pahoehoe are commonly affected by, and even emplaced on, other active lobes. In addition, portions of the 1972-1974 Mauna Ulu flow field within the study area were emplaced on flows from the 1969-1971 eruptive sequence [Holcomb, 1976; Tilling et al., 1987].

3. Surface textures are also influenced by factors other than the underlying topography, such as supply rate and subsurface storage. Surface texture appears to be most directly related to flow rate during formation of the surface crust, which depends on effusion rate (from the local source, such as a tube), underlying slope and substrate, and viscosity. The breakout lobes of unit III may not have any direct coupling to the underlying topography but instead are a function of pressure conditions within the flow field, as well as the topography created by earlier Mauna Ulu flow lobes.

A series of DEMs with increasingly coarser topographic resolution was also created for comparison with the ~6 m contour interval DEM to determine sensitivity of the methodology to resolution limitations. This was done to provide insight for future analyses of compound flows on other planetary surfaces for which high resolution topographic data are not generally

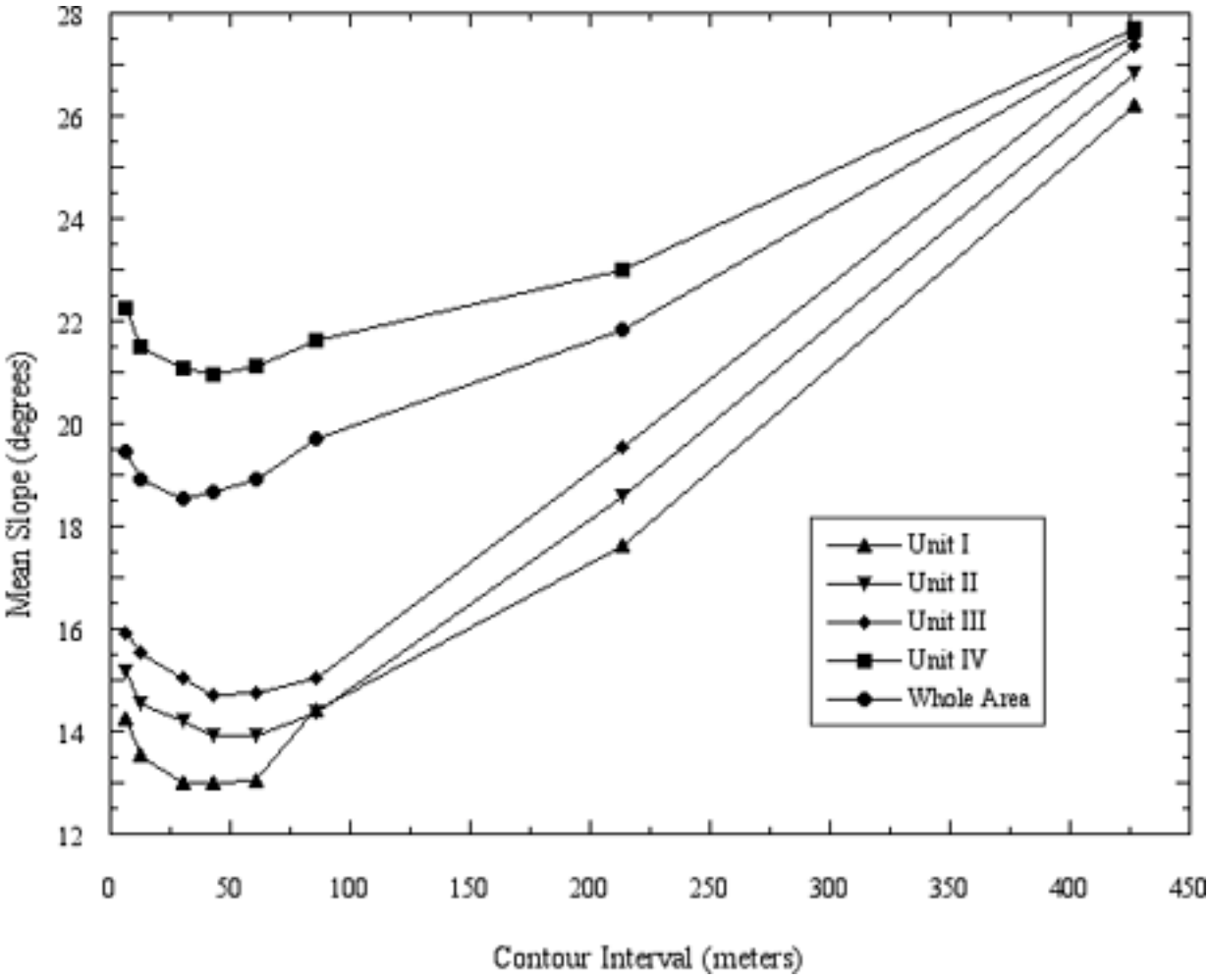

Figure 2.6. Effects of topographic resolution on unit mean slope discriminability. Note that the progression of mean slope values remains constant over contour intervals of ~6 to 430 m, whereas discriminability of means diminishes.

available. Contour intervals larger than 6 m yield the same progression of means up to an ~430 m (1400 foot) contour interval, although discriminability (separation of mean slope values) is reduced (Figure 2.6).

2.5.3. Lack of Unit Correlation to Lava Tubes

The distribution of pahoehoe units and the positions of major lava tube segments do not exhibit a strong spatial correlation. Because Swanson [1973] and Holcomb [1976] identified the pahoehoe within the study area as tube-fed and because blockages of lava tubes were observed to cause overflows and breakouts at Mauna Ulu [Tilling et al., 1987] and elsewhere [Kauahikaua et al., 1998], this relationship was unexpected.

The lack of correlation between pahoehoe surface units and proximity to lava tubes suggests two possible conclusions: (1) the major lava tubes do not significantly affect surface unit emplacement within the study area and/or (2) these lava tubes do not preferentially emplace any of the four units. Field observations support the first case in that the tubes do not display any surface expression over most of their extents. The second case is supported by observations made of the aerial photographs and in the field. In a few cases, units III and IV appear to be direct breakouts from the major tube system, based on the radial flow lobe morphology emanating from a localized source along a tube segment mapped by Holcomb [1976]. Field observations also show that primary sheets have been emplaced directly from the main tube system as overflows from skylights. If the first case is true, then surface units are probably primarily related to a smaller scale of lava tubes, as only the large tube segments are indicated on

the map of Holcomb [1976]. If the second case is correct, then the distribution of surface units cannot be used to make inferences about the lava tube distributary network.

Although there is no significant trend in unit distribution with distance from the major lava tubes, there are variations in the unit distribution. These variations suggest that other factors may influence unit emplacement relative to the location of lava tubes. For example, portions of the flow field that maintain a liquid core are more likely to form a lava tube and are also more likely to be subject to inflation which can produce unit I surfaces. The relationship between surface units and lava tubes is further complicated by the fact that different tube segments were active at different times during development of the flow field, and each segment undoubtedly experienced differences in supply and tube blockage. Further insight to the relationship between lava tubes and unit emplacement may be derived from extending the current analysis over the entire Mauna Ulu flow field, including documentation of breakouts and overflows from specific tubes. Additional detailed study of lava tubes in active flow fields is required to analyze the influence of various scales of tubes on surface unit emplacement over the course of flow field formation.

2.6. Conclusions

The development of a compound flow field is controlled by factors that characterize a given eruptive event (such as eruption temperature, lava composition, and the rate, history, and duration of supply) as well as factors that affect emplacement locally (such as topography and substrate, and the cooling, vesiculation, degassing, and crystallization history of the lava). For a typical pahoehoe flow, lava is transported through a subsurface distributary network from which

lobes are emplaced. Emplacement of pahoehoe units is affected by local conditions and the state of the lava, potentially producing a diversity of surface morphologies and textures in features at different scales. The emplacement of pahoehoe is therefore characteristically different than the emplacement of 'a'a, which is typically emplaced in individual lobes or a few main lobes having a continuous molten core.

Pahoehoe surface units are indicative of, and may be used to interpret, the complex emplacement histories associated with compound flow fields. This study defines pahoehoe surface units at Mauna Ulu and analyzes their distribution to understand the degree to which they are coupled to preflow topography and to the major tube segments. Mauna Ulu pahoehoe within the study area can be divided into four units based on color, surface texture (roughness and presence or lack of glassy crust), and morphology, which characterize their style of emplacement. Within the study area, these units can be identified and mapped in the field as well as in high-resolution color aerial photographs.

The distribution of pahoehoe units reflects differences in flow emplacement processes within the compound flow field, demonstrating that emplacement of flow field margins is not representative of emplacement of the entire flow field. This is expressed at Mauna Ulu by the contrast in complexity between flow field margins and interiors. Compound lobe margins are dominated by lobate sheets (unit I) and toe networks (unit II). These margins lack unit IV disrupted surfaces because concentration of flow is insufficient to form channels. Some unit I and II exposures defining compound lobe margins are supplied by channels either as downflow extensions or lateral overflows and breaches that widen the flow field. Flow field interiors show the full range of unit morphologies and textures identified because sheet and toe flow regimes

occur (producing units I and II), flow may be concentrated enough to form channels (unit IV), and these regions may serve as storage areas for later breakouts (unit III).

The units identified in the study area show a limited correlation to pre-Mauna Ulu topography based on the mean slopes calculated. In particular, in the Mauna Ulu study area, unit IV disrupted surfaces typically associated with channels occur on steeper preeruption slopes than the sheets and toe networks of units I and II. Factors other than topography also affect surface unit emplacement, however. For example, storage within the subsurface distributary network influences the distribution and nature of surface units, as toe networks of viscous lava are found superposed on other pahoehoe surfaces. Additional study is necessary to incorporate units characteristic of vent regions (such as those identified by Swanson [1973]) and those identified in other pahoehoe fields into assessments of the topographic influence on flow unit emplacement.

The overall distribution of surface units within the study area is not directly related to the largest scale of lava tubes. This result, coupled with field and remote sensing observations, suggests either that the surface unit distribution is primarily related to a smaller scale of distributary subsurface transport or that these main tube segments do not preferentially emplace any of the four surface units identified in this study. Additional investigation is required to determine the contribution of lava from different scales of lava tubes to the final flow surface over the formation of the flow field.

With an understanding of the morphologic variability of a flow field surface and documentation of relationships between surface morphology and emplacement processes, the ability to map surface units over a flow field with remote sensing data allows detailed analyses of the development and evolution of lava flow fields to be undertaken. Recent studies have

provided detailed characterizations of lava flow margins [Bruno et al., 1992, 1994], morphometric documentation of pahoehoe toe networks [Crown and Baloga, 1999], and assessments of scale-dependent tendencies within pahoehoe flows [Crown et al., 1998, 1999], from which a stochastic approach to modeling the emplacement of pahoehoe toe networks has been developed [Baloga and Crown, 1995; Baloga and Glaze, 2000]. The current study considers four types of pahoehoe surface units whose emplacement processes are reflected in particular dominant morphologic features (i.e., pahoehoe toe networks, sheets, or channels). Variations in the proportion of the various pahoehoe features and their relative importance in controlling flow field growth exist in different regions of a single flow field and between different flow fields. Studies such as the current investigation of the Mauna Ulu flow field can provide specific estimates of the areal extents and distribution of types of surface units within a flow field, which are essential for proper model applications.

Future work will also include use of thermal and radar remote sensing data sets coupled with visible-wavelength images and digital topography to provide more thorough characterizations of pahoehoe surface units. This will allow extension of the current study for analysis of the development of flow fields associated with other volcanic centers on Earth, as well as those on other planetary surfaces using newly acquired and future data sets.

Chapter 3

Emplacement of the Mauna Ulu flow field: New insights from integrated field and remote sensing analyses

3.1. Introduction

Knowledge of lava flow emplacement processes is fundamental to characterizing volcano growth and to understanding the development of lava flow fields for the purposes of hazard assessment and mitigation, as well as for comparison to volcanism in other planetary environments. The objectives of this research are to quantitatively characterize surfaces within the Mauna Ulu lava flow field (Kilauea Volcano, Hawai'i), to document relationships between surface units and remote sensing signatures, and to use the distribution of surface units to examine flow field development using remote sensing analyses. Field observations were made to determine surface characteristics associated with different types of lava flow units, to identify which characteristics related to flow emplacement can be identified remotely, and to provide a ground-based comparison to the remote sensing data. Remote sensing analyses utilized recently acquired ASTER (Advanced Spaceborne Thermal Emission and Reflection Radiometer) and MASTER (MODIS/ASTER airborne simulator) datasets [Yamaguchi et al., 1998; Hook et al., 2001]. These datasets provide a means to extend the spatial and spectral coverage from an initial study site (~6 km^2) within the Mauna Ulu flow field, which was investigated to determine relationships between pahoehoe surface units, topography, and lava tubes [Byrnes and Crown, 2001]. The current study also further develops a field and remote sensing approach to mapping and interpreting the emplacement of complex volcanic surfaces.

3.2. Background

Compound basaltic flow fields are emplaced in a complicated sequence of interfingering and overlapping lava flows, resulting in complex surfaces composed of numerous flow units emplaced in different styles and at different times during flow field evolution. The texture and morphology present at the flow surface are indicative of local emplacement conditions and provide important constraints for understanding flow field development. For example, surface characteristics have been related to effusion rate [Walker, 1972; Pinkerton and Sparks, 1976; Rowland and Walker, 1990], style of eruption and lava transport [Swanson, 1973], flow rheology [Peterson and Tilling, 1980; Rowland and Walker, 1987], flow inflation [Walker, 1991; Hon et al., 1994], thermal conditions [Keszthelyi and Denlinger, 1996], local topography and lava storage [Crown and Baloga, 1999; Byrnes and Crown, 2001], and scale-dependencies of lava distributary networks [Crown et al., 2002a; see also Crown et al., 1998, 1999, 2001].

Swanson [1973] described three intergradational pahoehoe types within the Mauna Ulu flow field that reflect differences in eruption style and transport. Near-vent surface-fed flows formed smooth-surfaced, dense pahoehoe or formed shelly pahoehoe, depending on whether the lava was emplaced from high lava fountains or overflows of the vent, respectively. Dense, hummocky pahoehoe in the medial and distal portions of the flow field was fed from lava tubes. Differences in eruption and transport of these three pahoehoe varieties produced differences in degassing, which affected emplacement and is reflected in the final morphology and surface texture of flow units. Dense near-vent pahoehoe was fountain-fed, which allowed degassing and produced relatively vesicle free lava in thin flow units. These flows commonly formed broad, leveed channels with associated overflows that are grossly similar to hummocky tube-fed pahoehoe, except that they lack tumuli. Surface units fed from vent overflows were gas-rich and

produced shelly pahoehoe, which contains cavities formed due to volatile exsolution and/or draining of the flow interior. These flows were emplaced as toes and sheets with crusts that may display fractures, buckles, and festoons. The hummocky, tube-fed pahoehoe has an intermediate vesicularity indicative of limited degassing during transport through the lava tube system. These flows have glassy crusts, commonly form lobes of pahoehoe toes, and display tumuli. Both fountain-fed surface flows and tube-fed flows transition to 'a'a in various places within the Mauna Ulu flow field [Swanson, 1973].

In addition to a range of meter-scale surface morphologies, differences in small-scale texture have been described. Wilmoth and Walker [1993] characterized differences in vesicles for tube-fed flows in the Mauna Ulu and Kupaianaha flow fields. S-type (spongy) pahoehoe displays selvages (outer ~6 cm) containing abundant (>40 vol. %), small (<4 mm), approximately spherical vesicles. P-type (pipe-vesicle bearing) pahoehoe is less common and displays lower vesicularity, lower porosity, and larger vesicles (including pipe vesicles near the base of each flow unit) relative to S-type pahoehoe. S-type pahoehoe may commonly spall flakes of the surface skin during and immediately following emplacement, whereas spallation is negligible for P-type pahoehoe. In addition to the difference in spallation, P-type pahoehoe may be distinguished based upon its distinct bluish surface coloration. Wilmoth and Walker [1993] suggest that crust spallation serves as a release for contractional stresses that are created as lava cools.

Vesicles are significant for several reasons in addition to their effect of increasing flow viscosity [e.g. Polacci et al., 1999]. The distribution of vesicles is indicative of pahoehoe eruption and transport styles, as described above for fountain- vs. vent overflow-fed and surface- vs. tube-fed pahoehoe flows [Swanson, 1973]. Vesicles also affect flow cooling, as increased

surface vesicle abundance promotes cooling of flow lobes [Keszthelyi and Denlinger, 1996]. Furthermore, vesicle distributions are correlated with flow ponding, coalescence, and inflation, reflecting the local pressure and cooling conditions at the interface of a flow's surface crust and molten interior [Hon, 1994; Cashman and Kauahikaua, 1997].

3.3. The Mauna Ulu flow field

The Mauna Ulu satellitic shield is located on the upper east rift zone of Kilauea Volcano. An approximately 61 km^2 flow field was emplaced from Mauna Ulu and local vents in two main episodes. The long-lived eruption (May 1969 to July 1974) displayed a wide variety of activity, including fire-fountains (the highest of which was >500 m), "gas-piston" cycles of rise and fall of the lava column that fed vent-overflow shelly pahoehoe units and built the 120 m-high Mauna Ulu shield, and the development of an extensive lava tube system that fed flows over 12 km from the vent region to the Pacific Ocean [Swanson, 1973; Swanson et al., 1979; Tilling et al., 1987].

Holcomb [1976] illustrates the distribution of 'a'a as well as surface-fed and tube-fed pahoehoe within the Mauna Ulu flow field. He indicates that tube-fed pahoehoe flows emanated from "master lava tube systems" that are marked by low, broad ridges. Swanson [1973] suggests that most of the Mauna Ulu tube-fed pahoehoe was probably emplaced from small, distributary tubes that branched from the master tubes.

3.4. Field characterization of the Mauna Ulu flow field

3.4.1. Initial Mauna Ulu site study

An initial site within the Mauna Ulu flow field [Byrnes and Crown, 2001] was selected to examine the diversity of pahoehoe surface units within flows that were mapped by Holcomb [1976] as tube-fed flows and classified as dense, hummocky pahoehoe by Swanson [1973]. The Mauna Ulu flow field was chosen because the flows are well exposed and relatively pristine, and because the eruption was long-lived and well documented [e.g. Moore et al., 1973; Swanson, 1973; Holcomb, 1976, 1987; Swanson et al., 1979; Tilling et al., 1987]. The site is located on and below Holei Pali 7 to 9 km from the Mauna Ulu vent, covers ~6.2 km^2 (~10% of the flow field), and was selected because it displays a significant local diversity of surface units.

Four varieties of pahoehoe lava flow surface units were defined and mapped within the initial study area using high-resolution color aerial photographs [Byrnes and Crown, 2001]. Field observations combined with Geographical Information Systems (GIS) analyses indicated that the visible-wavelength signatures represented in the photographs are controlled by the characteristic colors, surface textures (roughness and presence or lack of glassy crust), and morphologies (sheets, toes, or channels) of these units.

The four pahoehoe units distinguished display primary morphologies related to the local lava flow regime during emplacement. These morphologies range from sheets (broad, flat units occurring where emplacement is unconfined, or resulting from the coalescence and inflation of toes and/or small sheets and channels) to toes (small units, interconnected networks of which form small to intermediate lobes) to channels (centralized area of flow concentration, occurring where local flow rates are sufficiently high) [Byrnes and Crown, 2001]. Flow-unit textures include glassy, ropy, and slabby surfaces, gradational to a clinkery 'a'a texture. Unit I is

characterized by glassy-surfaced sheets, large occurrences of which display composite surfaces containing coalesced small sheets and/or toes. Unit II is composed of pahoehoe toes that display a similar glassy crust and is gradational to unit I with increased flow coalescence and inflation. Unit III has darker toes that lack a smooth surface crust, appears to have had a higher flow viscosity during emplacement (based on relatively equant toes and vesicles preserved on exposure surfaces), and represents locally late-stage emplacement (based upon stratigraphic position, and consistent with inferred viscosity). Unit IV typically exhibits a leveed channel morphology with a disrupted, slabby surface that displays primary unit I, II, and III surfaces and is gradational to 'a'a. Byrnes and Crown [2001] provide detailed descriptions and field photographs of these units.

These surface units represent the emplacement of lava under a variety of flow regimes (sheets, toes, and channels) and emplacement histories (primary morphologies, late-stage breakouts, and secondary disruption) within the flow field. The distribution of units was successfully mapped using an automated classification technique with high-resolution color aerial photographs. Proportions of the four units vary by an average of ~10% between the automated classification and manual mapping for a subscene of the study area [Byrnes and Crown, 2001]. Within the initial study area, the flow field margins are dominated by lobate sheets and toe networks (units I-II), whereas the flow field interior typically displays the full range of surface units. Additionally, the unit distribution is correlated with the pre-eruption topography, primarily displaying unit I sheets and unit II toes over relatively horizontal topography (mean slopes of 14.2° and 15.2°, respectively) and disrupted unit IV channels over steeper topography (22.2°). No correlation was found between the unit distribution and the location of the lava tubes previously mapped by Holcomb [1976], consistent with the assessment

of Swanson [1973] that lava was emplaced primarily from distributary tubes rather than the master tubes, as well as with recent field mapping of Mauna Ulu tube and channel systems [Crown et al., 2002a; see also Crown et al., 2001].

Surface textures were found not to be directly coupled to unit morphology, and field analyses indicate that the semi-quantitative classification of visible-wavelength images does not reflect transitional forms observed between the four tube-fed pahoehoe units defined in the initial study [Byrnes and Crown, 2001]. Determination of the relationships between small-scale surface textures and flow morphologies as well as further discrimination of surface units necessitates detailed field analyses of pahoehoe surface crusts. Furthermore, such analyses would allow incorporation of thermal infrared (TIR) remote sensing analyses to complement visible-wavelength analyses, because TIR data is influenced by textural and compositional variations. Additionally, extending the spatial coverage from the initial study area is required to incorporate additional types of surface units into analyses of the development of a complete flow field.

3.4.2. Methodology

In the current study, field observations were made to describe the variety of surface units within the Mauna Ulu flow field, document surface parameters related to flow emplacement, and identify which parameters may produce identifiable visible- and thermal-wavelength spectral signatures. These observations took place over a large portion of the flow field. Specific sites were selected that represent typical unit exposures as well as the range of morphologies and surface textures observed, including transitions between units. The selected study sites range in size from ~7 to 3000 m^2 and include 15 exposures of unit I, 9 exposures of unit II, and 7 exposures of unit III (Table 3.1), which were geolocated using a high-resolution (~10 cm

horizontal accuracy) differential Global Positioning System (dGPS; see Figure 3 and Appendix A). Descriptions of each site were compiled, noting unit morphology and color, context within the flow field and local stratigraphic relationships, topographic characteristics, and small-scale characteristics, including vesicularity, phenocryst abundance, and microtopography. For exposures of units I-III, estimates were made of the degree of spallation for flow unit surfaces (expressed as the areal percentage of spalled vs. intact crust), the areal abundance and size of vesicles and phenocrysts on surface crusts and spallation surfaces. Values for unit IV and 'a'a surfaces were not obtained. Unit IV surfaces are highly variable, containing slabs that are interpreted to have formed initially as units I-III and subsequently to have been disrupted, representing a transitional phase to the development of 'a'a clinkers. 'A'a surfaces do not typically preserve any quenched, glassy crust, and vesicularity estimates are not possible on these surfaces. The degree of spallation for units I-III was estimated over the entire unit exposure at a given site. Estimates of vesicularity and phenocryst abundance and size were made by selecting and describing representative areas (typically 5-10% of the unit exposure) of the surface crust and spallation surfaces. These estimates were made in order to characterize the range of surfaces observed and understand transitions between the units. Qualitative comparisons were then made to near-vent (fountain-fed and shelly), P-type, and unit IV pahoehoe varieties, as well as 'a'a.

Table 3.1. Field estimates of small-scale surface characteristics

site	crust spalled (%)	vesicles				phenocrysts			
		surface crust		spallation surface		surface crust		spallation surface	
		abundance (%)	size (mm)	abundance (%)	size (mm)	abundance (%)	size (mm)	abundance (%)	size (mm)
Unit I									
3.1.d	10	0	—	20	<0.5 - 3	0	—	<5	≤4
3.2.a	5	0	—	25	<0.5 - 3	0	—	<1	≤3
3.2.b[†]	90	0	—	30	1 - 3	0	—	15 - 20	1
3.3.a	5	0	—	10	1	0	—	<5	2
4.1.c	5	0	—	10	<0.5 - 3	0	—	0	—
4.3.b	40	<5	2	60	<0.5 - 33	0	—	10	1 - 2.5
6.1.a	60	0	—	40	0.5 - 2	0	—	0	—
6.3.a	20	0	—	<5	<1 - 2	0	—	0	—
6.4.a	70	0	—	40	0.5 - 2	0	—	0	—
6.5.a	80	10	1 - 2	40	0.5 - 2	0	—	<5	1
7.1.aA	<5	0	—	—	—	0	—	—	—
7.2.a	10	0	—	20	1 - 3	0	—	0	—
7.3.a	10	0	—	30	1 - 2	0	—	0	—
7.4.a	10	0	—	20	1 - 2	0	—	<1	2
7.6.a	20	0	—	10	0.5 - 2	0	—	0	—
mean	29 ± 18	1 ± 1	—	26 ± 12	—	0	—	3 ± 3	—
range	<5-90	0 - 10	1 - 2	<5-60	<0.5 - 33	0	—	<1 - 20	1 - 4

[†]unit I exposure at site 3.2.b displays a ropy, channelized sheet surface (rather than the more typical flat sheet surface)

Table 3.1. (continued)

site	crust spalled (%)	vesicles				phenocrysts			
		surface crust		spallation surface		surface crust		spallation surface	
		abundance (%)	size (mm)	abundance (%)	size (mm)	abundance (%)	size (mm)	abundance (%)	size (mm)
Unit II									
3.1.a	20	0	—	55	0.5 - 5	0	—	5	<1 - 5
4.1.b	50	0	—	20	1	0	—	10	≤3
5.1.a	20	0	—	50	0.5 - 1	0	—	0	—
6.1.a1	50	<5	1 - 2	30	1 - 2	0	—	0	—
7.1.aC	20	0	—	20	1	0	—	0	—
7.2.a1	70	0	—	40	0.5 - 3	0	—	0	—
7.4.a1	50	5	1 - 2	40	1 - 4	0	—	20	1 - 3
7.6.a1	10	0	—	20	0.5 - 3	0	—	0	—
7.7.a	10	0	—	20	0.5 - 4	0	—	0	—
mean	33 ± 19	1 ± 1	—	33 ± 9	—	0	—	4 ± 5	—
range	10 - 70	0 - 5	1 - 2	20 - 55	0.5 - 5	0	—	0 - 20	<1 - 5
Unit III									
3.1.b	90	40	1 - 2	60	<1 - 5	<5	≤3	10	≤2
4.1.a[#]	80	<5	<5 - 30	40	1 - 40	0	—	10	≤5
4.2.a	80	<5	2	40	0.5 - 2.5	0	—	20	1 - 4
4.2.b	90	10	1 - 2	30	2	0	—	<5	<1
5.1.b[‡]	70	20	1 - 13	30	1 - 3	0	—	20	2 - 4
7.1.aB	40	70	1 - 10	50	1 - 2	0	—	<5	≤4
7.3.a1	—	20	1 - 2.5	40	1 - 4	0	—	20	3 - 10
mean	75 ± 13	24 ± 18	—	41 ± 8	—	0 ± 1	—	12 ± 7	—
range	40 - 90	<5 - 70	1 – 30	30 - 60	0.5 - 40	0 - <5	≤3	<5 - 20	<1 - 10

[#]two populations of vesicles are present on site 4.1.a spallation surface, one consists of small (~1 mm) undeformed vesicles and the other displays highly deformed vesicles up to 5 mm wide by 40 mm long

[‡]a breakout of higher viscosity lava at site 5.1.b displays spallation surfaces with 20% vesicles (2-3 mm) and 30% phenocrysts (3-7 mm)

Figure 3.1. ASTER image of the Mauna Ulu flow field. Image displays ASTER band 3 (0.81 μm) as red, band 2 (0.66 μm) as green, and band 1 (0.56 μm) as blue. Vegetation on the pre-Mauna Ulu surface of Kilauea Volcano appears red in the composite image. Locations of study sites are indicated in yellow (see also Appendix A). Inset image shows location of pixels from which point spectra were obtained. Clouds appear white to cyan and are visible in the northeast portion of the image, obscuring part of the near-vent region.

3.4.3. Results

Unit I exposures typically have morphologies at the dm- to m-scale that are flat or display ropy, channelized zones, and range from individual sheets to composite surfaces composed of coalesced toes and sheets. The unit generally exhibits relatively low degrees of crust spallation. Surface crusts display limited (<5%), small (1-2 mm) vesicles and no phenocrysts, tend to be bronzy and glassy, and may be smooth or display mm-size ridges or dark, glassy knobs. Unit I spallation surfaces display more and larger vesicles, some small phenocrysts, and are concentrated in areas that have undergone deformation due to folding or inflation. Two types of surface coatings or alteration have been observed at some locales: a white variety, which is spatially associated with small cracks, and a splotchy, yellow to orange variety that appears to be preferentially associated with pahoehoe ropes, but is also found in flat portions of exposures.

Unit II morphologies consist of lobes of toe networks displaying low degrees of spallation, and exhibit both smooth surfaces and small ropy, channelized zones. Similar to unit I, unit II surface crusts display limited (<5%), small (1-2 mm) vesicles and no phenocrysts, tend to be bronzy and glassy, and may be smooth or display mm-scale ridges and/or dark, glassy knobs. Spallation surfaces are more vesicular and exhibit phenocrysts, and are also associated with disrupted areas. Both the white and splotchy surface coatings/alteration have been observed on unit II surfaces.

Unit III exposures consist of lobes of toe networks that may be smooth (at the dm-scale), ropy, or platy. Toes tend to be more equant, lobes are thicker, and crust spallation is more prevalent relative to toes of unit II. Unit III exposures are generally the last unit emplaced locally, based on flow stratigraphy, and are fed as breakouts from other surface units. Unit III surface crusts have relatively high vesicularities, may display phenocrysts, and typically are dark

and rough (mm- to cm-scale) due to the presence of glassy knobs and/or ridges. Some unit III exposures feed breakouts of darker, more viscous lava that typically displays more abundant and larger vesicles and phenocrysts. In limited areas, the unit III surface crust displays rare bronzy glass filaments similar to those which are a common part of unit I and II surface crusts. Spallation surfaces display more and larger vesicles and phenocrysts. The splotchy variety of surficial coating/alteration tends to be orange and is commonly found on pahoehoe ropes.

Unit IV exposures are typically large and commonly bounded by levees. They display highly disrupted surfaces composed of jumbled plates and slabs exhibiting textures associated with units I/II and III that are intermixed with 'a'a clinkers. 'A'a surfaces typically lack glass, may be dark gray to red, and are rough at the mm- to dm-scale.

Other varieties of pahoehoe were also observed, including surface-fed and transitional units. Both dense, fountain-fed pahoehoe and shelly pahoehoe typically display a bronzy, glassy surface crust similar to units I and II (Figure 3.2). The fountain-fed pahoehoe units are generally large and display a relatively smooth, bronzy, glassy surface crust and a range of morphologies consistent with emplacement as sheets, channels, and large (m-scale), elongate toes. Shelly pahoehoe displays a similar bronzy appearance, although it is not typically as smooth and glassy. Shelly pahoehoe may be emplaced as sheets or toes and is typically hollow beneath the upper few centimeters, and is transitional to a disrupted (unit IV-type) surface with collapse of the crust. Intermediate units that display transitions to both surface-fed varieties were also observed, indicated by Swanson [1973] to have formed from low (<100 m) lava fountains. The surface-fed flows observed in the proximal region have undergone significant post-emplacement alteration

a

Figure 3.2. Surface-fed pahoehoe in the Mauna Ulu proximal region. (a) Overview, showing folded and buckled shelly pahoehoe in the foreground (on which B. Banks is standing), fountain-fed pahoehoe in mid-ground, and Mauna Ulu vent in background. (b) Detail of shelly pahoehoe surface, displaying the altered glassy crust and small portions of the spallation surface (*sp*).

b

Figure 3.2. (continued)

of their surfaces relative to flows in the medial and distal regions, presumably due to the greater rainfall in the proximal region. Those units closest to the vent have additionally been subjected to post-emplacement chemical alteration due to degassing that continues at Mauna Ulu.

Field estimates of spallation, vesicle abundance, and phenocryst abundance are shown in Table 3.1. Each of the units displays a wide range in the proportion of surface crust that has been spalled and the abundance of vesicles and phenocrysts. Mean values of spalled crust are similar for units I (29%) and II (33%) and significantly higher for unit III (75%). Spallation appears to occur at different scales, from flaking of the outermost mm-scale skin to fracturing and removal of cm-scale crust, which exposes darker, progressively higher-vesicularity portions of the flow-unit interior. It appears that most of the vesicles that had formed on the surfaces of units I and II were stretched and flattened due to plastic deformation of the crust during emplacement. Unit III tends to preserve the surface expression of vesicles, although vesicles may be deformed. Although vesicularity estimates were not made for 'a'a surfaces, they were consistently found to have greater mm- to cm-scale roughness than the pahoehoe units. Olivine is the only mineral identified as phenocrysts. Phenocryst abundance is higher within unit III exposures (12% on the spallation surface) than for units I (3%) and II (4%).

Transitions between the four tube-fed pahoehoe units are common. Unit I sheets transition to unit II toes at their margins (presumably due to decreased flow rate), and unit II toey lobes transition to unit I sheets (through coalescence and inflation of the flow unit) [Byrnes and Crown, 2001]. A transitional unit that is intermediate to units I and III is present in the medial region above Holei Pali. It displays a unit I sheet morphology and a surface texture similar to unit III, attributed to high supply rates (relative to typical unit III exposures) and a degree of

apparent pre-emplacement cooling intermediate to the typical unit I and III end members. Units I, II, and III may all transition to unit IV with disruption of the flow surface, commonly associated with inflation and generally manifested as breaking of the unit into slabs. Additionally, units III and IV are transitional to an 'a'a texture with increased disruption of the flow surface.

Vesicle distributions within the units indicate that S-type pahoehoe is much more abundant than P-type, consistent with Wilmoth and Walker [1993]. We observed one exposure of P-type pahoehoe (below Holei Pali) displaying a glassy blue crust that lacks vesicles and phenocrysts and exhibits mm-scale knobs and minimal crust spallation. The spallation surface contains <1% vesicles (0.5-1 mm). Void spaces observed in the unit interior were few in number, but were large (dm-scale) and occupied a significant proportion of the volume of small lobes. The splotchy surface coating/alteration was observed to be extensive on the exposure, and the white "crack-filling" variety was also observed.

3.4.4. Significance

Detailed characterization of pahoehoe surface crusts yields a wide range of estimated values of surface spall, vesicle abundance, and phenocryst abundance, indicating that each of the units may be produced under a variety of conditions, consistent with the observed unit transitions. The characterization also indicates, however, that the unit I/II and III surface crusts represent two dominant primary surface textures that presumably reflect dominant conditions for Mauna Ulu pahoehoe emplacement.

Because spallation is related to stresses that develop in the lava crust, the greater amount of spallation on unit III surfaces suggests cooling sufficient to accommodate significant brittle

deformation before the cessation of movement. This indicates it had a different thermal history than units I and II, which are interpreted to predominantly have had crusts that were hot enough to plastically deform throughout most of flow advance. The high degree of unit III spallation and abundance of vesicles are also consistent with previous field observations that suggested unit III was relatively viscous during emplacement [Crown and Baloga, 1999; Byrnes and Crown, 2001]. These conclusions are also consistent with the interpretation that the bronzy, stretched glass filaments on unit I sheets and unit II toes formed as vesicles were stretched and lost concavity, whereas unit III tends to preserve the definition of vesicles at the flow surface.

Phenocrysts are indicative of cooling history and may indicate prolonged storage within the subsurface lava tube distributary network or may be transported from the vent. The high phenocryst abundance within unit III (relative to units I and II) should contribute to the higher apparent flow viscosity. Furthermore, the abundance of phenocrysts, coupled with the observation that unit III tends to locally be the last emplaced, supports the hypothesis that the lava has experienced storage in the subsurface distributary network [Crown and Baloga, 1999; Byrnes and Crown, 2001], which would allow crystal formation and/or settling to occur.

Unit IV and 'a'a textures indicate that the flow surface experienced significant disruption. In this respect, they represent secondary morphologies, although unit IV may preserve primary surface crusts on slabs and plates. The similarities between surface-fed pahoehoe and tube-fed units I and II indicate that similar sheet and toe flow regimes occurred throughout the flow field, although several important differences are important for understanding flow field development. The larger areal size of the surface-fed units suggests that the volumetric supply rate was greater for these units than locally from lava tubes, consistent with observations made of the emplacement of these units [Swanson, 1973]. Furthermore, surface-fed flows do not generally

appear to have undergone flow inflation, and the significant differences in vesicle content (which affects flow rheology) suggest that the actual flow of lava may have been more varied than is indicated by the resulting morphologies.

It is clear from these analyses that the various morphologies and textures may form under a range of conditions. For example, toes indicate low local flow rates during emplacement, whereas sheets and channels reflect successively higher flow rates (for similar topography and flow substrate). A smooth, glassy crust indicates that a flow unit was relatively hot and fluid during emplacement, whereas a vesicular surface indicates that a flow had experienced a greater degree of cooling prior to emplacement. Combining morphologic and textural information provides greater constraints on the state of the lava during emplacement than either provides by itself. Although the wide range of small-scale characteristics and the transitions between units indicate that the surface units are emplaced under a wide variety of conditions, the type examples present suggest that, within the Mauna Ulu flow field, a limited set of emplacement conditions (pertaining to supply rate, flow viscosity, cooling history, etc.) were dominant during the development of the flow field.

3.5. Spectral characterization of the Mauna Ulu flow field

3.5.1. Thermal infrared remote sensing of volcanic surfaces

Thermal-infrared (TIR) wavelength remote sensing datasets may be used to map variations in surface properties and/or thermal anomalies because thermal radiance is a function of a surface's emissivity (a material property) and temperature [e.g. Gillespie, et al., 1990; Hook et al., 1992; Kahle and Alley, 1992]. TIR data have been used to discriminate rocks of different

mineralogic content [e.g. Vincent and Thomson, 1972; Walter and Salisbury, 1989] and lithology [e.g. Vincent et al., 1972; Kruse and Kierein-Young, 1990]. Previous volcanologic investigations have used TIR data to map the distribution of basaltic units of similar composition and varying age [Kahle et al., 1988], silicic units of similar composition and varying vesicularity [Ondrusek et al., 1993; Ramsey and Fink, 1999], and thermal anomalies associated with active lava tubes [Realmuto et al., 1992].

Vesicularity variations among flow surfaces of consistent composition may be modeled by measuring the relative depths of spectral features [Ondrusek et al., 1993; Ramsey and Fink, 1997, 1999]. For example, a basaltic pahoehoe exposure may be modeled as a surface composed of smooth basaltic glass and vesicles (or similar small-scale roughness elements). Relative proportions of these two spectral end members may be calculated by measuring the depth of the glass absorption feature present at ~9.1 μm, because vesicles effectively contribute a reflectance component to the emissivity spectra that mutes the glass signature and may therefore be modeled as featureless blackbody radiators [Ramsey and Fink, 1999]. Because thermal emittance from multiple components mix linearly in proportion to their areal abundance, TIR spectra can be deconvolved to estimate proportions of end member surfaces within a pixel [Thomson and Salisbury, 1993; Ramsey and Christensen, 1998]. Ramsey and Fink [1999] applied this method to successfully calculate vesicularity of silicic lava flow surfaces (mean RMS error of 0.51% emissivity) in order to map the distribution of textural units at Medicine Lake Volcano (California, USA). The application of this methodology has been further extended to active silicic domes [Ramsey and Dehn, 2002].

3.5.2. The ASTER and MASTER datasets

Due to the importance of vesicularity on lava flow emplacement, datasets were used in this study that included TIR emittance in addition to visible and near infrared (VNIR) reflectance. Such data were acquired for the Mauna Ulu flow field by ASTER on May 4, 2000 and by MASTER on October 14, 2000 during the PacRim II mission (Figure 3.3). The ASTER instrument is described in detail by Yamaguchi et al. [1998] and its application to volcanic processes is further explained by Ramsey and Flynn [2002] and Pieri [2002]. The ASTER data used herein were processed to Level 1B (radiometric and geometric corrections). ASTER data are 15 m/pixel resolution in the VNIR, 30 m/pixel in the SWIR, and 90 m/pixel in the TIR. The airborne MASTER instrument was developed to simulate and validate ASTER and MODIS (Moderate Resolution Imaging Spectroradiometer) data [Hook et al., 2001]. The MASTER instrument has an instantaneous field of view of 2.5 mrad for all bands, yielding data that are ~13.6 m/pixel at nadir at sea level (given a flight altitude of 5458 m).

3.5.3. Methodology

Remote sensing analyses were performed in order to determine the spectral characteristics of Mauna Ulu surface units and to assess whether the surface units of interest could be discriminated. First, the ASTER and MASTER datasets were processed, and mean spectra were derived for identifiable, areally extensive exposures of surface units. These spectra are compared with examples of point spectra in section 3.6, and interpretations of the remote sensing images are discussed in section 3.7.

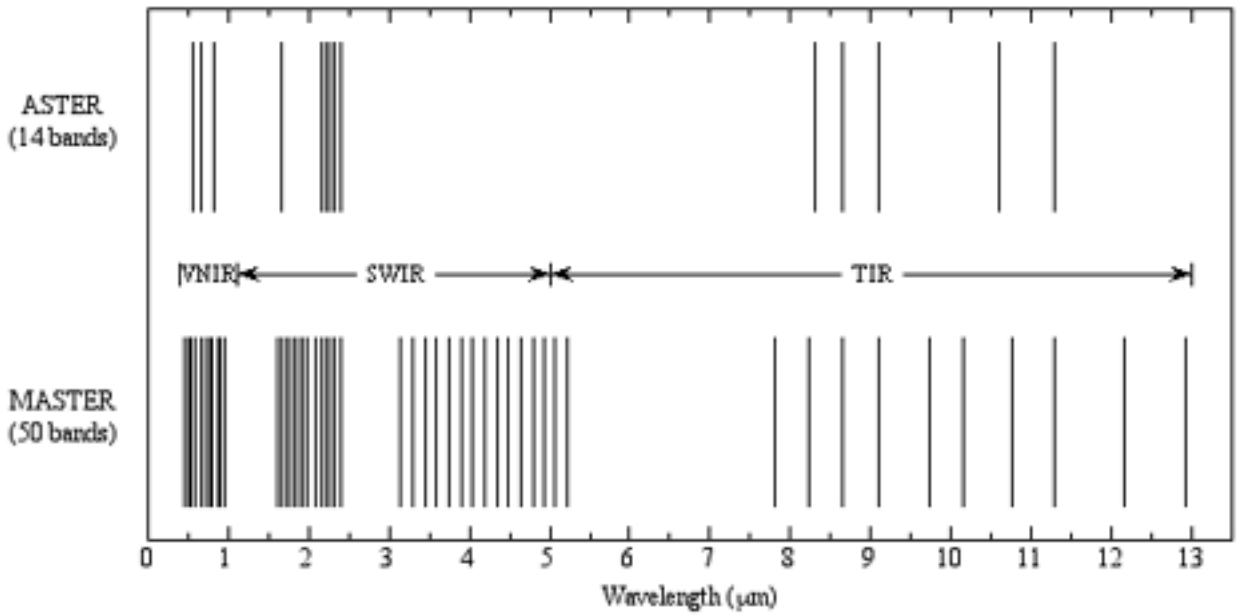

Figure 3.3. Band positions of the ASTER and MASTER remote sensing instruments. Wavelength regions are also indicated: VNIR = visible + near infrared, SWIR = short wavelength infrared, and TIR = thermal infrared.

ASTER VNIR DN values were converted to ground radiance using the scale factors provided in the dataset header information. A temperature-emissivity separation was performed on the ASTER TIR bands in order to remove the temperature component from the ground radiance to yield emissivity. The separation utilized an emissivity normalization technique [Realmuto, 1990] with an emissivity maximum value of 0.985. Moderate variations of the emissivity maximum value do not affect interpretations; Realmuto [1990] indicated that maximum values of 0.95-1.0 are reasonable for basalt, and Kahle and Alley [1992] have shown that small errors in the assumed emissivity value will not affect spectral differentiation. The TIR-derived emissivity values were subsequently normalized to a flat mean water spectrum based on 51,000 pixels (~11.5 km^2) representing the Pacific Ocean. This normalization was required to correct for systematic errors that were presumably related to the atmospheric correction. Geometric corrections were applied to the entire dataset in order to coregister the data with the high-resolution dGPS data that we collected at the selected field sites during November 1999 and July 2001.

The MASTER VNIR DN values were converted to radiance at sensor using the calibration slopes provided in the dataset header information. A standard atmospheric model (MODTRAN) was utilized to convert the radiance at sensor to ground radiance for elevations of 150, 450, and 750 m. The scenes were then cut (near the pali) and mosaiced in order to account for large-scale topographic changes (and hence changes in atmospheric thickness) along the flight line from south to north. Additionally, a dark object subtraction was performed on band 1 (0.46 μm) to correct for atmospheric radiance. The TIR MASTER ground radiance was converted to emissivity (as above) and normalized to a flat mean water spectrum based on 8220 pixels (~1.85 km^2) representing the Pacific Ocean. The 5- to 8-μm portion of the TIR data was

not used because these data are fairly noisy in this dataset, and the strongest reststrahlen bands (fundamental molecular vibrations of silicates) occur within the 8- to 13-μm region [e.g. Salisbury and D'Aria, 1992]. The data were corrected for panoramic distortion and coregistered with the dGPS and ASTER data.

Coregistration of the datasets was performed using nearest neighbor resampling in order to avoid pixel averaging, and all bands in both datasets were resampled to 15 m/pixel. For comparison, a mosaic of high-resolution color aerial photographs of the initial study site and a supervised classification derived from the mosaic [Byrnes and Crown, 2001] were also coregistered with the dGPS, ASTER, and MASTER data.

Average VNIR-derived reflectance and TIR-derived emissivity values were calculated to compare mean spectra of the four pahoehoe surface units of the initial site study [Byrnes and Crown, 2001]. The automated classification of Byrnes and Crown [2001] was used to create data masks for pahoehoe units I-IV. Mean spectra for those units were calculated using the masks, which represent the entire classification, with subsampled ASTER, MASTER, and derived datasets. Means represent averages of 1,342,821 pixels (~1.34 km^2) for unit I, 778,452 pixels (~0.78 km^2) for unit II, 358,367 pixels (~0.36 km^2) for unit III, and 304,726 pixels (~0.30 km^2) for unit IV in the subsampled data. Mean 'a'a spectra are based on the distal portion of a large 1969 'a'a lobe (Figure 3.1, see also Appendix A), using 1190 pixels (~0.27 km^2) for ASTER and 2465 pixels (~0.55 km^2) for MASTER. Mean spectra for surface-fed pahoehoe (fountain-fed and shelly) were derived from two areas totaling 1404 pixels (~0.32 km^2) for ASTER. Fountain-fed and shelly pahoehoe were not analyzed separately in the current study because discrete, extensive exposures of each unit have not been mapped in the available

datasets. Surface-fed pahoehoe was not analyzed for MASTER due to extensive cloud cover over the proximal region of the flow field during data acquisition.

Small-scale roughness was calculated for the ASTER and MASTER datasets through the use of a linear deconvolution model [Ramsey and Fink, 1999]. For this study, the model fit two end member emissivity spectra to each pixel within the datasets, that of an ideal blackbody and a Mauna Ulu basaltic glass sample (lab spectra obtained following Ruff et al. [1997]). The model then calculated the proportions of the two end members to produce a value for each pixel that represents the areal abundance of the blackbody.

3.5.4. Results

Reflectance spectra derived from the ASTER and MASTER VNIR data are shown for the Mauna Ulu surface units in Figure 3.4. Error bars representing standard error on the mean are smaller than the symbols used to plot the data, although standard deviations display overlap. The shape and magnitude of the reflectance spectra differs between the two datasets, which may be due, in part, to differences in viewing geometries. Despite these differences, the flow units display the same overall progression in surface reflectance. Surface-fed pahoehoe displays the greatest reflectance at all wavelengths in the ASTER VNIR, and both instruments indicate that reflectance decreases from pahoehoe unit I sheets to unit II toe lobes to unit III breakouts to disrupted unit IV surfaces and finally to 'a'a lobes. Mean ASTER and MASTER emissivity spectra for the four units are shown in Figure 3.5. These display differences in emissivity at ~9.1 μm, which are used with the linear deconvolution model [Ramsey and Fink, 1999] to derive small-scale surface roughness (Figure 3.6). Mean model small-scale roughness values indicate

a

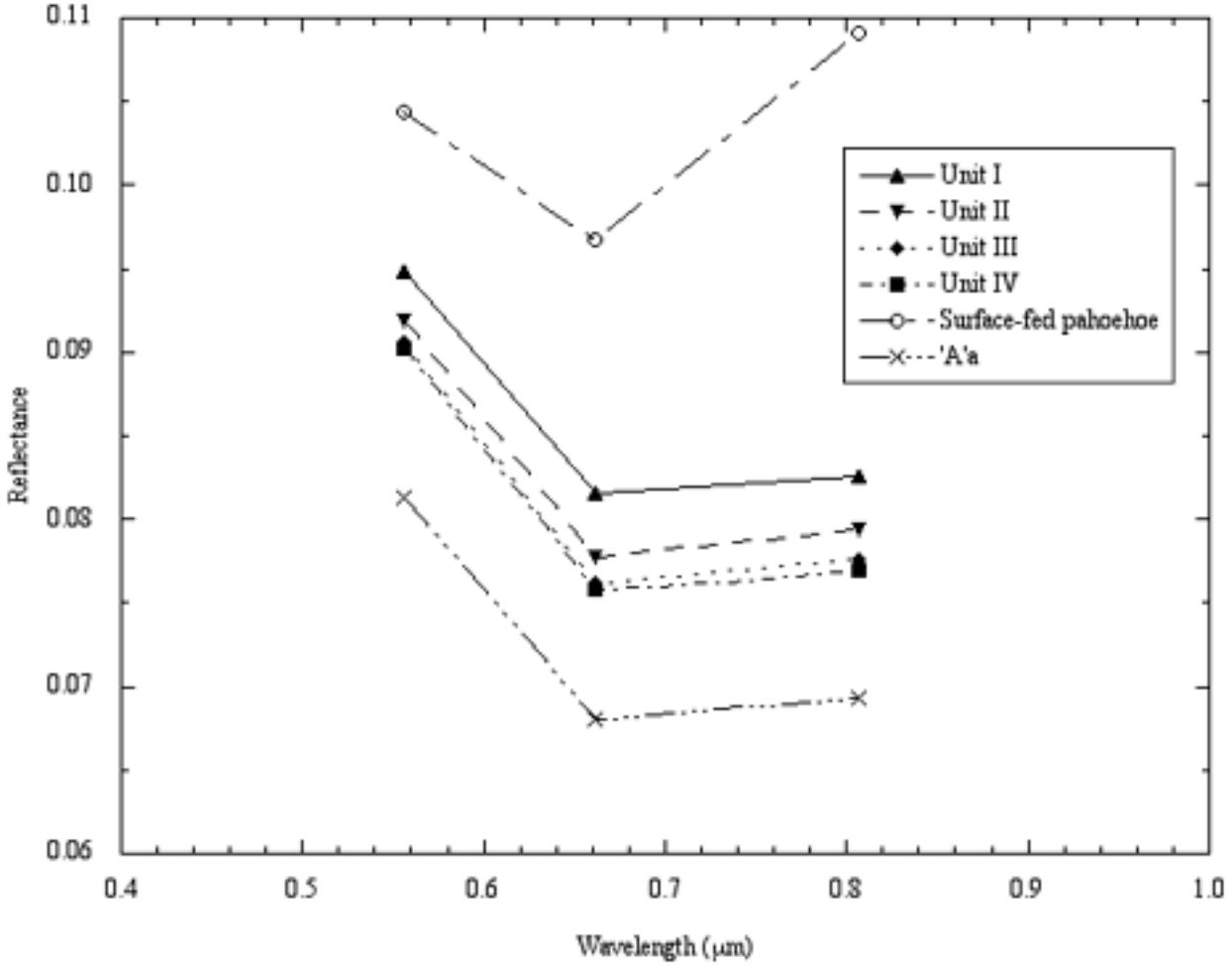

Figure 3.4. Mean reflectance spectra for Mauna Ulu surface units, derived from (a) ASTER, bands 1 to 3, and (b) MASTER, bands 1 to 11.

b

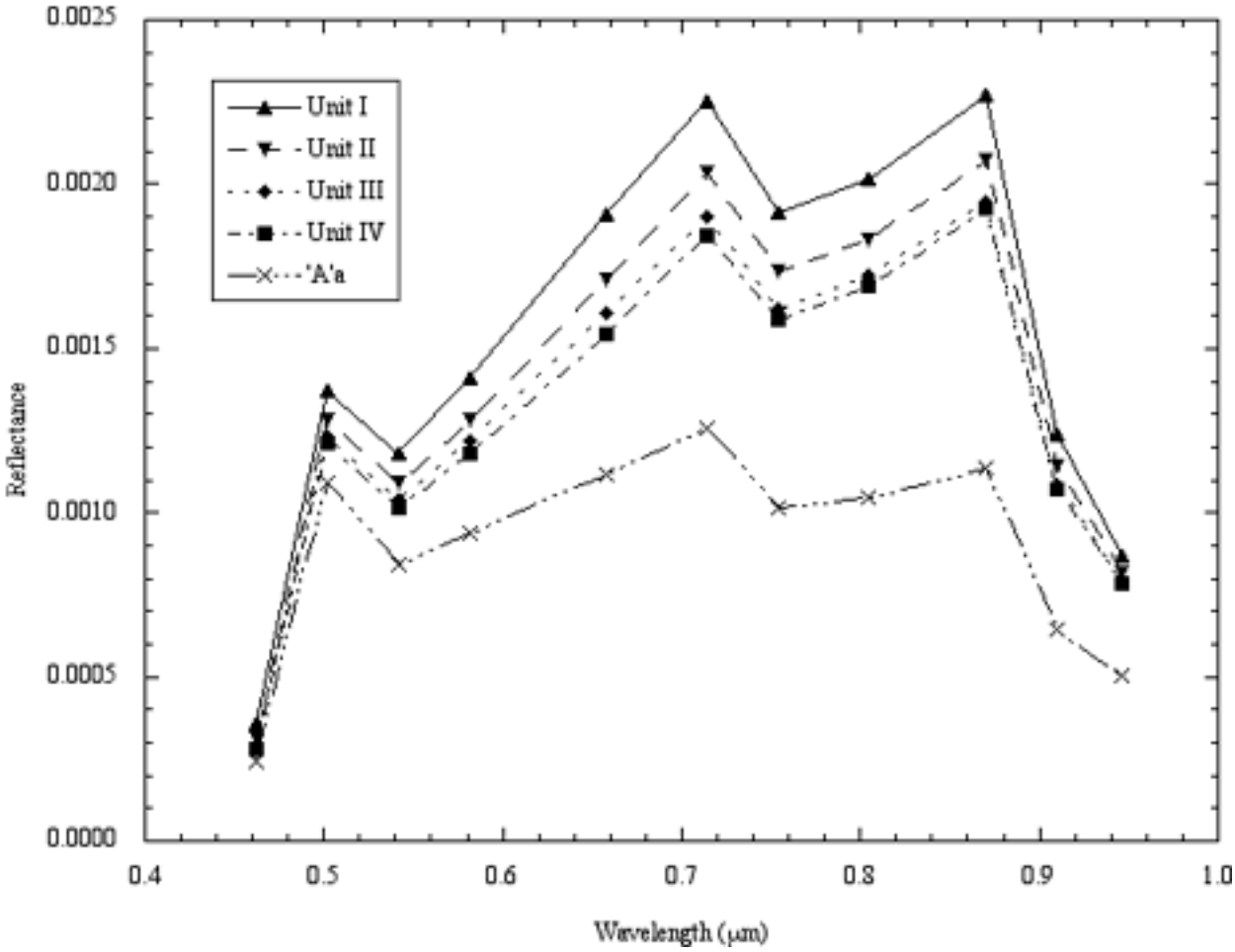

Figure 3.4. (continued)

a

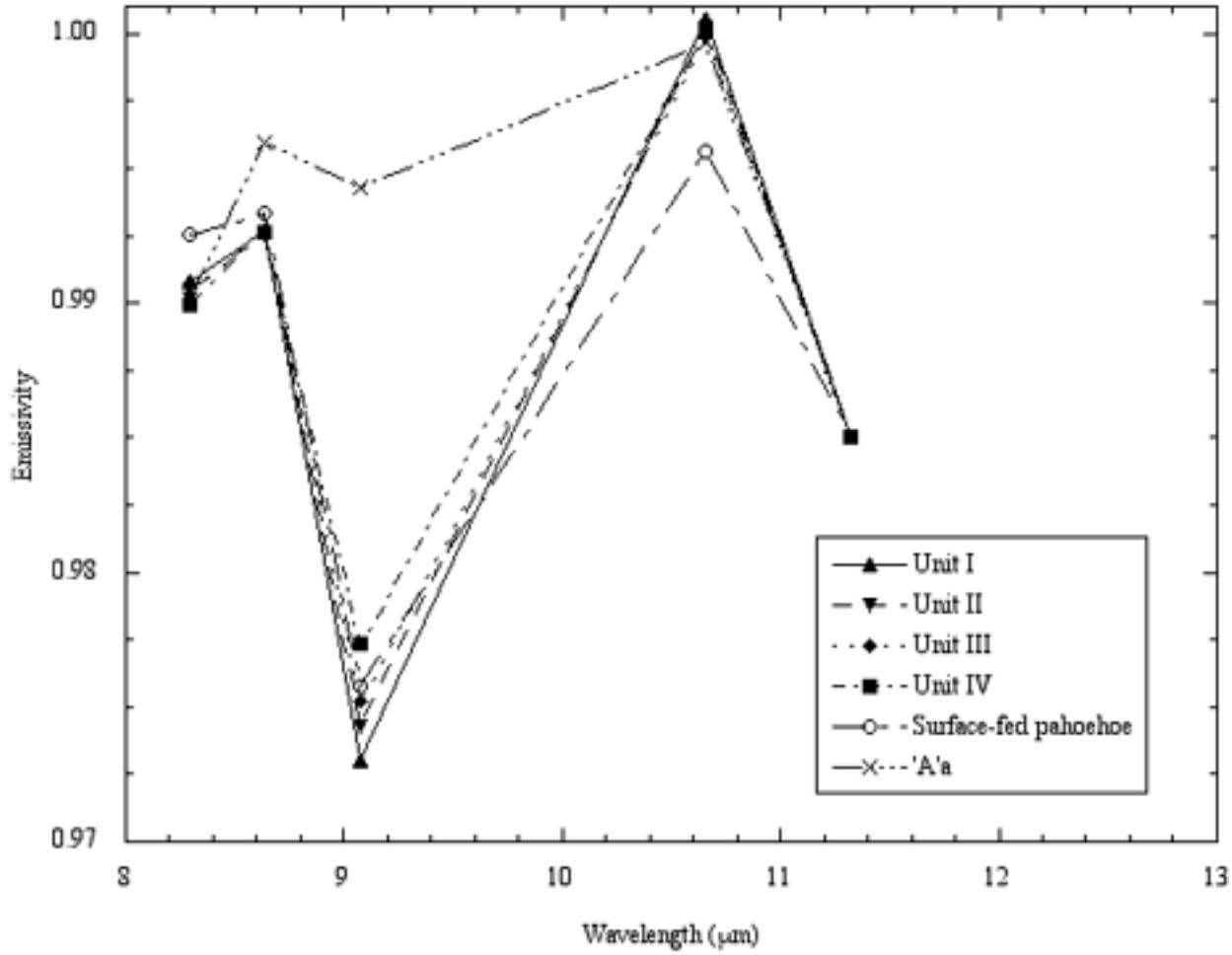

Figure 3.5. Mean emissivity spectra for Mauna Ulu surface units, derived from (a) ASTER, bands 10 to 14, and (b) MASTER, bands 42 to 50.

b

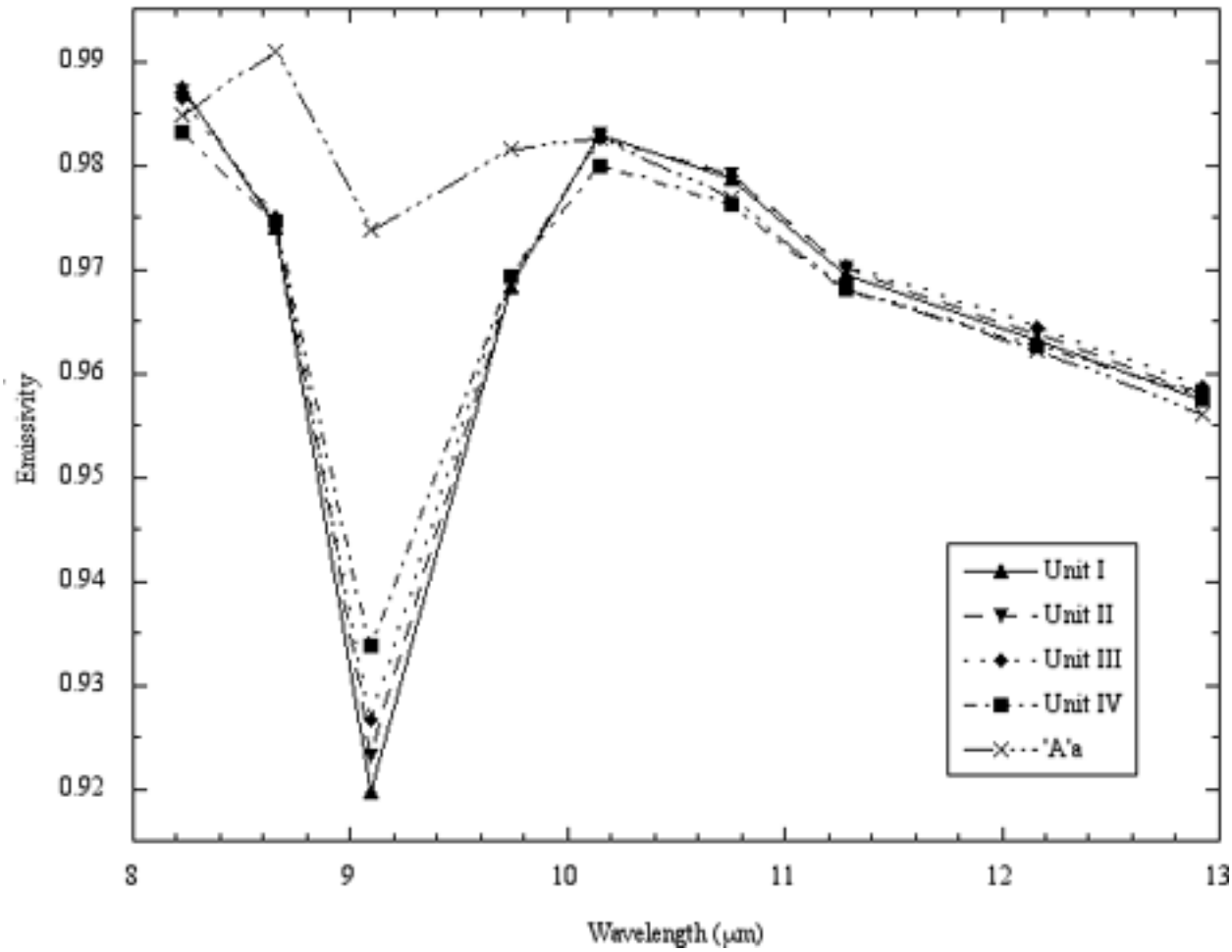

Figure 3.5. (continued)

a

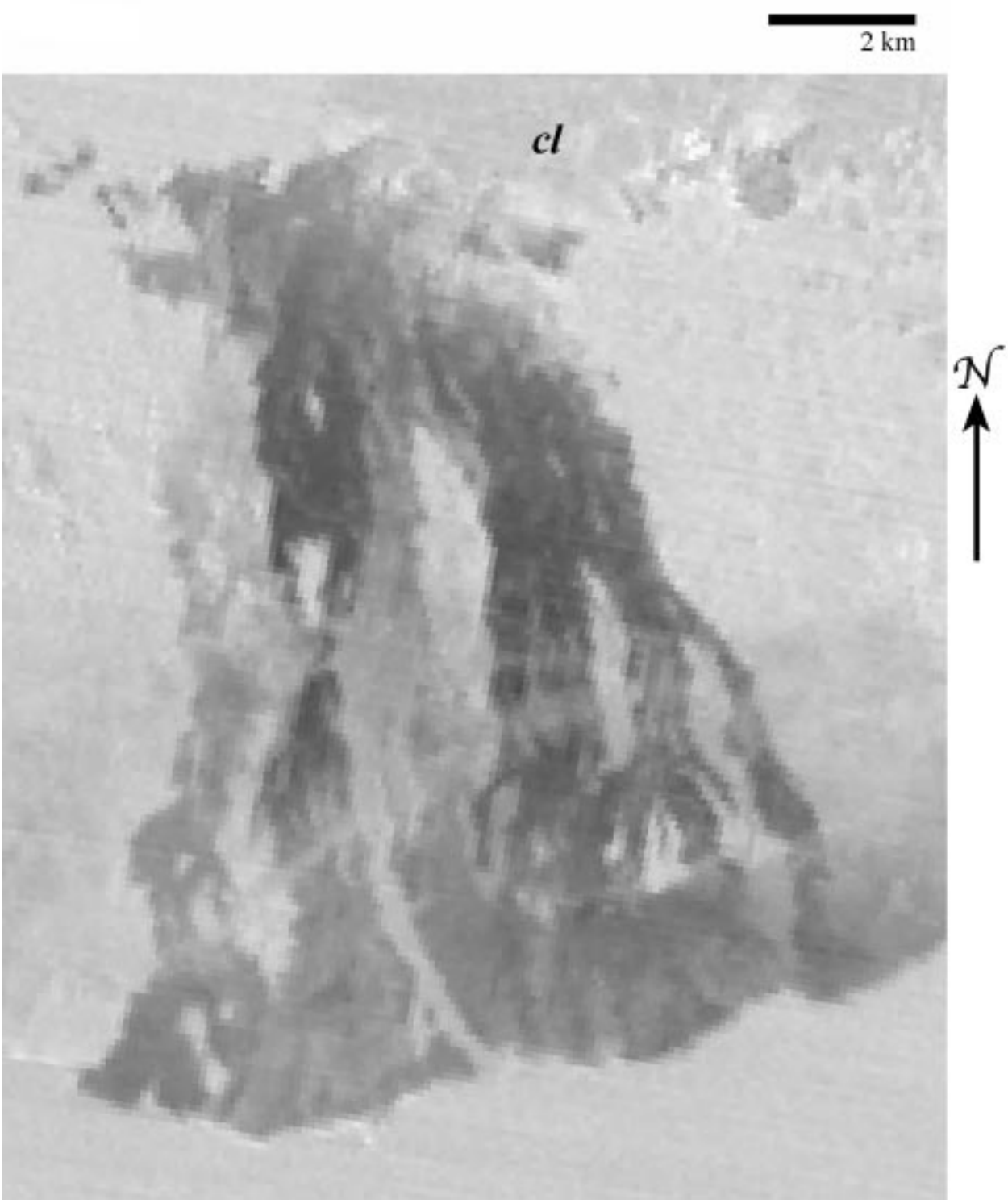

b

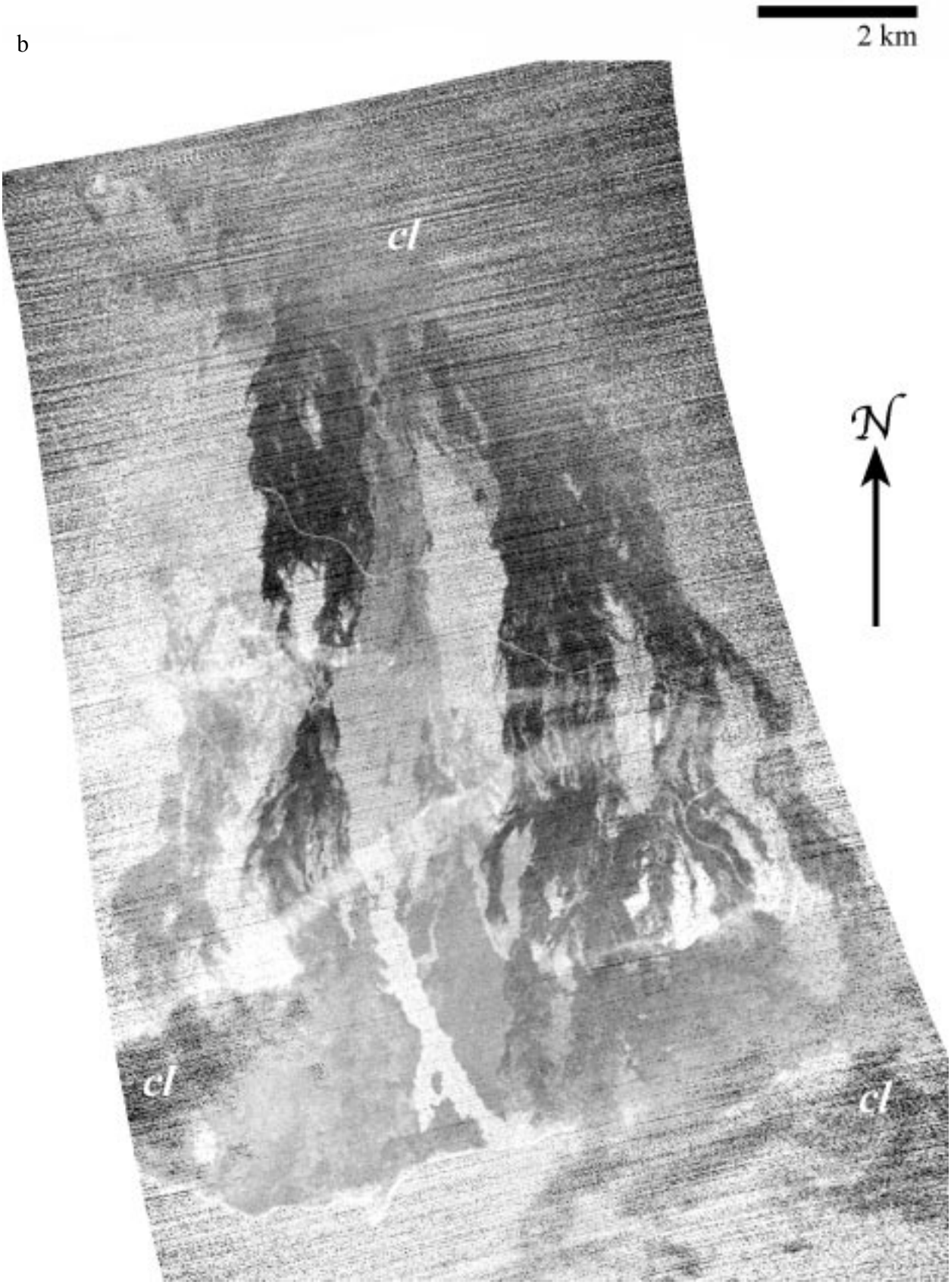

Figure 3.6. (previous) Emissivity-derived small-scale roughness maps of the Mauna Ulu flow field. (a) ASTER-derived roughness map. (b) MASTER-derived roughness map; note that the MASTER data are higher resolution, resulting in greater image contrast. Each grayscale image is displayed as a linear stretch of the proportion of rough (vs. glassy) surfaces, from black (0% roughness) to white (100%). Note that cloud cover appears as noise (*cl*).

an increase in small-scale surface roughness from relatively glassy-surfaced units I and II to the relatively high vesicularity unit III to the disrupted unit IV surfaces (Figure 3.7), consistent with a previous analysis of Thermal Infrared Multispectral Scanner (TIMS) data [Byrnes et al., 2000]. The surface-fed pahoehoe is similar in roughness to unit IV (Figure 3.7). 'A'a has the greatest small-scale roughness of the Mauna Ulu surface units (Figure 3.7), which is comparable to that of the pre-Mauna Ulu surface (Figure 3.6). The mean surface-fed pahoehoe emissivity spectrum (Figure 3.5a) indicates that the unit differs from the other surface units at ~10.7 μm in addition to the 9.1-μm feature.

3.5.5. Significance

The quantitative results presented in Figure 3.4 indicate that the surface units can be distinguished on the basis of characteristic surface reflectance. These results are consistent with

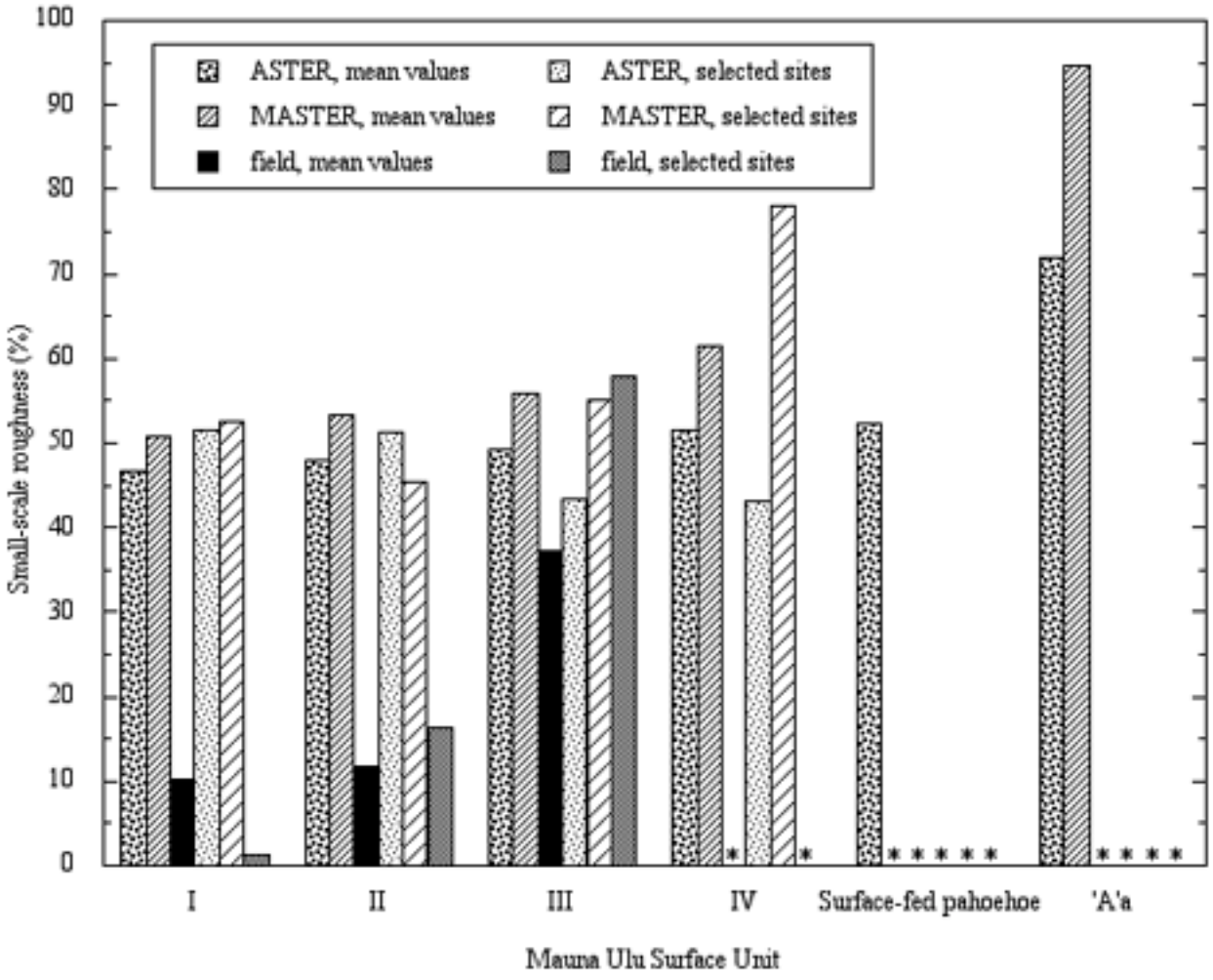

Figure 3.7. Small-scale roughness of Mauna Ulu surface units, expressed as a percent of surface area. Mean unit values as well as point values for four selected sites (see Figure 3.1 inset and section 3.6 text) are compared for field-based vesicularity estimates and emissivity-derived model roughness for ASTER and MASTER. Asterisks indicate data are not available.

the qualitative assessments derived from high-resolution color aerial photographs [Byrnes and Crown, 2001] and field observations that indicate that the abundance of glass and the color at the surface are correlated with lava flow morphology and emplacement processes.

Mean emissivity spectra (Figure 3.5) are consistent with field investigations in this study as well as previous work [Ramsey and Fink, 1997, 1999; Byrnes et al., 2000] that indicates emissivity differences are expected in the surface units due to variations in glass abundance and small-scale roughness. Spectral features associated with the presence of olivine are not observed, consistent with field observations of low exposed phenocryst concentrations (Table 3.1) and the limited areal extent of the most phenocryst-rich surfaces. An assumption of the temperature–emissivity separation technique is that temperature is isothermal within each pixel. Self-shadowing may be significant for unit IV, shelly pahoehoe, and 'a'a due to the nature of their characteristically irregular surfaces, which may create temperature differences within a pixel and produce errors in derived emissivity [Gillespie et al., 1990]. Despite this effect, the results presented herein indicate that the surface units examined have characteristic emissivity spectra that may be used to distinguish them.

The high degree of small-scale roughness for unit IV and surface-fed pahoehoe is interpreted to be due to vesicular flow interiors exposed in disrupted, overturned crust. The high model roughness calculated for the surface-fed pahoehoe may also be related to the depressed emissivity values in ASTER band 13 (~10.7 μm) shown in Figure 3.5a and/or a product of enhanced weathering in the proximal region. The high degree of small-scale roughness observed for pre-Mauna Ulu surfaces reflects a lack of glass, consistent with field observations. The dichotomy between the unit I/II surface texture and the unit III surface texture that is clear in

field observations is not distinct in the mean VNIR and emissivity spectra. Differences between unit I and II in the emissivity data may indicate that unit I displays a lower characteristic degree of crust spallation than unit II, consistent with field data (Table 3.1). Differences in the VNIR data are attributed to the dm-scale morphology (flat sheets vs. undulating toes), consistent with Byrnes and Crown [2001], and may also be related to differences in the characteristic degree of spallation. All four pahoehoe units have similar 9.1-μm features relative to 'a'a (Figure 3.5), which produces greater discriminability between the pahoehoe and 'a'a than between the different pahoehoe units (Figure 6). Differences in contrast between Figures 6a and 6b result from the difference in resolution of the ASTER and MASTER TIR data (90 m/pixel and >10 m/pixel, respectively). The coarser resolution of ASTER yields pixels that sample more surfaces than MASTER pixels, reducing the range of roughness represented within the flow field.

Figure 7 illustrates that the TIR-derived roughness is consistently higher than the field based vesicularity estimates for the unit averages. This indicates that vesicles do not represent the only small-scale roughness elements within the flow field to which TIR data responds.

3.6. Field and remote sensing synthesis

Synthesizing field and remote sensing analyses is paramount to applying field observations made at specific study sites to the entire Mauna Ulu flow field, as well as to using remote sensing for investigations of volcanic processes. To directly compare field observations with remote sensing data, dGPS data were used to select pixels in the coregistered datasets that represent specific field sites.

Four sites were selected to provide a comparison between tube-fed units I-IV as observed in the field and as detected in the remote sensing datasets: site 3.2.a (unit I), site 6.1.a1 (unit II), site 3.1.b (unit III), and site 3.1.c (unit IV). The selected unit I and II examples each display typical unit morphologies as well as complexities due to the transitional nature of the pahoehoe units. The selected unit III and IV sites are the type localities for those units.

3.6.1. Field descriptions of selected sites

Site 3.2.a (~15×25 m) is shown in Figure 3.8 and exhibits a complex unit I surface composed of coalesced toes and small channels and sheets. The surface crust displays bronze-colored, stretched glass filaments with small (mm-scale), dark knobs. In local (dm-scale) areas that have larger knobs, these protrusions are more abundant and less bronzy. The surface crust lacks both vesicles and phenocrysts, but in places displays a splotchy, orange-colored coating/alteration (in portions of flat and ropy areas) and a white-colored coating/alteration (along small cracks). The spallation surface, representing ~5% of the exposure, displays ~25% vesicles (up to 3 mm, but typically 0.5 mm) and <1% phenocrysts (≤3 mm long). This unit I exposure was fed from a large, ropy channel (over a lava tube) and fed toey lobes downflow. The site apparently experienced minor flow inflation as indicated by fractures in the unit surface and maximum local relief (fracture offset) of ~22 cm.

Site 6.1.a1 (~15×10 m) is shown in Figure 3.9 and exhibits discrete pahoehoe toes that are transitional to coalesced toes at the site 6.1.a unit I exposure. The unit II toes are several decimeters to ~1 m in size, with larger toes tending to be more elongate. The surface crust displays bronze-colored, stretched glass filaments and dark knobs; vesicles are uncommon (<5%)

a

Figure 3.8. Example of unit I pahoehoe at site 3.2.a. (a) Site overview, showing coalesced toes and small sheets in foreground overlying an older Mauna Ulu ropy channel that represents a transition from unit I to unit IV. Fractures and offset crust that are evident in the photograph are interpreted to result from minor flow inflation. (b) Unit detail, showing a smooth, glassy, relatively non-vesicular surface; small areas displaying the spallation surface (*sp*); small surficial cracks associated with a white surface coating or alteration; and dark fractures of the crust that are associated with cooling and minor flow inflation. Note that the top scale bar is in inches and the lower scale bar is in centimeters.

b

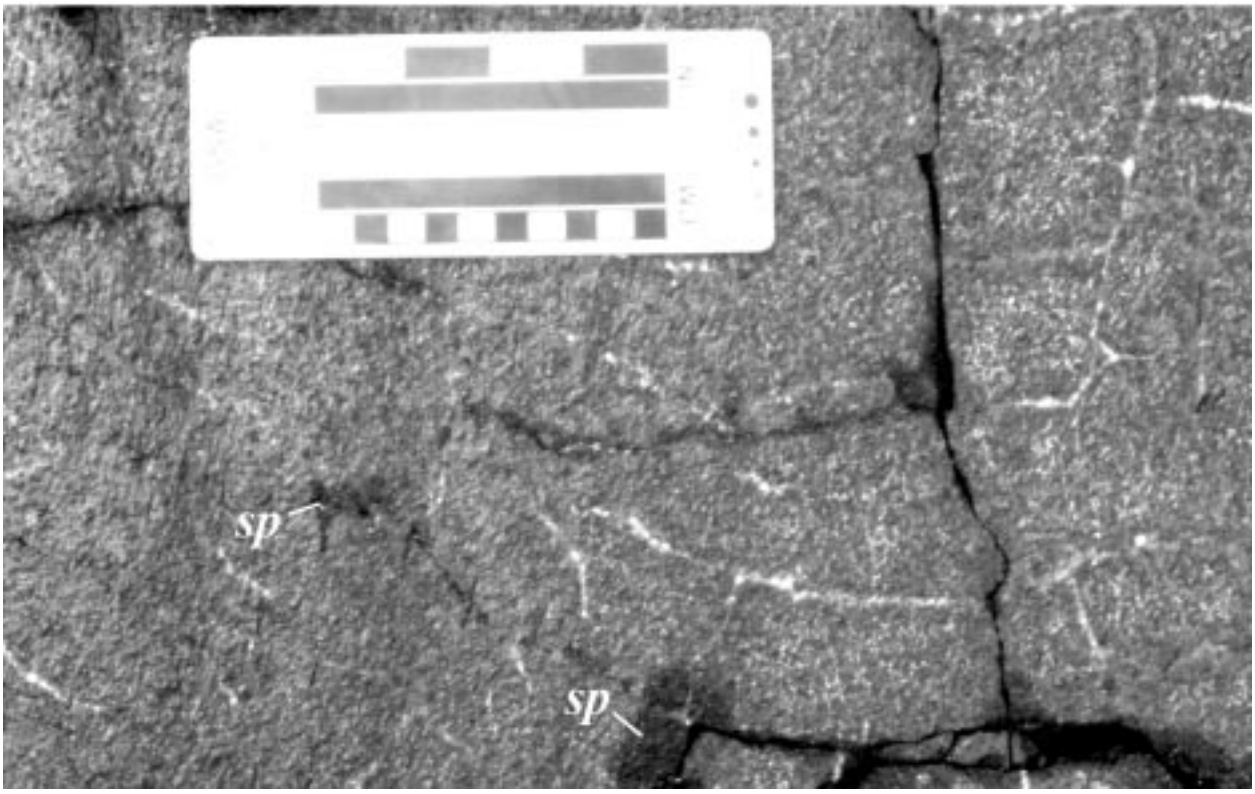

Figure 3.8. (continued)

a

Figure 3.9. Example of unit II pahoehoe at site 6.1.a1. (a) Site overview, showing discrete toes (near M. Ramsey) transitioning (to the left) to coalesced toes forming a unit I surface. (b) Unit detail, showing spallation surface with a small portion of the glassy surface crust at the lower right (*sc*). Scale bar is in centimeters.

b

Figure 3.9. (continued)

and small (1-2 mm). Approximately half of the surface crust has been spalled, revealing a surface with more abundant vesicles (~30%) of the same size. Phenocrysts and surface coatings/alteration are absent. Inflation occurred, as manifested in a large tumulus from which squeeze-ups emanate.

The site 3.1.b (~15×30 m) unit III toes (Figure 3.10) appear to be the last-emplaced surface unit locally, fed as a breakout from the distal end of the site 3.1.c unit IV channel. Toes are decimeters to several meters in length; smaller toes tend to be smooth whereas larger toes tend to be ropy. The unit III surface crust appears dark with a vitreous luster. The surface displays relatively abundant (~40%), elongate vesicles that are 1-2 mm long. Olivine phenocrysts are present (<5%) and up to 3 mm long. Most of the surface crust has been spalled (90%), exposing a dark, highly vesicular (60%) surface. Vesicles are typically 1 mm across, but range up to 0.5 cm. Olivine phenocrysts make up ~10% of the spallation surface and are up to 2 mm long.

The site 3.1.c (~75×45 m) unit IV channel (Figure 3.11) is highly variable, including the following: slabs that display a flat, bronzy, stretched-glass unit I/II-type surface texture; slabs with centimeter-scale compressional folds displaying glassy surfaces; slabs of overturned crust that are gray-brown and non-vesicular; reddish, vesicular 'a'a clinkers; and slabs displaying unit III-type surface crusts and spallation surfaces. Small pieces of wind-blown reticulite have accumulated at the site as well.

a

Figure 3.10. Example of unit III pahoehoe at site 3.1.b. (a) Site overview, showing toes that are relatively thick, commonly ropy, and accumulate to form "centrally ridged" lobes [Crown and Baloga, 1999]. Site 3.1.c unit IV exposure is visible as disrupted, dark plates in photo mid-ground (*u4*), and Chain of Craters Road is visible along the pali in the background. (b) Unit detail, showing rough surface crust (*sc*) and highly vesicular spallation surface (*sp*). Scale bar is in centimeters.

b

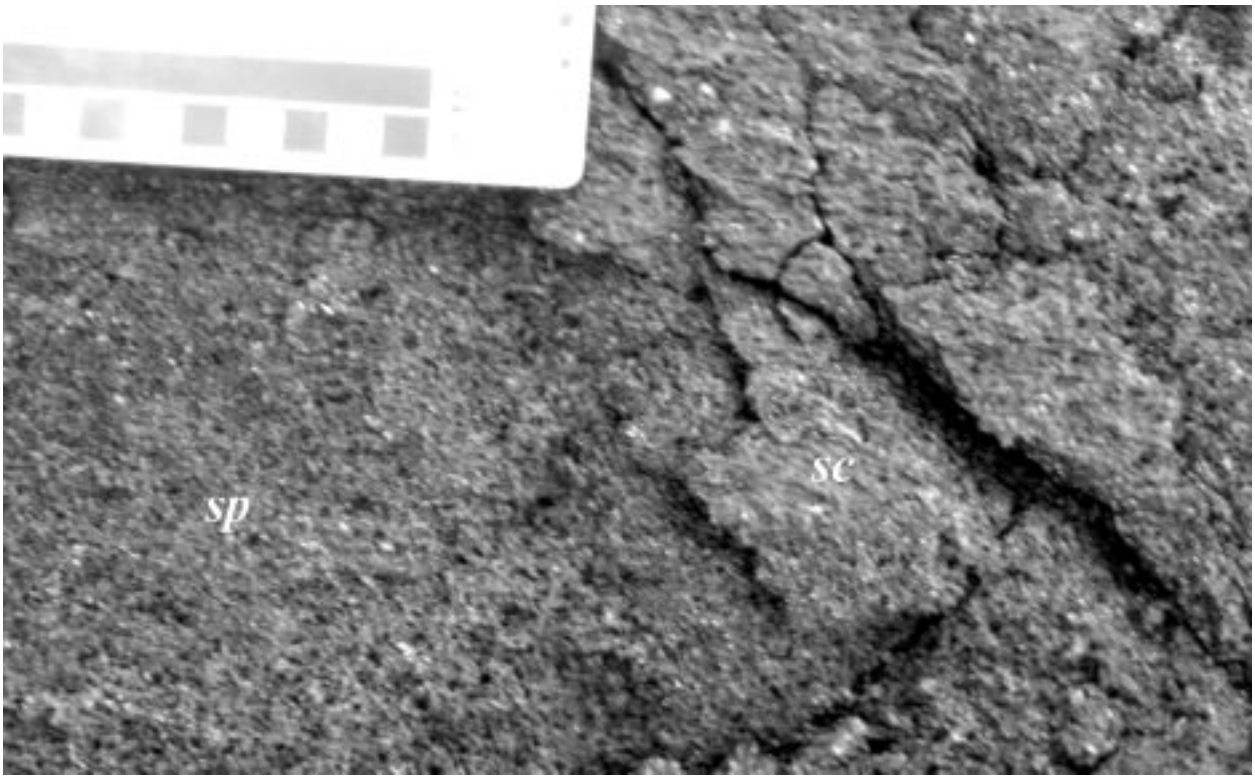

Figure 3.10. (continued)

Figure 3.11. Example of unit IV pahoehoe at site 3.1.c. Unit overview shows disrupted surface displaying primary unit I/II textures in smooth and ropy plates with glassy surfaces, primary unit III textures in dark plates with rough surfaces, and 'a'a texture on clinkers.

3.6.2. Remote sensing characteristics of selected sites

Point spectra for the four selected sites are shown in Figure 3.12. These spectra do not display the simple relationships observed in the mean unit spectra (Figures 3.4-3.5). Specifically, in the ASTER VNIR data, the pixel containing the unit III exposure at site 3.1.b has a higher reflectance at all three wavelengths than the other three site pixels. The unit I and IV sites (3.2.a and 3.1.c, respectively) display similar reflectance, and the unit II site (6.1.a1) has the lowest reflectance at all wavelengths. ASTER emissivity spectra are opposite of the mean emissivity trend – units III and IV display the most prominent 9.1-μm feature, followed by unit II and unit I. The MASTER VNIR data indicate that overall the unit I site is the brightest pixel of the four, followed by the unit III and II sites, and finally the unit IV site, although the progression is not consistent at all wavelengths. The TIR-derived point emissivity spectra also depart significantly from the mean spectra, which is reflected in the site point values of small-scale roughness (Figure 3.7). Roughness of the selected sites does not show the simple increase from unit I to II to III to IV that is indicated by the field data and mean TIR-derived values. Additionally, the mean and point TIR-derived roughness values are significantly higher than field-based estimates of vesicularity.

3.6.3. Significance

The spectral data for individual sites diverge significantly from the trend established by mean unit data. This is interpreted to be due to the selected pixels sampling multiple types of surfaces. For example, the site 3.1.c unit IV exposure is adjacent to a kipuka of exposed pre-Mauna Ulu basalt. The pre-eruption surface is visibly much brighter than the Mauna Ulu basalt

a

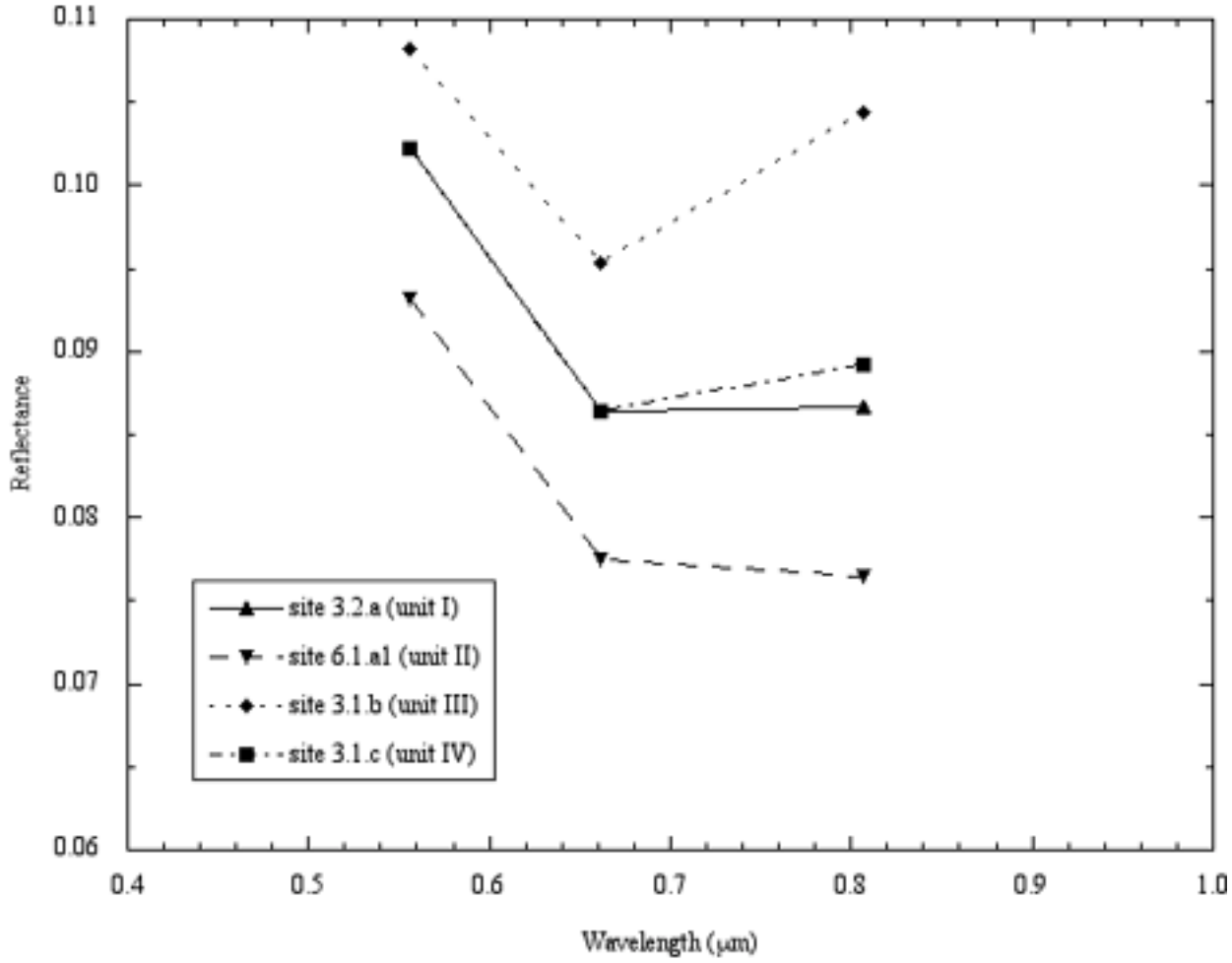

Figure 3.12. Point spectra of the four selected sites (see Figure 3.1 inset and section 3.6.1 text). (a) ASTER VNIR-derived reflectance, bands 1 to 3. (b) MASTER VNIR-derived reflectance, bands 1 to 11. (c) ASTER TIR-derived emissivity, bands 10 to 14. (d) MASTER TIR-derived emissivity, bands 42 to 50.

b

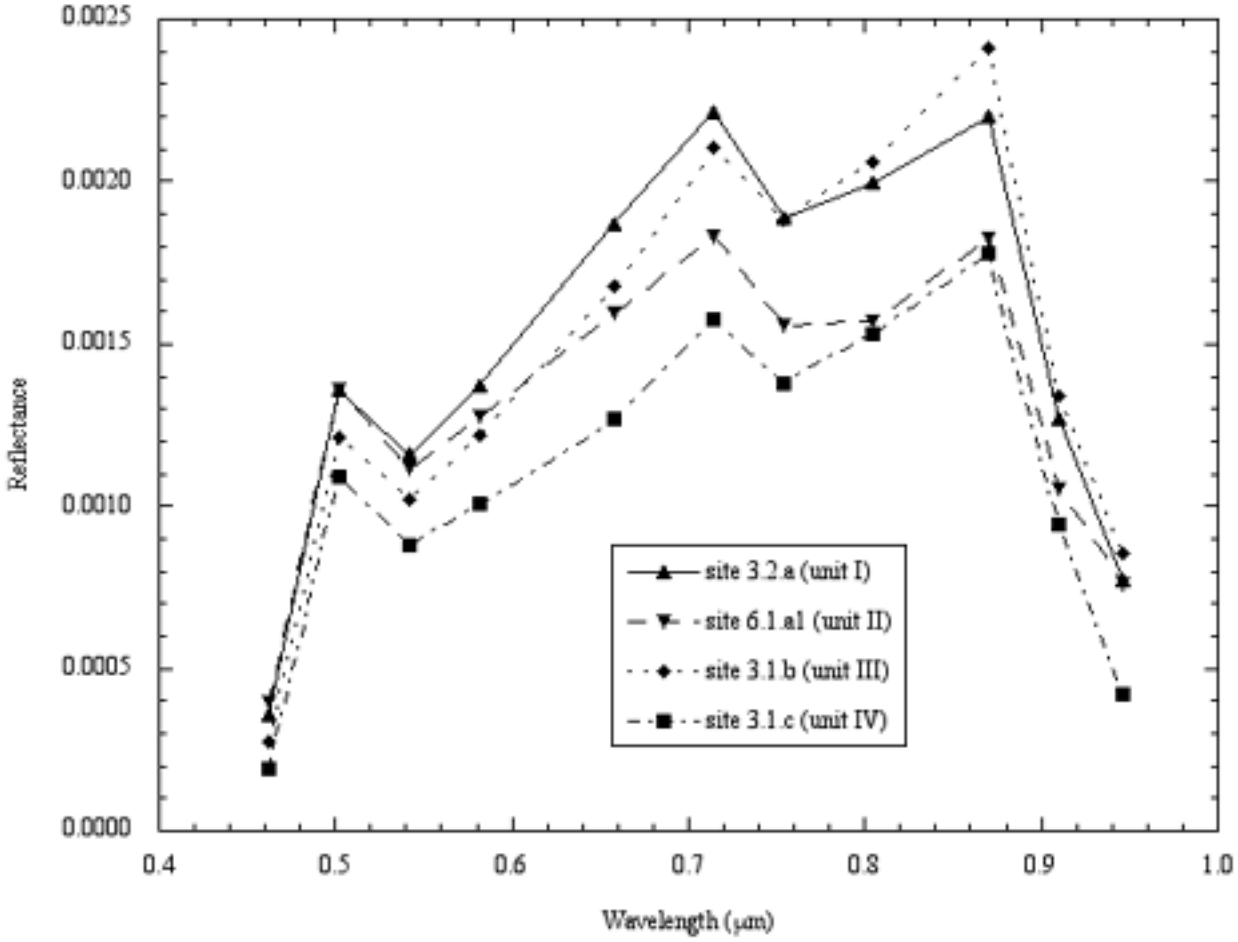

Figure 3.12. (continued)

c

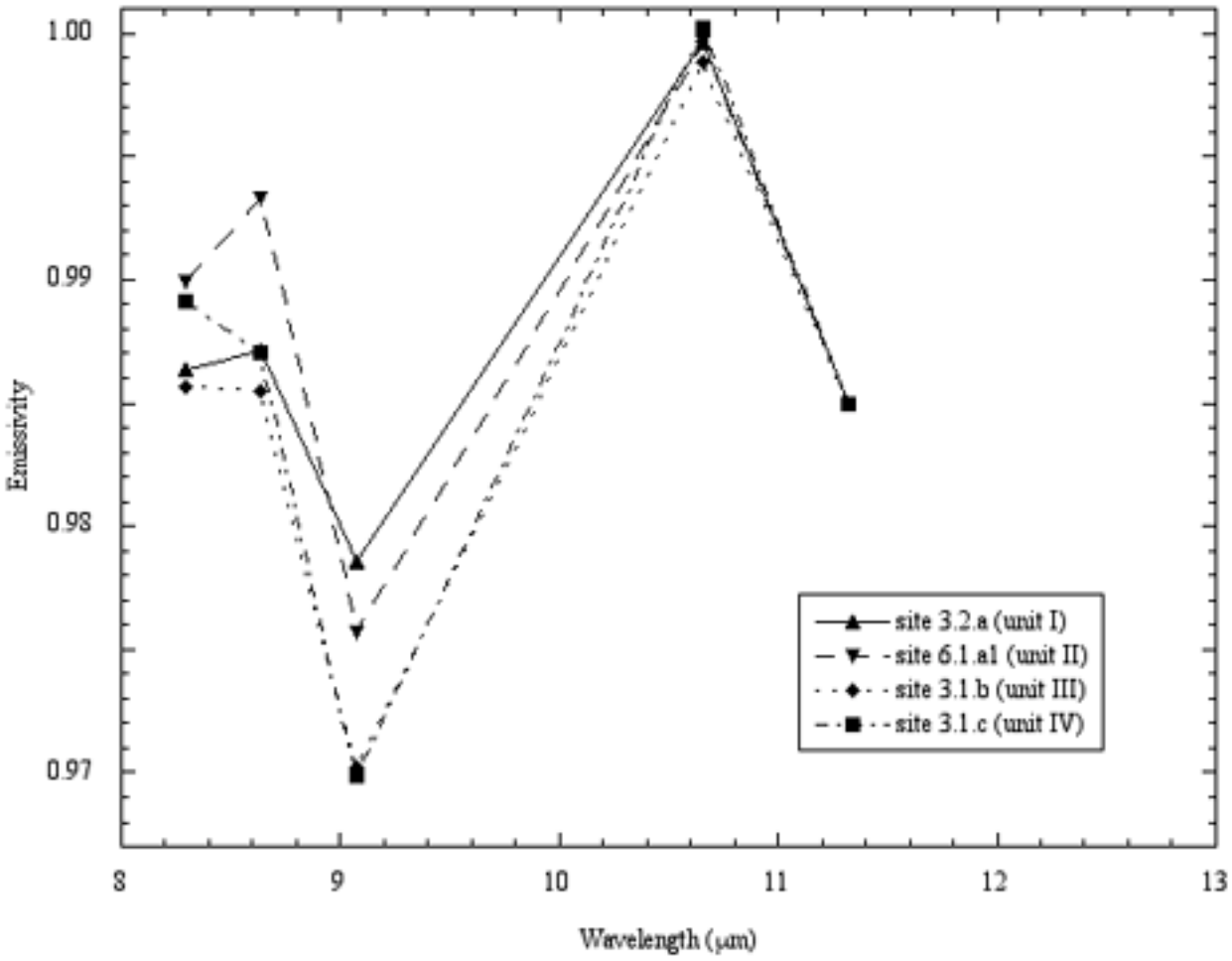

Figure 3.12. (continued)

d

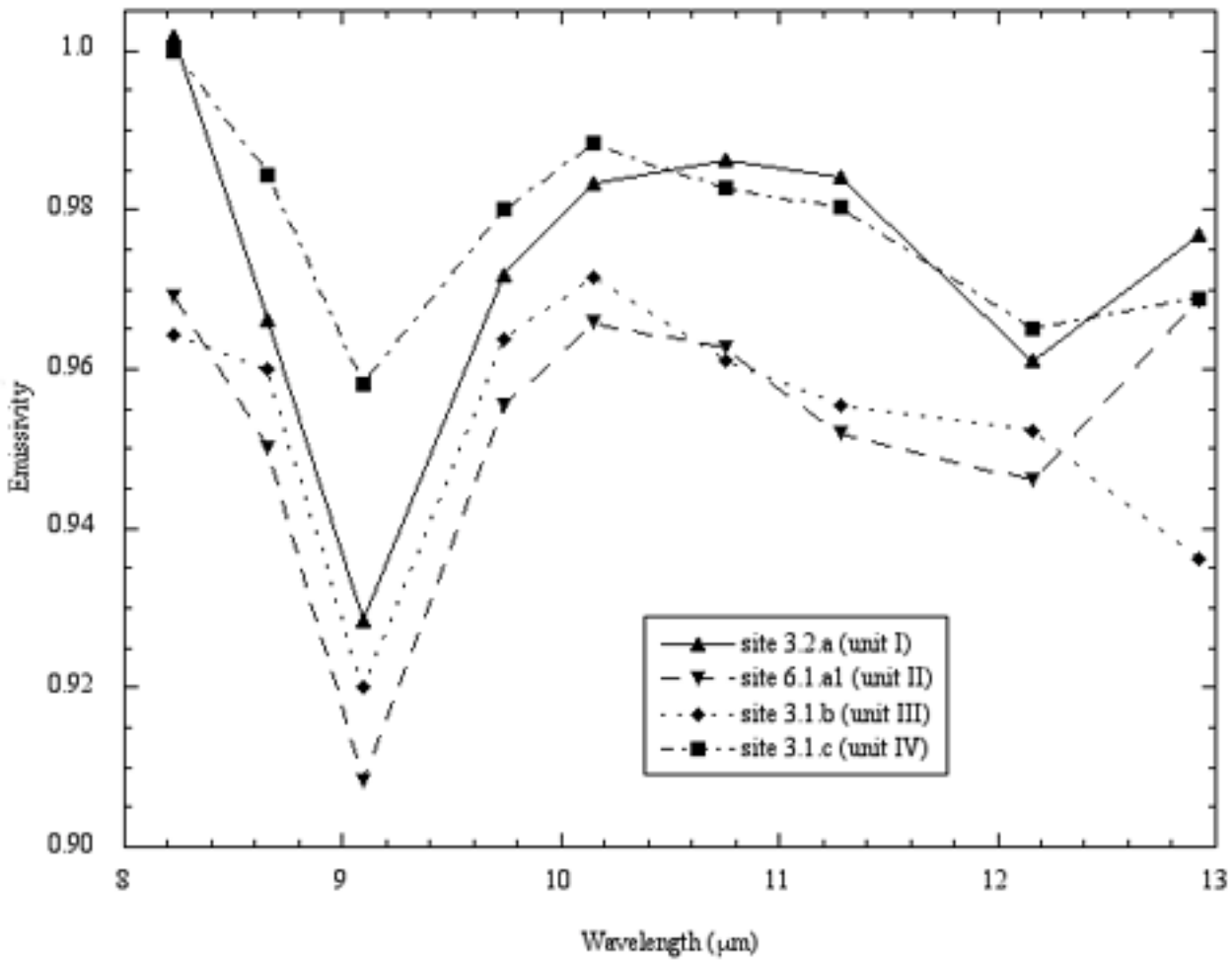

Figure 3.12. (continued)

due to more extensive weathering of the surface (consistent with observations by Lockwood and Lipman [1987] of basalt weathering on Mauna Loa). Mixing of the pre-eruption surface with the unit IV surface within the pixel accounts for increased reflectance in the ASTER VNIR data and increased roughness in the MASTER TIR-derived data. Differences between the ASTER and MASTER VNIR point data are due, at least in part, to differences in the actual pixel footprints and may be amplified by small errors in coregistration. The ASTER and MASTER TIR data have very different spatial extents, which causes even greater differences in derived emissivity and small-scale roughness. Mixed pixels will tend to cause single-point spectra to represent averaged values. This effect is illustrated in Figure 3.7 in that roughness values derived from the remote sensing data are fairly consistent for units I-III relative to that observed in the field, because the unit I and II sites are in pixels that include rougher surfaces and the unit III site is within a pixel that includes smoother surfaces. The TIR-derived roughness values are in most cases higher than the field-based vesicularity estimates, although no consistent difference in values is present (+51% to -3%). This is interpreted to indicate that small-scale roughness elements other than vesicles contribute to the emissivity spectra, such as observed mm-scale knobs and ridges, and other surface irregularities such as small-scale fractures associated with flow inflation.

Surface coatings and/or alteration may affect the emissivity spectra at locales, although this effect, if present, does not appear to affect the separability of unit surfaces based on the mean spectra. Although it has been documented that surficial coatings and/or alteration affect TIR signatures of basalt, they may enhance the glass signature if composed of amorphous silica, or mask the feature if composed of hematite or palagonite [see Figure 2 of Kahle et al., 1988] or halite from sea spray (refer to the ASTER spectral library, http://speclib.jpl.nasa.gov).

3.7. Discussion

3.7.1. Comparison and application of ASTER and MASTER datasets

The pahoehoe morphologies examined herein (sheets, channels, and toes) are expressed within surface units of the Mauna Ulu flow field at the meter scale. Both the ASTER and MASTER pixels are much larger than this (≥15 m/pixel and >10 m/pixel, respectively) and will therefore typically sample multiple surface units, as occurred in the site examples discussed in section 3.6. This indicates that individual units of small areal extent are not easily identifiable in spectra derived from individual pixels. Interpretation of remote sensing data is further complicated by the morphologic variability within a given flow regime due to changes in factors such as local supply and substrate as well as different degrees of spallation and flow inflation. However, the mean unit spectral data suggest that the units defined for the Mauna Ulu flow field have characteristic spectra. These spectra are better defined by increasing the ratio of signal from a surface unit to noise of other unit surfaces, accomplished by averaging a larger number of pixels as discussed in sections 3.5.3-3.5.5. Thus, within the Mauna Ulu flow field, these remote sensing datasets may be used to constrain the dominant surface unit at a locale as well as characterize changes that occur in the distribution of units within the flow field.

In addition to spatial resolution, an important factor in application of remote sensing datasets is the spectral resolution. ASTER collects 3 bands from 0.4-1.0 μm and 5 bands from 8-13 μm, compared with 11 bands and 9 bands, respectively, for MASTER. Additional bands in the MASTER VNIR-region are advantageous because they allow compilation of a near-true color image of the flow field, which is useful for comparison with field observations. Additional bands in the MASTER TIR-region are beneficial in order to better constrain the depth of the absorption feature present at 9.1 μm. Despite the additional TIR bands, units with high

abundance of olivine phenocrysts in the Mauna Ulu flow field do not appear to produce identifiable spectral features because of the limited spatial extents of phenocryst concentrations relative to the spatial resolution of the data.

3.7.2. Distribution of surface units within the Mauna Ulu flow field

Several large-scale trends in emplacement are apparent within the Mauna Ulu flow field, based on synthesizing the field and remote sensing analyses presented herein. ASTER and MASTER VNIR data suggest that the proximal surface units (fountain-fed and shelly pahoehoe) are similar and relatively homogeneous, except for the significant chemical alteration that is present immediately adjacent to the Mauna Ulu vent. Tube-fed pahoehoe units I-IV and lobes of 'a'a dominate the medial and distal portions of the flow field. Small-scale roughness data derived from the ASTER and MASTER TIR data support the interpretation that the proximal region is relatively homogeneous. The highly-altered material nearest the vent is not evident in the TIR nor roughness data, presumably because the ASTER data lack sufficient spatial resolution and the MASTER data have sufficient cloud cover to mask an alteration signature.

The small-scale roughness model results indicate that the smoothest areally extensive surfaces within the Mauna Ulu flow field are located in interior portions of the medial region, with roughness increasing toward the flow field margins and increasing downflow as the tube-fed lava experienced the topography associated with the steep pali, which also tends to produce 'a'a flows. These effects are presumably caused by increased cooling of lava away from the master tube system toward the flow field margins and progressive downflow disruption of the lava flows. Cooling tends to be limited within the master tube system; Swanson [1973] indicates that lava flowing through the Mauna Ulu master tubes experienced minimal heat loss and did not

display progressive cooling downslope. However, it is expected that flow velocities decrease as lava is transported away from the main lava tube segments in the smaller distributary lava tubes, promoting storage and allowing for increased cooling of some proportion of the lava. Downflow disruption of the flows may be related to increased hydraulic head below the pali system leading to greater degrees of flow inflation. A potential complicating factor may also affect the derived emissivity, however. Toward the coast, sea spray may add salt to the flow field surface, and may be responsible for the white surface coatings/alteration observed at some sites (e.g. site 3.2.a, section 3.6.1, Figure 3.8b). Halite lacks a strong absorption at 9.1 μm (refer to the ASTER spectral library) and thus may serve to mask the glass spectral feature. Resolution of these issues may be accomplished with a field spectrometer to detail spectral changes across and along the flow field.

3.8. Conclusions

The Mauna Ulu flow field exhibits surface units that display a range of morphologies and textures resulting from differences in flow emplacement conditions, including four tube-fed pahoehoe units (I-IV), near-vent surface-fed pahoehoe (shelly and fountain-fed), and 'a'a. Characteristic variations related to differences in emplacement processes between these units are identifiable in the field as well as in remotely sensed VNIR and TIR spectra. Visible-wavelength characteristics of the surface units are dependent on the color, abundance of glassy surface crust, and nature of dm-scale undulations and larger-scale irregularities based on field observations. TIR-derived emissivity data are responsive to variations in glass abundance and small-scale roughness, and may be used to calculate the abundance of small-scale surface roughness

elements (such as vesicles), which is related to the thermal and degassing history of the lava. The wide range in characteristics observed in the field indicates that each of the units may be produced under a range of conditions, consistent with the gradational nature of the units observed within the flow field. The primary pahoehoe morphologies are associated with two types of surface textures, although spallation of the surface crust complicates both the VNIR and TIR signatures of the units. The unit characteristics may be used to infer flow regimes and cooling histories within the flow field in order to understand emplacement. For example, flows that display relatively high reflectance and low emissivity-derived roughness tend to be hot and fluid during emplacement whereas darker, rougher flows are cooler during emplacement and may result from late-stage emplacement and/or disruption of the flow surface.

Although individual flow units cannot be identified at the resolution of the ASTER and MASTER datasets, the predominant unit morphologies and textures may be ascertained, and several large-scale trends in emplacement are apparent within the Mauna Ulu flow field. The proximal region is characterized by surface-fed shelly and fountain-fed pahoehoe that is relatively homogeneous, except for those flows nearest the vent that are being subjected to chemical alteration due to continued degassing. The surface-fed units are emplaced as large sheets, toes, and channels, and signify relatively high lava supply rates. Medial and distal portions of the flow field display 'a'a and tube-fed pahoehoe. 'A'a becomes more common in association with the steep pali, due to the increased lava strain rate caused by increased flow velocity. Tube-fed pahoehoe is emplaced as sheets, toes, and channels that display different small-scale surface characteristics due to differences in cooling, degassing, and crystal formation and/or settling. Tube-fed pahoehoe units (I-IV) display an overall trend of increased small-scale surface roughness toward the flow field margins and away from the vent, suggested to result

from cooling and flow disruption. Application of the methodology presented herein to flows in different settings may be used to further constrain the effects of eruption parameters (supply rate, eruption style, etc.) and setting (transport network, topography, cooling environment, etc.) on the emplacement of lava flow fields.

Chapter 4

Morphology, Stratigraphy, and Surface Roughness Properties of Venusian Lava Flow Fields

4.1. Introduction

Lava flow fields on Venus are globally distributed [Saunders et al., 1992] and are commonly associated with volcanic shields and domes, coronae, and rifts [Head et al., 1992]. The general characteristics of many flow fields have been described [e.g., Guest et al., 1992; Head et al., 1992; Roberts et al., 1992; Senske et al., 1992; Head et al., 1993; Lancaster et al., 1995; Stofan et al., 2001; Magee and Head, 2001], including gross morphologic and surface roughness properties, geologic and tectonic settings, and large-scale topographic characteristics. Previous analyses of flow margins and surface roughness characteristics of Venusian lava flows suggest the presence of flow surfaces similar to terrestrial pahoehoe and 'a'a [Bruno et al., 1992; Campbell and Campbell, 1992; Campbell and Rogers, 1994; Bruno and Taylor, 1995; Pike et al., 1998]. Lava flow fields may provide constraints on Venusian resurfacing history, for which directional [Basilevsky and Head, 1995; Basilevsky and Head, 2000] and nondirectional [Guest and Stofan, 1999] models have been developed. The directional model is based on the suggestion that the surface records a progression of globally-synchronous volcanic and tectonic events, whereas the nondirectional model suggests that volcanic and tectonic processes occur on regional scales and do not display a simple evolutionary trend. In order to understand styles of volcanism and the evolution of the surface on Venus, the objective of this study is to constrain emplacement processes within lava flow fields on Venus through analysis of flow lobe morphologies, stratigraphic relationships, and radar backscatter characteristics.

4.2. Background

Previous investigations of lava flows have examined morphologies diagnostic of emplacement style and processes, constraining flow field development using terrestrial examples. Walker [1972] distinguishes lava flows based on whether they are divisible into multiple flow units (compound) or are not (simple). These terms were originally applied to small-scale features observed primarily in cross-section; pahoehoe flows are considered to be almost always compound and 'a'a flows are commonly compound, whereas higher viscosity lavas (andesite and dacite) are more typically simple [Walker, 1972]. For a given lava composition, extrusion rate is suggested to be the primary control determining which type of flow is produced, with higher rates favoring simple flow emplacement. Guest et al. [1987] describe constraints on flow morphology that are due to limited supply and to cooling. Volume-limited flows advance until lava supply from the local source ceases. Cooling-limited flows advance until cooling at the flow front is sufficient to prohibit further movement. This may produce overflows and breakouts from the original lobe, which change its gross planform morphology. Planform morphometric properties (average thickness and ratio of maximum width to maximum length) have been related to eruption duration and underlying slope, which is suggested to be independent of flow field size [Kilburn and Lopes, 1988; Lopes and Kilburn, 1990]. Due to the complexity of subsurface transport through multiple paths in compound pahoehoe flow fields, analyses of volume- and cooling-limited flows have been primarily limited to surface-fed lava flows [e.g., Kilburn and Lopes, 1988; Pinkerton and Wilson, 1994].

Morphologic analyses of Venusian lava flows rely largely on synthetic-aperture radar (SAR) data collected during the 1990-1994 Magellan mission. Three radar-mapping cycles resulted in the collection of single-wavelength (S-band, 12.6 cm), single-polarization (HH,

horizontal transmit-horizontal receive) data at ~100 m/pixel for over 98% of Venus' surface. Those data have been resampled to 75 m/pixel in the full-resolution radar mosaic datasets (FMAPs).

A previous survey of large (>50,000 km^2) lava flow fields, termed great flow fields, on Venus focused on overall flow field morphologies, radar textures, and eruptive settings [Lancaster et al., 1995]. Lancaster et al. [1995] developed a morphologic classification of great flow fields based on 50 of the 208 large flow fields identified by Magee [1994; see also Magee and Head, 2001]. Flow fields are described as sheet, transitional, or digitate; digitate flow fields are further classified as apron, fan, or subparallel. The morphologies are attributed to differences in emplacement style, source characteristics, and local topography. The sheet flow field morphology (e.g., from Lauma Dorsa) lacks discrete sub-units and is interpreted to indicate ponded, volume-limited flow emplacement. Transitional flow fields (e.g., Neago Fluctus) are composed of multiple large sheets, creating a more digitate planform and greater length to width ratios than sheet flow fields.

Digitate flow fields (e.g., the lava fan on Derceto Plateau, the southeast flank of Ozza Mons, and the flow fields examined herein) are the most common morphologic type on Venus. They are composed of multiple distinct flow units that are attributed to cooling-limited flow emplacement. The apron and fan types of digitate flow fields were found to have been extruded from centralized sources (such as coronae or clusters of shields) and are distinguished by whether the flow field completely surrounds the source vent (apron) or not (fan), reflecting the local topography. Subparallel flow fields were found to have been emplaced from less centralized sources (such as portions of rifts). It should be noted that sheet and digitate morphologies represent, respectively, simple and compound flows, although the scale of features

for which these terms were defined is drastically different. This is the case because the ability to distinguish flow units within a flow field depends on the type and resolution of data available for flow mapping. Terrestrial studies of flow fields using airborne and spaceborne radar remote sensing data suggest that the ability to discriminate individual lava flow units within Venusian flow fields may not be possible for the smallest scales at which they occur, given the limitations of Magellan SAR resolution and lack of multiple wavelength and polarization data [e.g., Greeley and Martel, 1988; Gaddis et al., 1989; Plaut, 1991]. These studies indicate that features such as 'a'a flows and large-scale topographic elements may be distinguished using radar data; low-backscatter features, such as pahoehoe flows and cinder cones, were not reliably identified.

The classification scheme of Lancaster et al. [1995] is modified in a recent study of the three large Venusian volcanoes Sif, Gula, and Kunapipi Montes [Stofan et al., 2001]. Stofan et al. [2001] divide flow fields into digitate, fan, and sheet types, which are further broken into the following subtypes based on appearance in the Magellan SAR data: dark, bright-intermediate, dark-bright edges, mosaic, hummocky, or complex. The variations in flow planform morphology and surface texture, distribution of these flow field types, and shapes of the volcanoes were examined to constrain the development of each edifice. Planform morphology was related to variations in eruption style, with digitate flows resulting from high effusion rate, short duration eruptions relative to sheet flows. Surface textures evident in the radar data were interpreted to reflect local emplacement processes, such as fracturing of the surface crust during flow. This analysis indicated that the volcanoes developed through emplacement of frequent, short duration, low effusion rate summit eruptions and infrequent, large volume flank eruptions. Previous investigations had suggested that lava flows from a volcanic center display a temporal progression from long, broad sheets to shorter, digitate flows over the duration activity [Keddie

and Head, 1994, 1995]. Volcanic histories determined by Stofan et al. [2001], however, indicate that large sheets and smaller digitate flows are both emplaced throughout the duration of edifice growth, consistent with terrestrial volcanoes.

Previous detailed mapping of Venusian flow fields has been limited. One such study mapped flow fields in Kawelu Planitia around Sekmet Mons, with intra-flow field mapping conducted for Strenia Fluctus [Zimbelman, 2000]. From that study, it was concluded that flows within Strenia Fluctus emanate from multiple sources, are interfingered, and that at least some flows are compound. No obvious pattern in flow field stratigraphy was observed.

4.3. Methodology

For the current study, lava flow fields were chosen that display numerous discrete lobes and exhibit a significant range of radar brightness, giving preference to those imaged at similar incidence angles to terrestrial airborne radar (~30-45°). Five examples (Figure 4.1) were selected that are covered well in the Magellan cycle-1 (left-looking) FMAPs, include rift and centralized vents, and represent a diversity of geologic and tectonic settings in various regions across Venus: Turgmam Fluctus, Zipaltonal Fluctus, the Tuli Mons/Uilata Fluctus flow complex, the Var Mons volcanic center, and Mylitta Fluctus (Figure 4.2). Based on stratigraphic relationships, these flow fields represent some of the most recent resurfacing (locally to regionally) within the extensive lowland plains [e.g. Crown et al. 1994, 2002b; Zimbelman, 2000; Rosenberg and McGill, 2001], providing important constraints on the development of volcanic surface units.

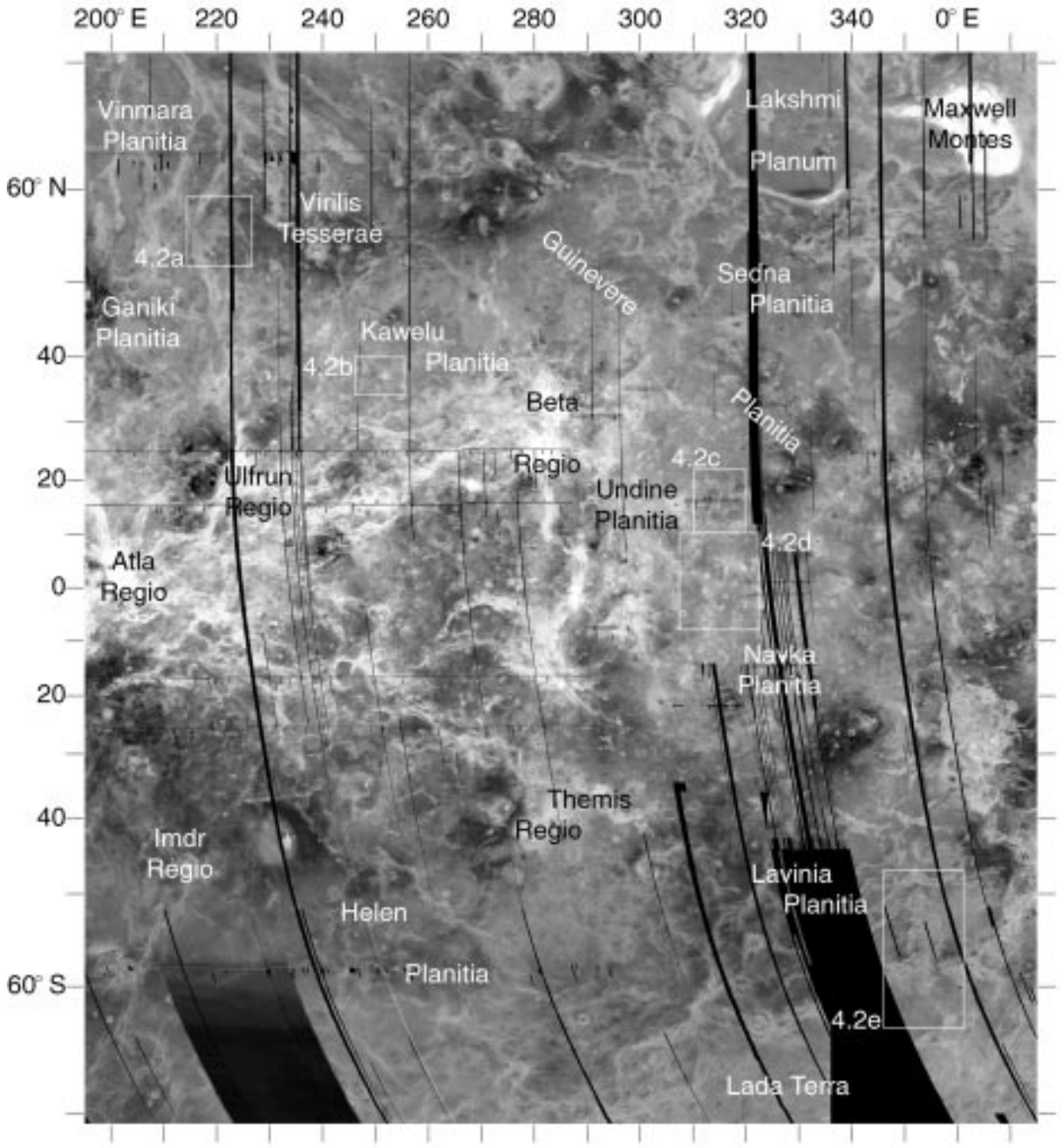
200° E
220
240
260
280
300
320
340
0° E
60° N
40
20
0
20
40
60° S
Vinmara Planitia
Virilis Tesserae
4.2a
Ganiki Planitia
Kawelu Planitia
4.2b
Guinevere Planitia
Lakshmi Planum
Maxwell Montes
Sedna Planitia
Beta Regio
Ulfrun Regio
4.2c
Undine Planitia
4.2d
Atla Regio
Navka Planitia
Themis Regio
Imdr Regio
Helen Planitia
Lavinia Planitia
4.2e
Lada Terra

Figure 4.1. (previous) Locations of venusian flow field study sites. Numbered boxes refer to subsequent figures: 4.2a=Turgmam Fluctus, 4.2b=Zipaltonal Fluctus, 4.2c=Tuli Mons/Uilata Fluctus complex, 4.2d=Var Mons flow field, 4.2e=Mylitta Fluctus. Base map is a Mercator projection Magellan cycle-1 FMAP, created using the NASA Planetary Data System MAP-A-PLANET website (http://pdsmaps.wr.usgs.gov/maps.html). North is to the top of all images in subsequent figures.

Figure 4.2. (following) Images of venusian flow fields (from left-looking Magellan cycle-1 FMAPs, Mercator projection), created using MAP-A-PLANET. Boxes show locations of subsequent figures, which all have sinusoidal projections. (a) Turgmam Fluctus (figure extents are 59.3-51.9° N, 214.5-226.6° E). (b) Zipaltonal Fluctus (figure extents are 39.9-34.3° N, 246.2-255.2° E). Intermediate-size construct (~20 km diameter) is partially buried by Zipaltonal flows (see Figure 4.12a). (c) Flow complex composed of Uilata Fluctus and Tuli Mons flows (figure extents are 21.8-10.5° N, 310.3-319.7° E). *TM* marks the location of Tuli Mons; *UF* indicates the highest point on the edifice associated with Uilata Fluctus. (d) Var Mons flow field (figure extents are 10.2° N-7.8° S, 322.3-307.5° E). (e) Mylitta Fluctus (figure extents are 47.2-63.7° S, 346.2-361.1° E). *TP* marks Tarbell Patera.

a

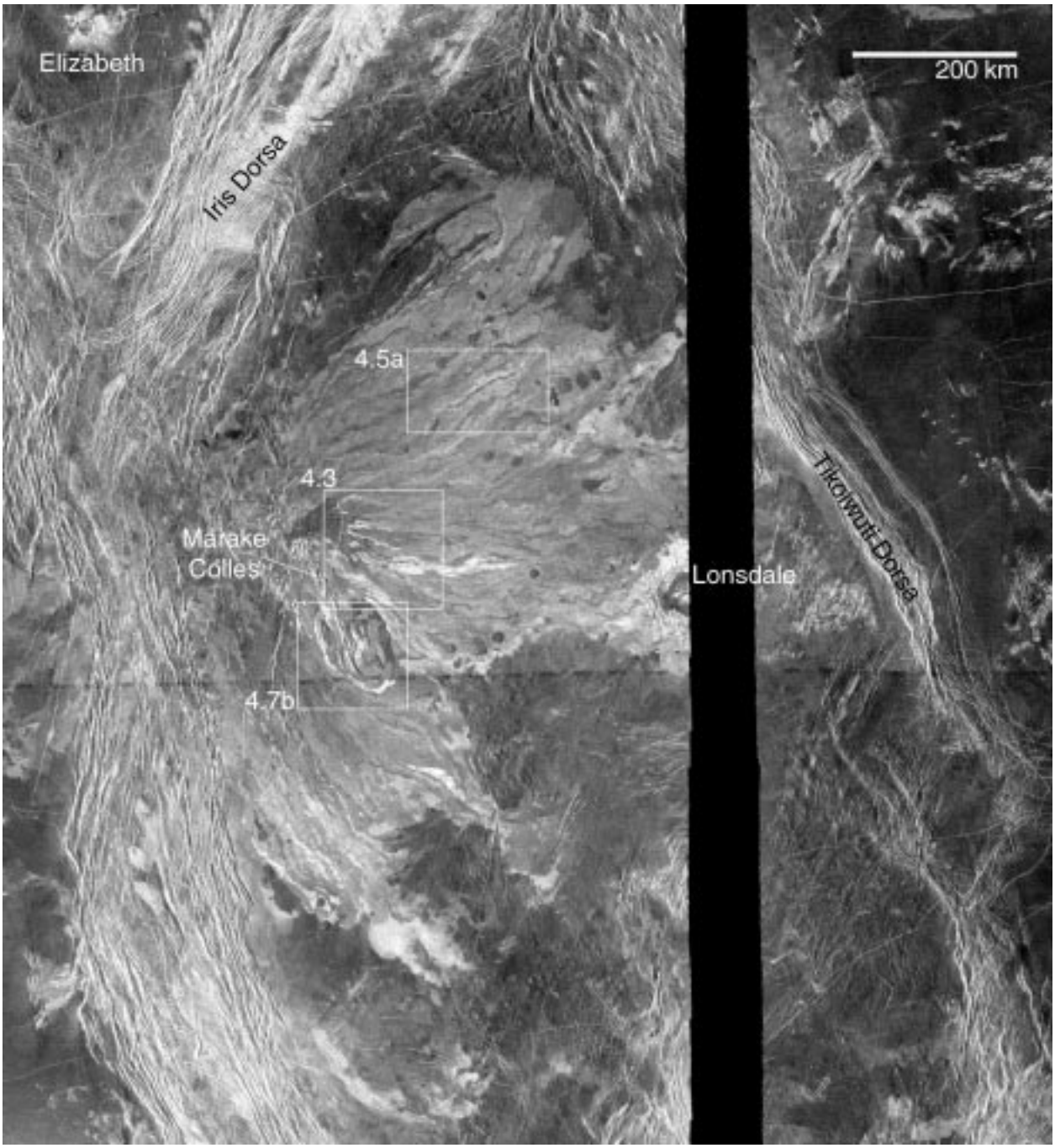
Elizabeth
200 km
Iris Dorsa
4.5a
4.3
Malaka
Colles
Lonsdale
Tikoiwuti Dorsa
4.7b

b

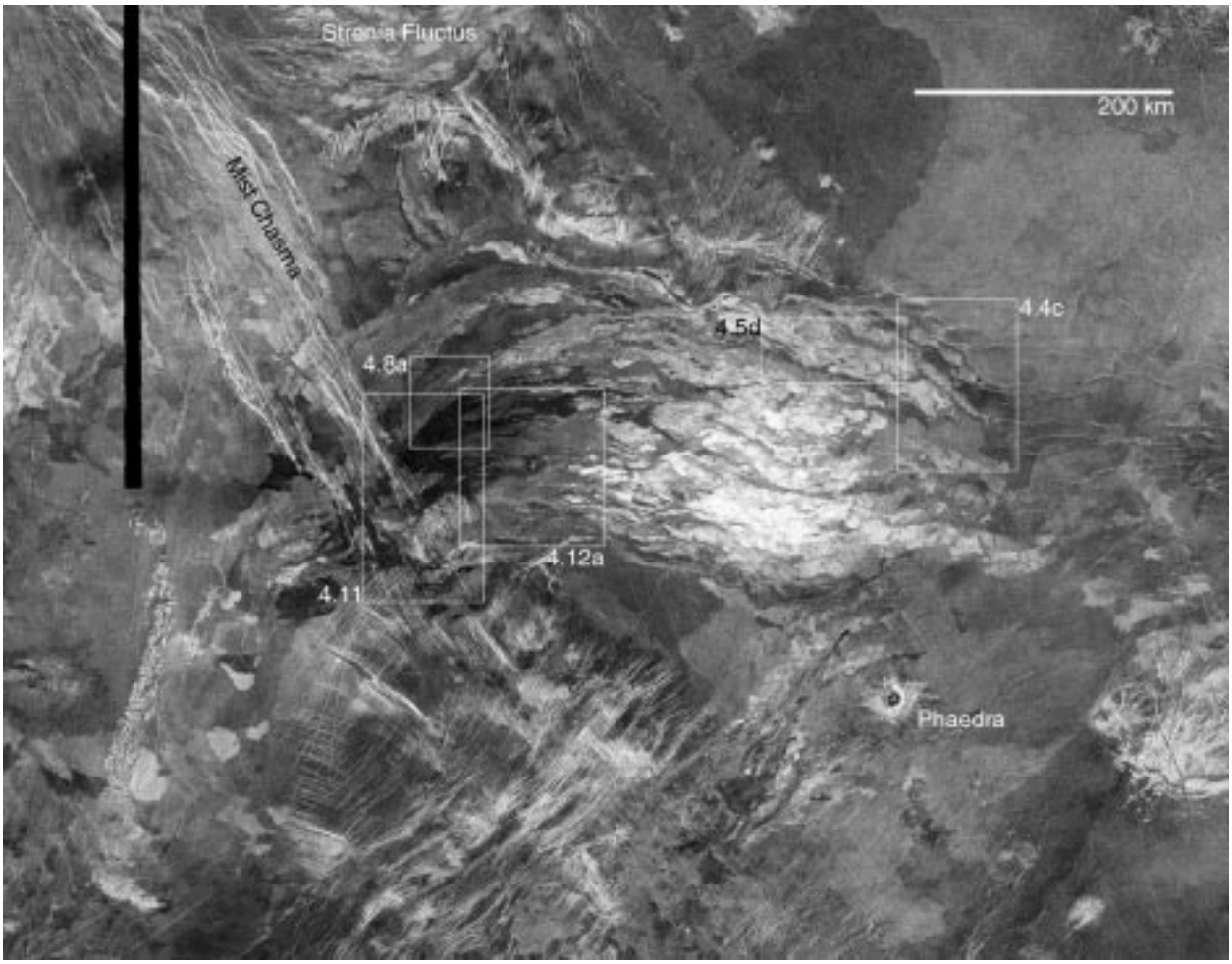

Figure 4.2. (continued)

c

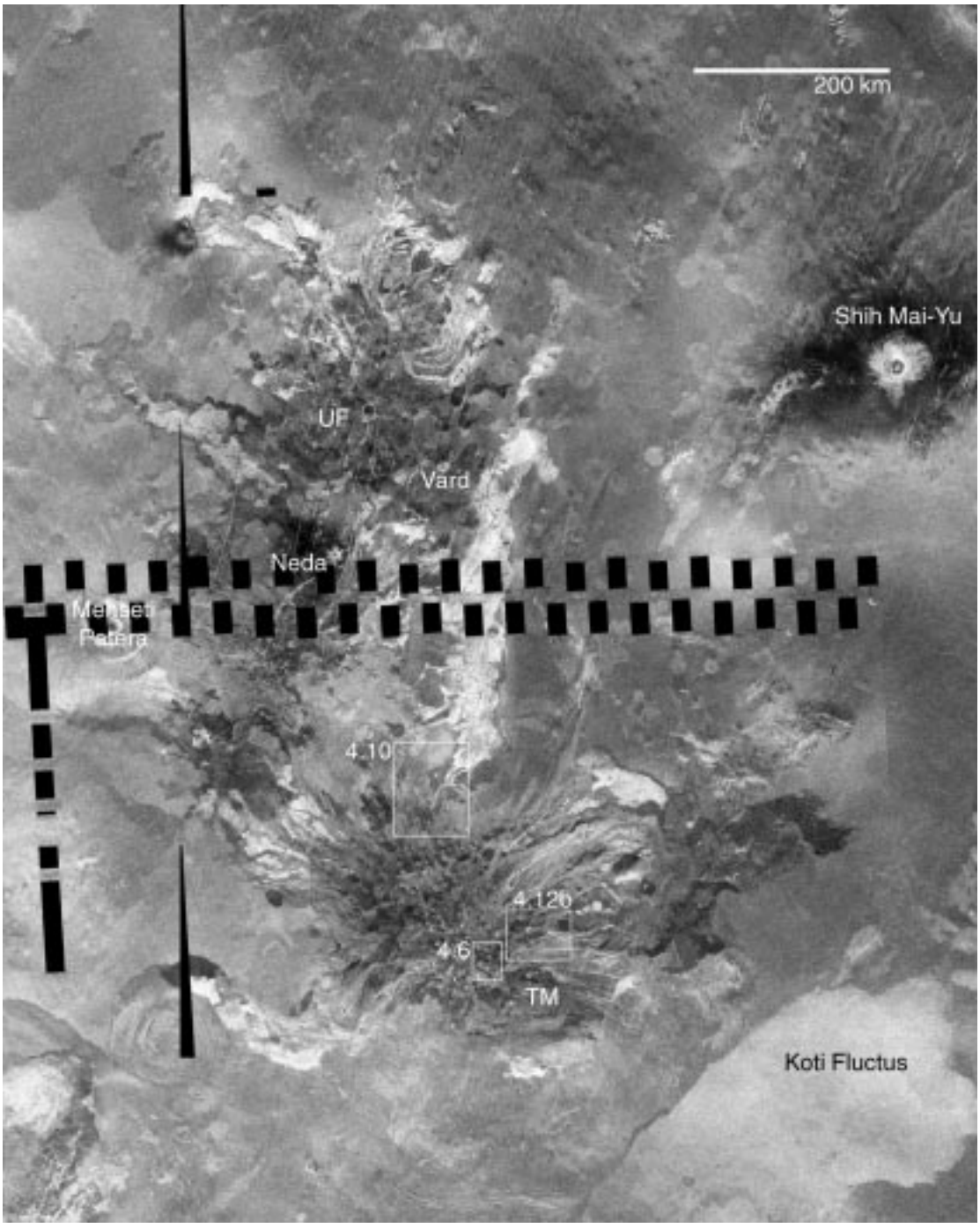

Figure 4.2. (continued)

d

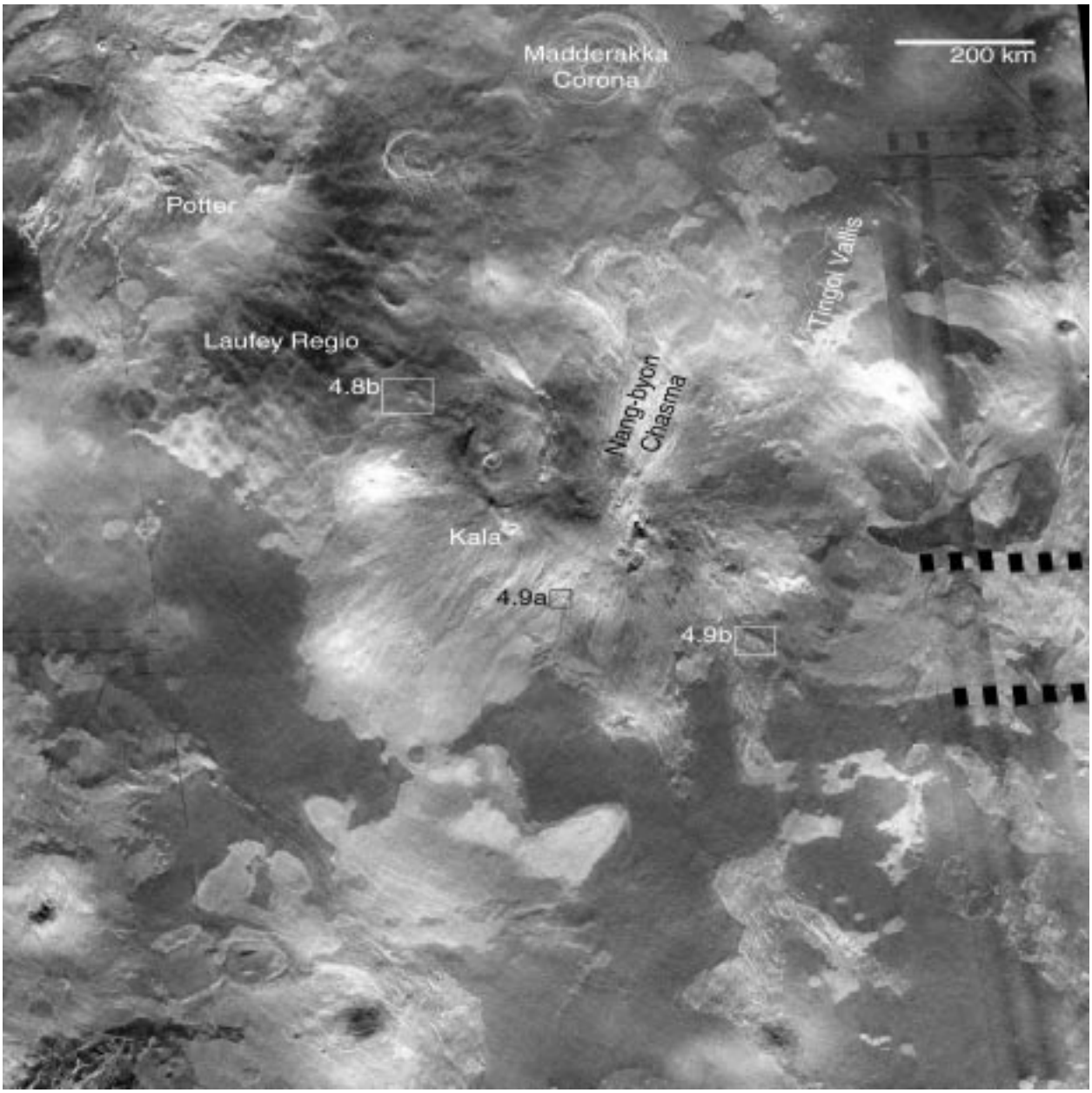

Figure 4.2. (continued)

e

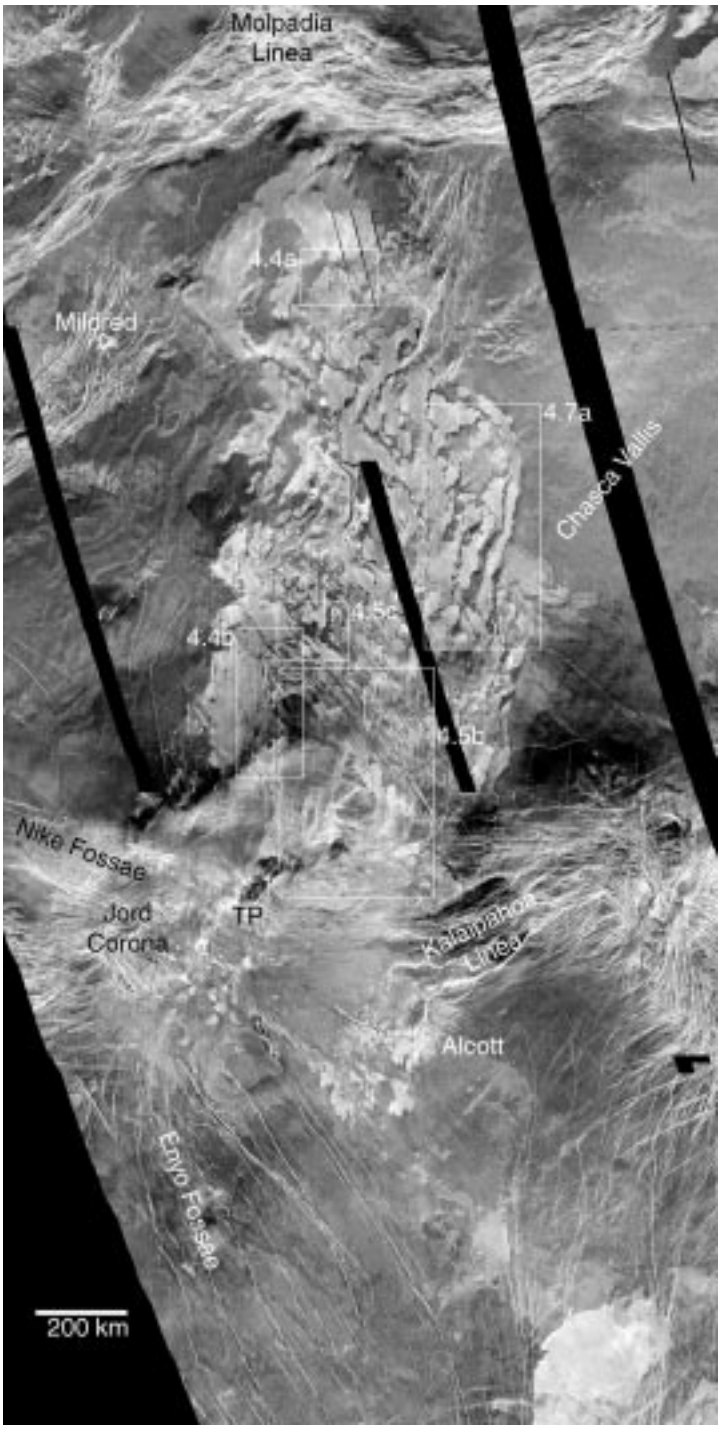

Figure 4.2. (continued)

Flow field base images were produced using the Integrated Software for Imagers and Spectrometers (ISIS, available from the U.S. Geol. Surv., Flagstaff, AZ) to reproject and mosaic Magellan cycle-1 FMAP framelets. Calibration of the radar data follows Ford and Plaut [1993] and Campbell [1995]. To apply the calibration for incidence variations between each successive data row, we fit a 2nd-order polynomial for incidence angle vs. latitude for each flow field. See Appendix B for additional details on Magellan radar calibration.

Synthetic stereo anaglyphs were generated for each flow field to aid interpretation and provide qualitative constraints on topographic effects. The anaglyphs were generated using Magellan SAR data in conjunction with the Global Topography Data Record (GTDR) [Kirk et al., 1992; D. Young, personal communication, refer to: http://www.geology.smu.edu/~tectonics/young/young.html]. The GTDR represents elevation differences of 1 m, although the altimeter footprint is large (≥8 km). Slope information was obtained by taking representative transects along flows and calculating average slopes over a 100 km baseline (except where noted). This baseline length was selected because it is large enough to include a significant number of data points, but small enough to show variations within each flow field.

Observations and mapping of the lava flow fields focused on flow morphologies, flow stratigraphy, and radar backscatter characteristics. Morphologic analysis was conducted to constrain lava emplacement regimes, including whether lava was emplaced in broad lobes or in channel/levee systems and whether individual flows are simple or compound at the scale of the Magellan SAR data, as well as to constrain lava transport styles by identifying morphologic characteristics representative of surface-fed and tube-fed flows. Flow stratigraphy was examined to support morphologic observations, provide further constraints on flow emplacement, and

identify, if present, evolutionary trends in eruptive style. Cross-cutting relationships were also examined between flows and other spatially associated features. Radar backscatter characteristics were analyzed within and between flow units and flow fields and compared to terrestrial flow field radar data.

4.4. Flow Field Descriptions

4.4.1. Turgmam Fluctus

Turgmam Fluctus (58.4-52.7° N, 215.8-225.1° E) extends from Iris to Tikoiwuti Dorsa (Figure 4.2a), covering ~140,000 km^2 of the region between Vinmara and Ganiki Planitiae (to the west) and Virilis Tesserae (to the east). Mapping completed as part of the current analysis differs somewhat from the recently published 1:5M geologic map of the Pandrosos Dorsa Quadrangle [Rosenberg and McGill, 2001]. Specifically, two radar-dark outcrops within the flow field that were mapped as smooth local plains material (ps) are included herein as part of the flow field, and the flow field margin is different in a few locations, although the differences in mapping do not significantly affect interpretations of flow field emplacement. The flow field was imaged at 28.7-31.4° incidence and displays backscatter coefficients ranging from –1.5 to –20.9 dB. Turgmam Fluctus superposes relatively radar-dark plains that exhibit numerous small volcanic constructs, fractures, and ridges. Rosenberg and McGill [2001] indicate that Turgmam Fluctus superposes their radar-dark regional plains material (prc), densely lineated material (ld), and linear belt material (bl) units. The plains deformation that produced ridges in the region primarily occurred before emplacement of the flow field; ridges are breached by lava flows and the flow field lacks features associated with shortening. Fractures are typically buried by the

flows, although some fractures cross-cut the uppermost surface of the flow field. The flow field emanates from the fracture system, the most recent volcanic activity having produced radar-dark flows along an 8 km portion (centered at ~56.0° N, 217.8° E) of a NNW-SSE trending fissure set. The flow field exhibits shallow slopes (<0.15°) and was emplaced through a series of episodes that produced multiple overlapping arms, resulting in a digitate fan morphology.

Turgmam Fluctus is spatially associated with Marake Colles (located SSE of the most recently active fissure vents), which is made up of linear ridge segments (probably genetically related to Iris Dorsa and subsequently modified by Turgmam flows) adjacent to a cluster of small shields and domes (1-5 km diameter). Similar small volcanic constructs are found throughout the flow field. Turgmam Fluctus is superposed by Lonsdale crater (44 km diameter) and is located near Elizabeth crater (10.5 km diameter).

4.4.2. Zipaltonal Fluctus

Emanating from Mist Chasma, Zipaltonal Fluctus (39.2-34.9° N, 247.2-254.1° E) covers almost 80,000 km^2 of eastern Kawelu Planitia (Figure 4.2b). The flow field was imaged at 38.2-40.2° incidence and displays backscatter coefficients ranging from –0.2 to –24.4 dB. Zimbelman [2000] mapped Zipaltonal Fluctus as having been emplaced on older lava flows as well as radar-dark to intermediate plains (including lineated plains), and embaying tessera along its western margin. The most recent eruptive vents are located along a 100 km portion of the Mist Chasma fissure system. The flow field exhibits shallow slopes (<0.10°) and displays a digitate subparallel morphology. Although radar brightness is variable throughout the flow field, the proximal area primarily displays relatively radar-dark flows, the medial region contains

relatively radar-bright flows, and the distal portion exhibits flows of intermediate radar brightness.

An intermediate-size shield or dome (37.2° N, 250.1° E) within the medial portion of the flow field appears to be partially buried by Zipaltonal flows. The edifice is ~20 km in diameter and displays a radial surface texture with central radial fractures. A few tens of isolated small shields are also associated with the flow field. These shields are typically 1.5-2.5 km diameter and up to 6.5 km diameter. Other nearby features include Strenia Fluctus (which also emanates from Mist Chasma) to the north [Zimbelman, 2000], Phaedra crater (16 km diameter) to the south, and Junkgowa Corona (~280 km diameter) to the east of Zipaltonal Fluctus. The surface of the flow field's distal-most portion is cross-cut by radial fractures associated with Junkgowa Corona, and also appears to have been uplifted in conjunction with corona formation.

4.4.3. Tuli Mons/Uilata Fluctus Flow Complex

Within Guinevere Planitia, a large volcanic flow complex covering ~350,000 km^2 developed through coalescence of Uilata Fluctus, flows from Tuli Mons, and other localized sources within 20.5-11.8° N, 311.4-318.6° E (Figure 4.2c). The flow field was imaged at 44.9-46.0° incidence and displays radar backscatter coefficients of –4.6 to –28.6 dB. Crown et al. [1994, 2002b] mapped the flow complex as having been emplaced on mottled, lineated plains of intermediate radar backscatter, radar-dark plains with wrinkle ridges, and lava flows emanating from Madderakka Corona. Along its western margin, the flow complex may be interfingered with flows from Mehseti Patera. Tuli Mons displays ~600 m of relief and a field of low, small edifices at its summit [Crown et al., 1994]. Slopes on the Tuli Mons edifice are shallow (<0.35°). A cluster of small edifices (shields, cones, and/or domes) is also associated with the

Uilata Fluctus source region, located on a low shield-shaped construct displaying less relief and shallower slopes (<0.30°) than Tuli Mons. Other small edifices are located within the volcanic complex. The flow complex is composed of coalesced digitate aprons. Lobes are distributed radially from their sources on the two constructs, reflecting the topography of the edifices. Peripheral to both edifices' flanks, lobes are generally oriented toward the north, reflecting the regional slopes (~0.035° over ~900 km baseline) from Laufey Regio northward into Guinevere Planitia.

Vard (6 km diameter) and Neda (8 km diameter) craters are superposed on the northern portion of the complex. Near the flow complex are Madderakka Corona to the south from which Koti Fluctus emanates, Atanua Mons to the southwest, Hulda Corona to the west, and Shih Mai-Yu crater (22 km diameter) to the east.

4.4.4. Var Mons Volcanic Center

Var Mons, a large volcanic center, is located between Guinevere, Undine, and Navka Planitiae at 1.2° N, 316.2° E (Figure 4.2d). The volcano, which exhibits 1.7 km of relief, displays a complex summit region with at least three distinct eruptive centers and flows that embay its prominent rift zone, Nang-byon Chasma [Crown et al., 1994; Brian et al., 1999]. The flow field (8.1° N-5.7° S, 309.2-320.6° E) covers ~820,000 km^2, although much of its margin is poorly defined. The flow field was imaged at 43.9-46.1° incidence and displays radar backscatter coefficients of –3.5 to –27.5 dB. The flow field superposes mottled, lineated plains of intermediate radar backscatter, radar-dark plains with wrinkle ridges, and lava flows from Madderakka Corona [Crown et al., 2002b]. The Laufey Regio dark halo material, which is associated with Potter crater (46.9 km diameter), appears to superpose portions of the flow field,

although some Var Mons lava flows superpose the halo material. Lava flows extend from the summit region of Var Mons, and particularly from a vent located 250 km NE of the highest point on the volcano. The flow field displays an overall digitate apron morphology, although of the five flow fields examined it is the closest to the transitional flow field morphology of Lancaster et al. [1995]. Maximum slopes within the complex are ~2.35° (the steepest measured in this study), although slopes in the apron are typically <0.10°. Despite having a wide range of radar backscatter, the Var Mons flow field displays the least well defined lobes of the flow fields examined. Kala crater (17.4 km diameter) is superposed on the flank of Var Mons.

4.4.5. Mylitta Fluctus

Located in southern Lavinia Planitia, Mylitta Fluctus (49.1-61.8° S, 347.8-359.3° E) covers ~390,000 km^2 (Figure 4.2e). The flow field was imaged at 20.4-23.6° incidence and displays radar backscatter coefficients of –2.0 to –17.8 dB. Fracturing and deformation in the region formed Nike and Enyo Fossae and Kalaipahoa Linea. The flow field superposes plains units of Lavinia Planitia and the uppermost flow surface was emplaced after the regional deformation, as fractures do not cross-cut the flow field. The flow field extends up to 960 km from Tarbell Patera (58° S, 351° E; 24.5×40.3 km wide), which is located on an ~395×430 km diameter shield. This edifice is adjacent to, and overlies a portion of, Jord Corona, with Mylitta flows resurfacing fractures on the corona. Maximum slopes on the shield are <1.00°, and slopes in the medial and distal portions of the flow field are <0.10°.

Previous mapping characterized the general flow field setting and characteristics [Roberts et al., 1992]. The primary source vent is Tarbell Patera, and secondary vents may be inferred from the regional sketch map and flow maps [Figure 3 and Plate 1 from Roberts et al., 1992].

Flow lobes were described as typically radar-bright with uniform surface textures and lobate margins. Central channels were identified and often associated with levees and overflows. Six smaller flow fields were mapped within Mylitta Fluctus, each of which was interpreted to represent a major eruptive event in Mylitta's history based on radar brightness and morphology. Lancaster et al. [1995] classified Mylitta as a digitate subparallel flow field.

The current analysis (which includes flows not previously mapped as part of the flow field) shows that flow lobes within Mylitta Fluctus display a wide variety of morphologic and radar backscatter properties. The previous division of the flow field into smaller discrete flow fields, based on C1-MIDRs (compressed-once mosaiced image data records, resampled to 225 m/pixel), has been reevaluated in the current FMAP-scale analysis. The current study indicates that Mylitta Fluctus is composed of an abundance of individual flow lobes forming an extensive flow field.

Two clusters of volcanic shields are spatially associated with Mylitta Fluctus: one is located toward the northern end of the flow field near Chasca Vallis and associated with lineaments, and the other cluster is located on Jord Corona and extends SE along the general trend of the fossae. Alcott crater (~65 km diameter) is located along the eastern margin of the edifice. Ejecta from Alcott is superposed on older Mylitta flows and the crater is flooded by subsequent flows.

4.5. Lava Flow Field Characteristics

Interpretations of lava flow emplacement processes for the five flow fields examined are based on current knowledge of terrestrial analogs and are inherently limited by the difficulty in

distinguishing surface texture changes along or across a flow from superposition of units with different surface textures. Additionally, although lava flow surfaces have been successfully modeled using scattering theory, small-scale surface morphology cannot be uniquely determined based on radar data [Campbell et al., 1993]. Magellan radar data interpretation is further complicated because each pixel represents averaged surface roughness over large (>5500 m^2) areas. Although morphologies observed in the Magellan SAR data are similar to terrestrial flow morphologies, the Venusian features are often orders of magnitude larger.

4.5.1. General Flow Field Characteristics

All five study areas display a digitate flow field morphology (Table 4.1). Two of the flow fields emanate from fissure systems and three were emplaced from centralized vents. Fissures tend to produce elongated flow fields and centralized sources typically generate apron morphologies, due to topographic effects, but vent geometry does not appear to be related to emplacement processes occurring within the flow fields. Each flow field is fairly well defined over most of its extent, though all display some diffuse margins. Flow fields range from 475 to 1450 km long and 200 to 900 km wide. Each flow field displays radar-bright and -dark lobes as well as radar-dark lava channels, although the entire range of morphologic variation is not displayed at any individual flow complex. Proximal regions tend to show the most variation of radar brightness within each flow field, as well as the greatest concentration of radar-dark flows (Figures 4.2-4.3). The range of radar backscatter observed is interpreted to result from the emplacement of near-vent flows over a wider range of conditions than flows in the medial and distal portions of the flow fields. However, modification of medial and distal flow surfaces

Table 4.1. Summary information for flow field study areas

flow field	flow field location	flow field size (km^2)	radar backscatter range (dB)	incidence angle (°)	vent characteristics	flow field morphology[1]
Turgmam Fluctus	58.4-52.7° N, 215.8-225.1° E	140,000	–1.5 to –20.9	28.7-31.4	fissure system	digitate fan
Zipaltonal Fluctus	39.2-34.9° N, 247.2-254.1° E	80,000	–0.2 to –24.4	38.2-40.2	fissure system	digitate subparallel
Tuli Mons/Uilata Fluctus	20.5-11.8° N, 311.4-318.6° E	350,000	–4.6 to –28.6	44.9-46.0	multiple central vents	coalesced digitate aprons
Var Mons	8.1° N-5.7° S, 309.2-320.6° E	820,000	–3.5 to –27.5	43.9-46.1	multiple central vents	digitate apron
Mylitta Fluctus	49.1-61.8° S, 347.8-359.3° E	390,000	–2.0 to –17.8	20.4-23.6	primary central vent	digitate subparallel

[1]classification scheme of Lancaster et al. [1995]

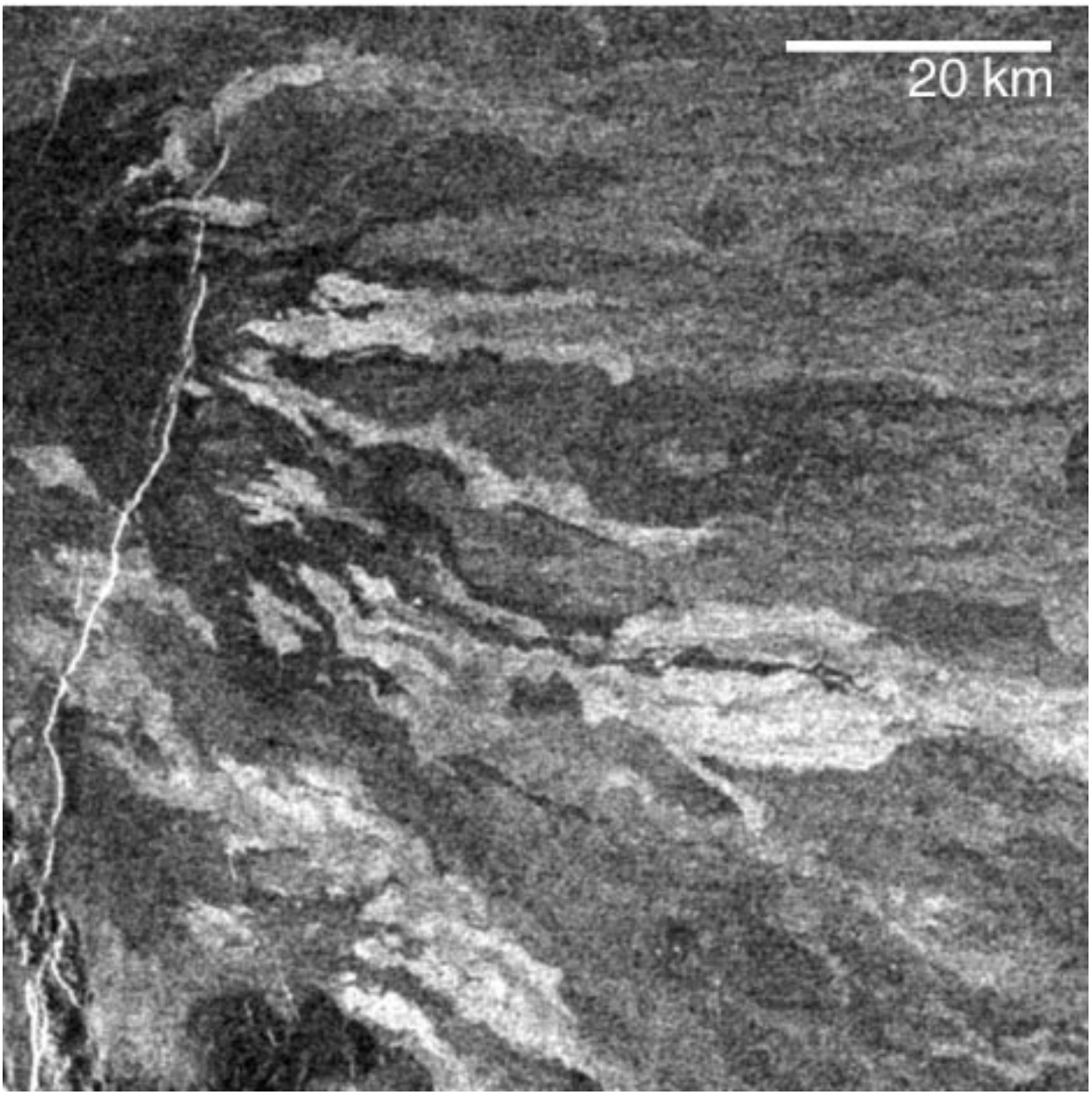

Figure 4.3. The most recent flows emanating from the vent system at Turgmam Fluctus. This area shows the greatest local diversity of radar brightness and the greatest concentration of radar-dark flows within the flow field. The morphology of the radar-dark lobes is most likely a product of branching and superposition of simple flow lobes.

during the final stages of, or following, emplacement, by processes such as flow inflation and foundering of the surface crust, may preferentially reduce the abundance of dark flows by disrupting smooth surfaces and thus may reduce the range of radar backscatter (see section 4.5.2). Flow fields show a significant difference in radar backscatter between roughest and smoothest flows (~16-24 dB over a 1-4° range of incidence), although the overall backscatter values tend to decrease with increasing incidence angle. No consistent trends in radar backscatter are apparent across a flow field, nor with time (based upon the observed stratigraphy, discussed in sections 4.5.5 and 4.5.6).

4.5.2. Lobate Features

The five flow fields studied display numerous discrete, elongate flow lobes. These lobes are generally radar-bright and have lobate margins (Figure 4.2). Lobe margins typically exhibit similar radar brightness to that of the surface of the whole flow lobe, although this interpretation is somewhat biased because lobe boundaries are generally identified by a contrast in radar brightness at the 75 m/pixel scale. Bright lobes with dark, lobate margins (Figure 4.4a), dark lobes with bright, digitate margins (Figure 4.4b), and dark units with lobate margins are also present in the flow fields.

Some lobes display discrete interior zones of increased radar brightness (Figure 4.4c), which may: 1) indicate post-emplacement modification of portions of the lobe interior, 2) reflect changes in flow conditions during lobe emplacement, 3) represent older flows (kipukas), and/or 4) result from differential mantling. In the first case, broad lobes are interpreted to have been emplaced as relatively smooth flows. After emplacement, the lobe interior becomes rougher due

a

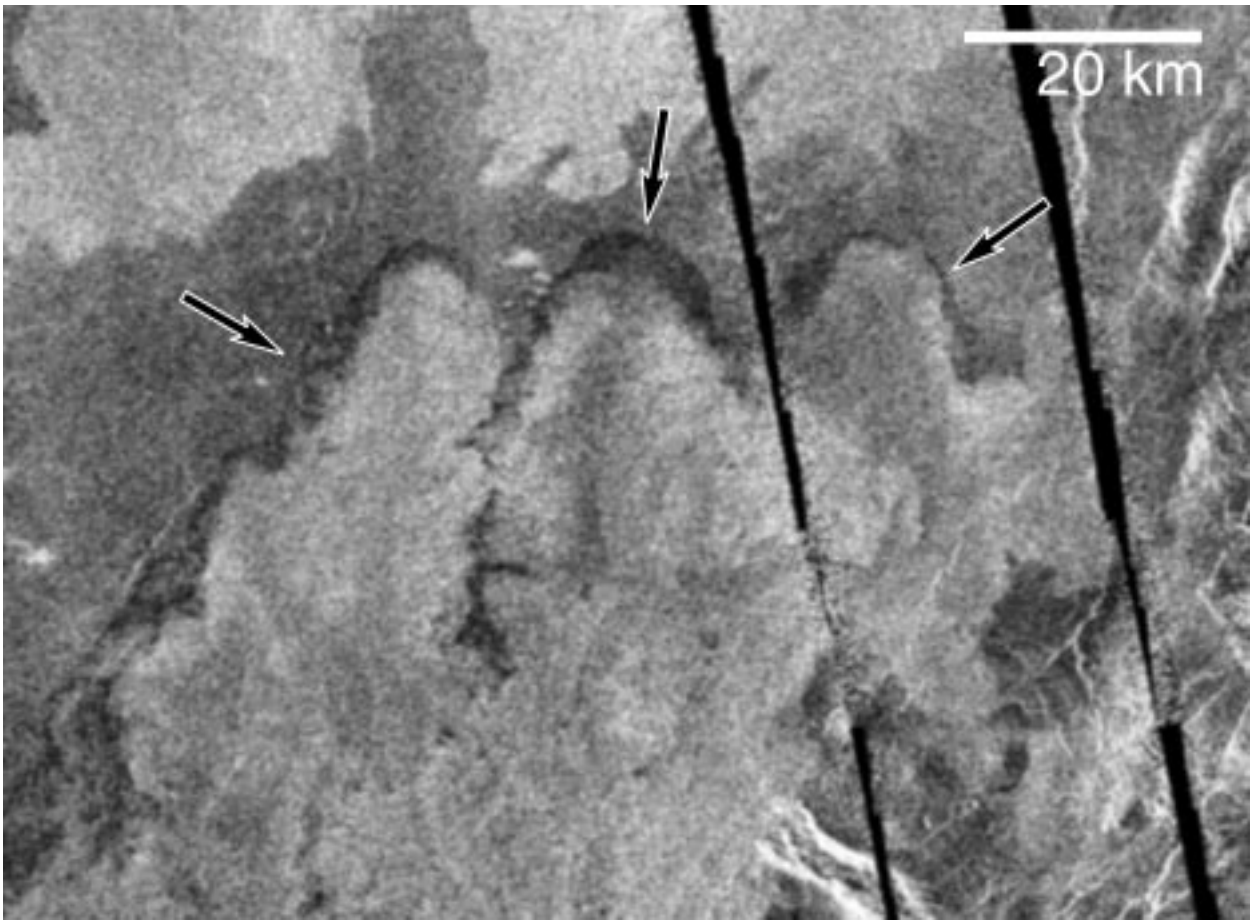

Figure 4.4. Examples of lobe morphologies observed within venusian flow fields. (a) Broad lobes of intermediate radar brightness displaying dark margins (arrows) within Mylitta Fluctus. (b) Radar-dark Mylitta Fluctus lobe displays bright, digitate margins (arrows). Lobe narrows and margins become brighter downflow. (c) Radar-dark lobe within Zipaltonal Fluctus displays interior radar-bright zones (arrows). See text for discussion.

b

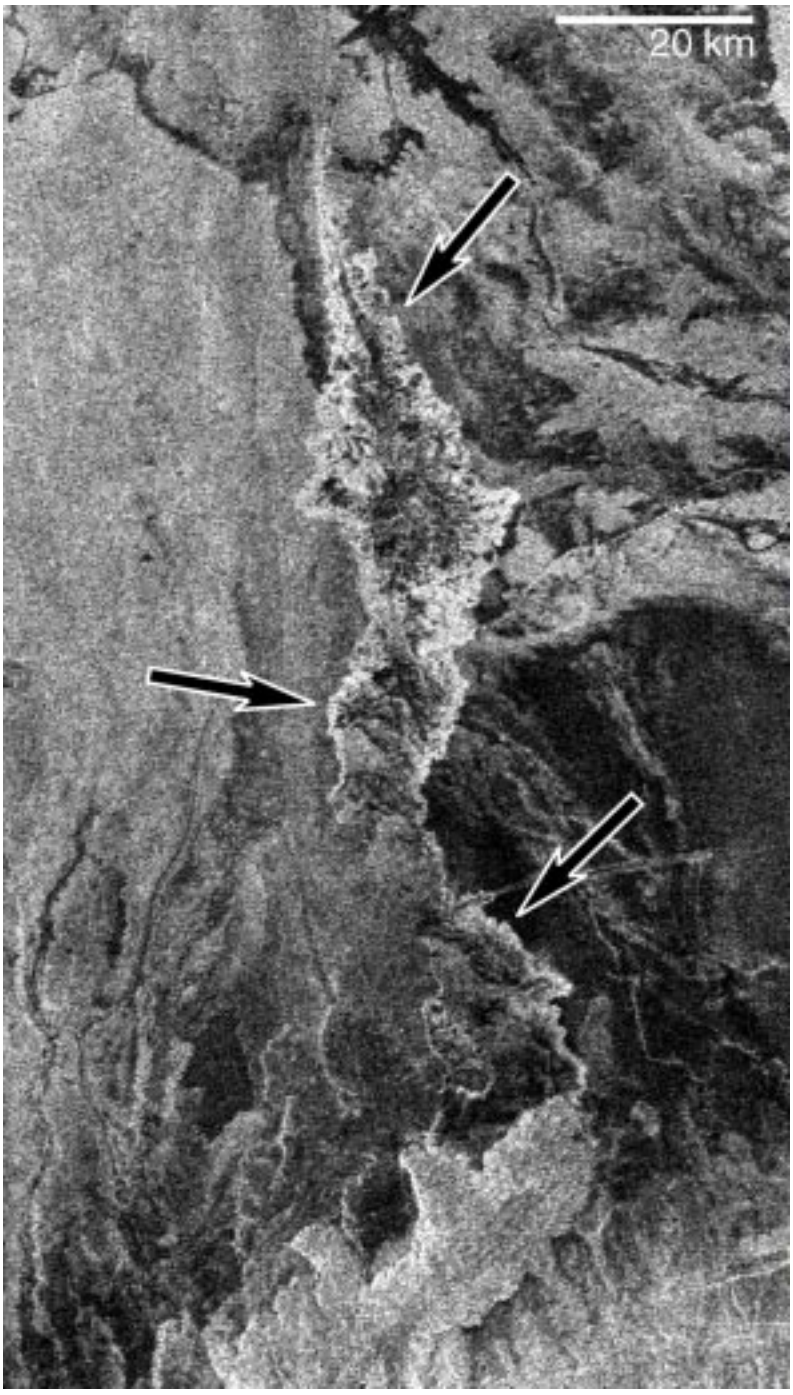

Figure 4.4. (continued)

c

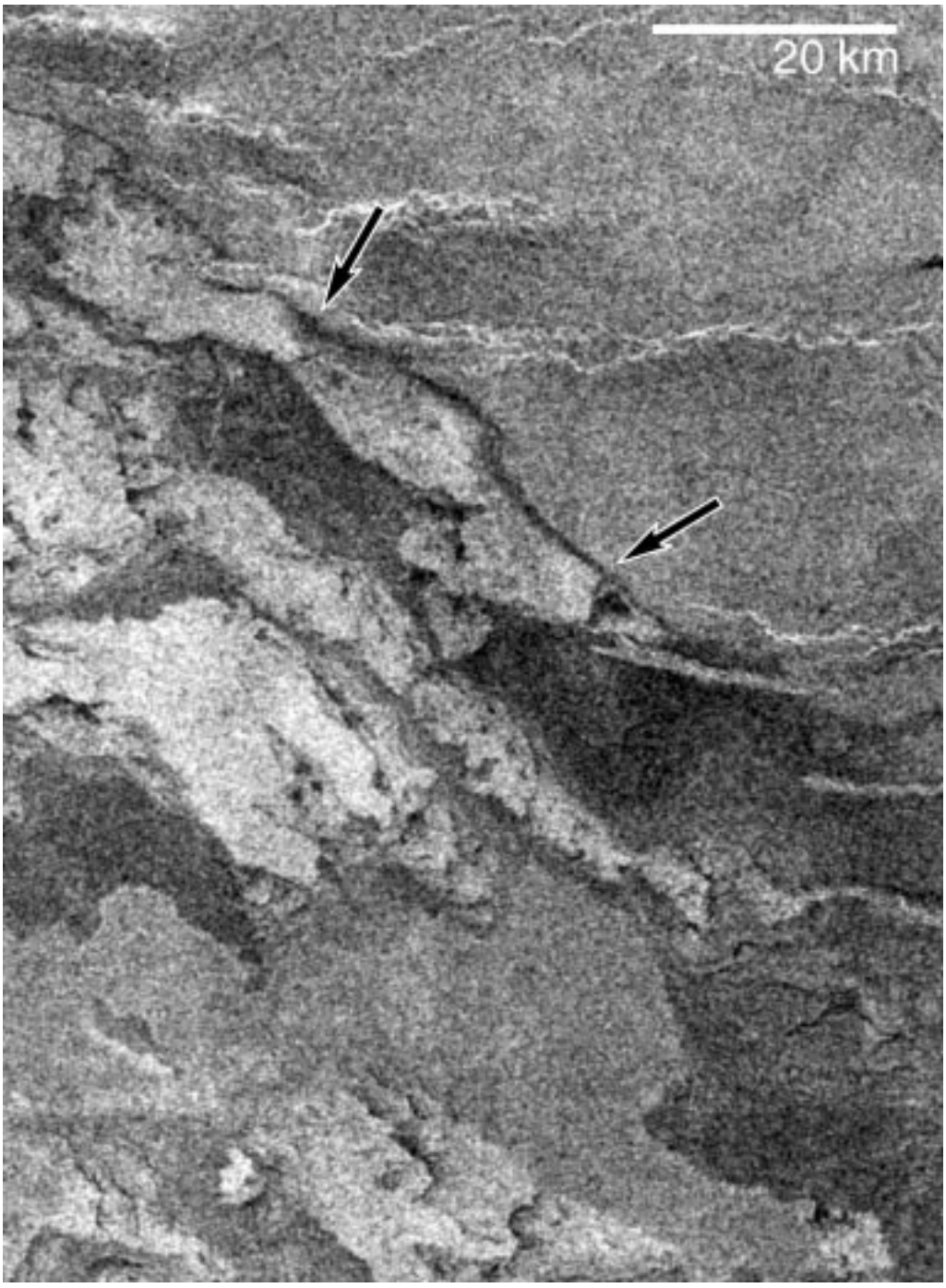

Figure 4.4. (continued)

to processes such as inflation that forms cracks (cm- to dm-scale) [Hon et al., 1994] and/or tumuli (m- to Dm-scale) [Rossi and Gudmundsson, 1996] at sub-pixel scales, or foundering of the surface crust after draining of the lobe interior. In the second case, flow roughness is interpreted to vary as the flow front advances. This may indicate that portions of the surface crust is fractured or deformed during emplacement due to differential flow within the lobe, that smooth-surfaced breakouts are emplaced at flow margins, or that the flow is responding to differences in underlying slope and/or substrate roughness. In the third case, kipukas of underlying radar-bright material are visible within the radar-dark lobe. In the last case, relatively fine-grained material may accumulate in topographic lows within and between flows. Although the last two scenarios may occur within the flow fields, they are not sufficient explanations for most occurrences of this morphology and are not consistent with the observation that the radar-dark portions are fairly common and tend to display relatively uniform margin widths along the flow lobes. Specifically, width of the radar-dark margin is not expected to be uniform along an individual flow if that flow is merely bifurcating around a kipuka, nor is mantling expected to commonly produce uniform widths of radar-dark zones adjacent to flow lobes. Both post-emplacement modification and variations in surface roughness during flow advance (cases 1 and 2) have probably occurred within the flow fields and are consistent with this morphology representing a transition to the bright interior/dark, lobate margin morphology (Figure 4.4a). Dark lobes with discrete radar-bright zones occur predominantly in medial to distal portions of the flow fields, which are relatively flat in comparison with proximal regions. This association with topography further supports the interpretation of flow inflation, which commonly affects terrestrial basalt flows on near-horizontal slopes [e.g., Hon et al., 1994; Rossi and Gudmundsson, 1996].

The length of individual lobes shows no simple relationships with average radar backscatter, backscatter variation within the lobe, nor flow widening and branching. Also, lobes tend to have as great a range of radar backscatter across a flow as along it. Lobe lengths are variable within and between flow fields, with maximum observed lobe lengths reaching 100 km within Turgmam Fluctus, 75 km within Zipaltonal Fluctus, 500 km within the Tuli Mons/Uilata Fluctus complex, 140 km within the Var Mons flow field, and 300 km within Mylitta Fluctus.

4.5.3. Lava Channels

Lava channels are common within the flow fields and normally display relatively radar-dark surfaces and smooth (low sinuosity) margins (Figures 4.5-4.6). Channels generally occur as simple linear to sinuous monofilament conduits, although channels may display distributary morphologies. Typically, channels are up to a few tens of kilometers long and a few kilometers wide. Channels may occur as central features within a lobe (Figures 4.5a,b) or may not be associated with a distinct flow lobe (Figure 4.5c). Zipaltonal Fluctus displays a lava channel system that appears discontinuous (Figure 4.5d). This may be due to lava tube formation, changes in surface roughness along the channel surface, narrowing of the channel beyond the limits of resolution, partial burial by subsequent flows/overflows, and/or the development of independent channels along a similar trend.

Many channels are associated with adjacent radar-bright surfaces, some of which are interpreted to be levees (Figures 4.5c, 4.6). Some ambiguities are present in levee identification, as it is not possible in all cases to distinguish levees that formed synchronously with a channel from preexisting topography affecting the course of a subsequent channel.

a

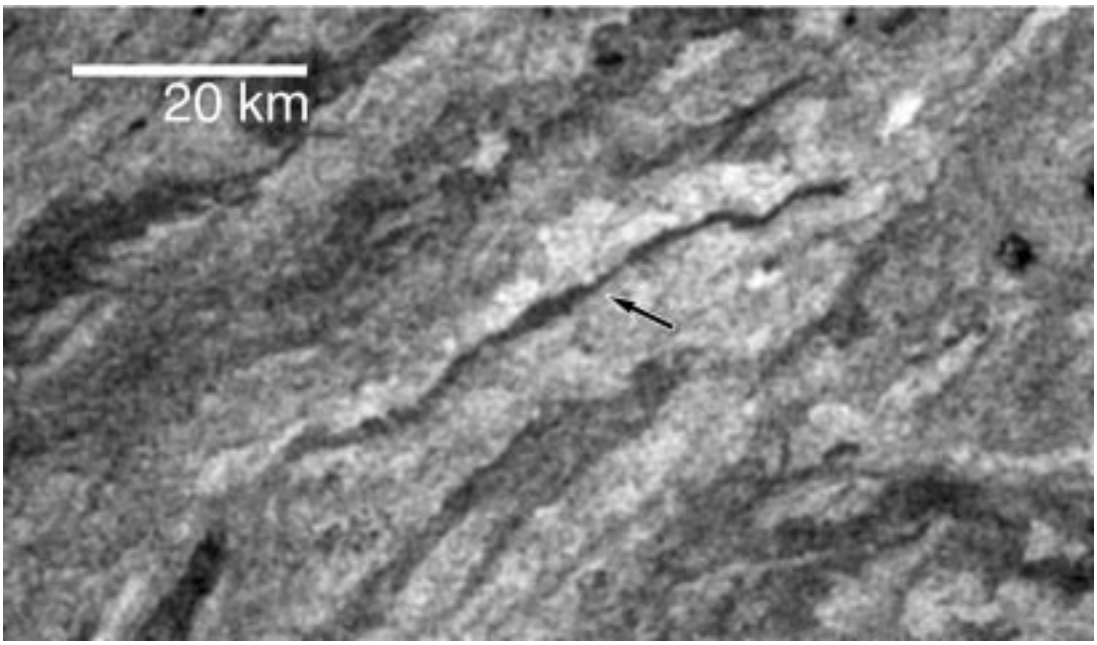

Figure 4.5. Examples of lava channel morphologies. (a) Typical channel (arrow), confined within individual lobe (flow is from SW to NE) within Turgmam Fluctus. (b) Three superposed Mylitta Fluctus lobes (white in sketch map), trending north and northwest across older flows (gray) that trend NE (arrows indicate flow direction). All lobes display central channels (dashed in sketch map). The longest of the lobes becomes broader and more radar-dark toward its distal end, consistent with flow ponding. (c) Radar-dark Mylitta Fluctus channel superposed across multiple lobes. Sudden apparent changes in radar brightness along the channel (arrows) are interpreted to result from partial burial by subsequent flows. Narrow levees are observed along some portions of the channel that have not been resurfaced. (d) Dark, discontinuous Zipaltonal Fluctus channel system (arrows) appears narrow with numerous branches upflow (upper left) and as a single, broad, sinuous channel downflow (lower right); see text for discussion.

b

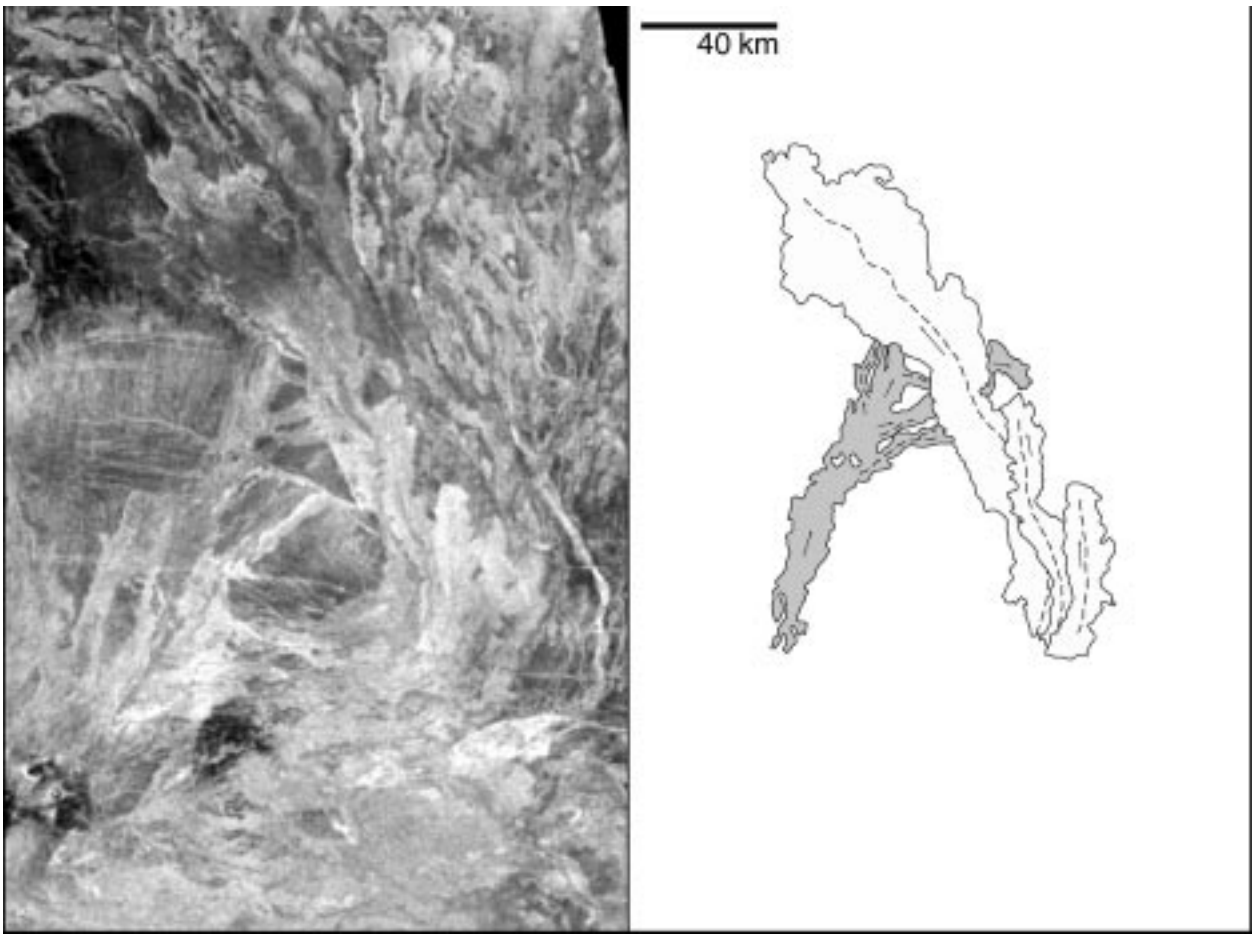

Figure 4.5. (continued)

c

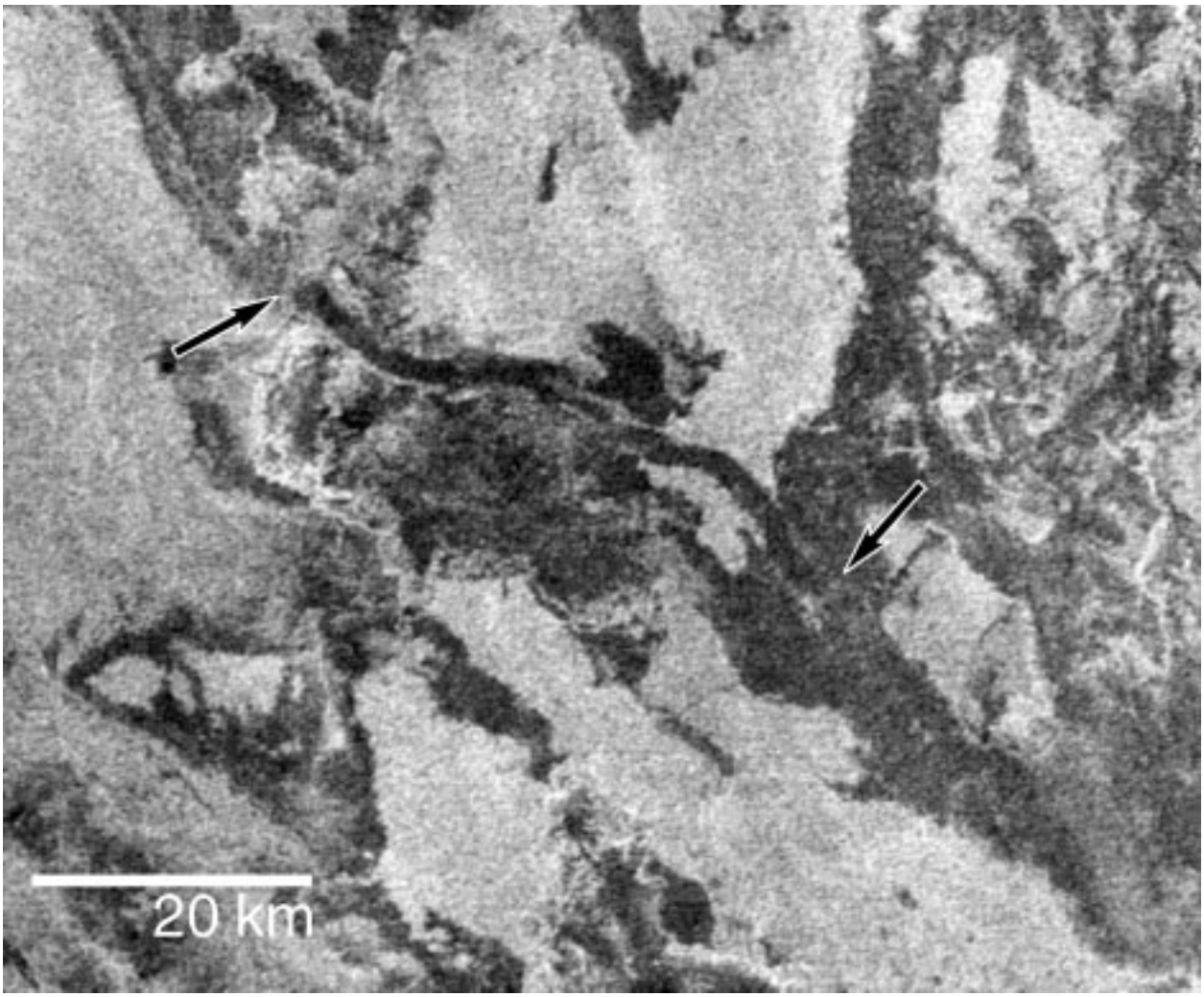

Figure 4.5. (continued)

d

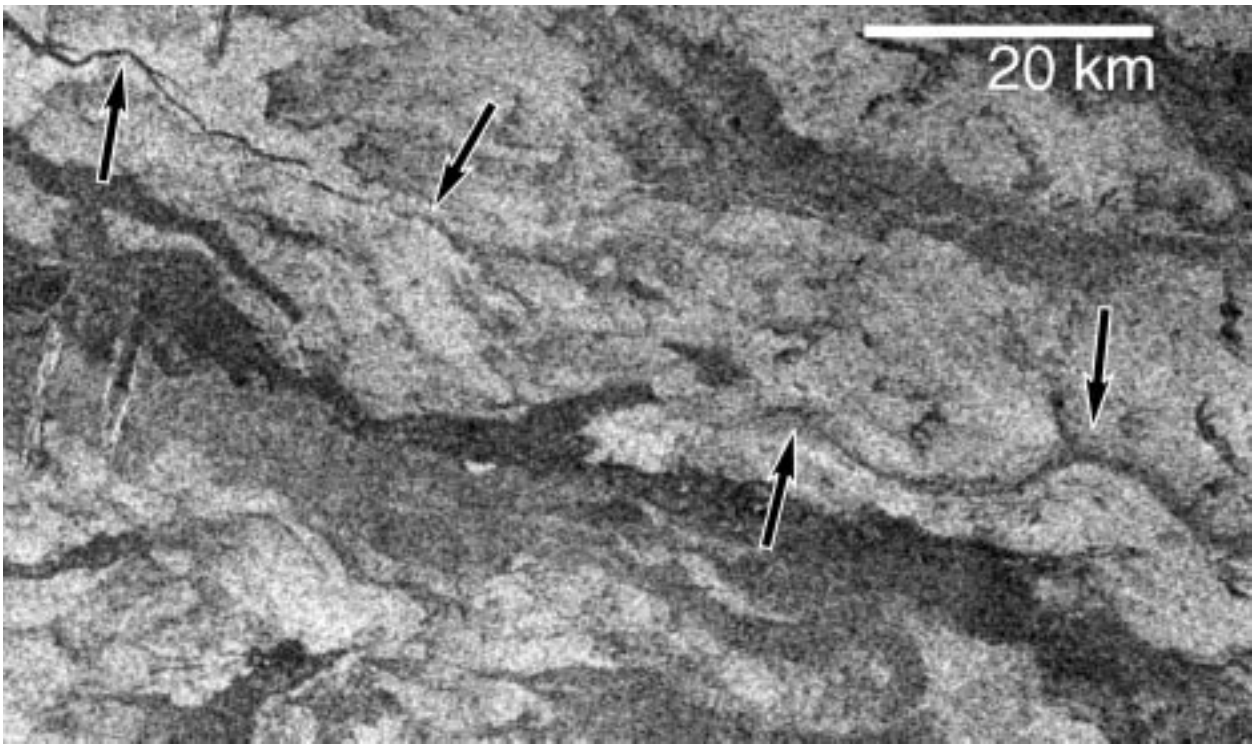

Figure 4.5. (continued)

Figure 4.6. Leveed channels distributed radially about a vent at the summit of Tuli Mons (*V*). A wide variety of small edifice morphologies are displayed within the image.

Some lobes appear to have had a central channel that was later inundated by a relatively smooth-surfaced flow (Figure 4.7). This process may be identified by its tendency to cause the interior lobe margin (bounding the inundated portion) to have a sinuosity that is intermediate to that of channels and typical lobe peripheries. This interpretation is supported by previous analysis of a flow lobe within Mylitta Fluctus that indicated the peripheral margin (see Figure 4.7a) had a higher fractal dimension and greater range of fractal scales than the interior margin [Bruno and Taylor, 1995]. It is not possible in any of the channel inundation examples to determine the length of time between channel formation and flooding. In some examples, it is possible that the inundation occurred as channel overflows while the channel was still active, but after the channel margins had stagnated.

Figure 4.7. (following) Examples of inundated-channel morphologies. (a) Radar-bright Mylitta Fluctus lobe with channel inundated by subsequently emplaced radar-dark lava. Statistical analysis [Bruno and Taylor, 1995] indicates that the interior margins along the flooded channel (arrows labeled *i*) are significantly different than margins along the periphery of the bright lobe (arrows labeled *p*). (b) Radar-dark flow within Turgmam Fluctus is captured by, partially floods, and overflows central channel within bright lobe. Margins of dark unit are more crenulated than upflow and downflow portions of the channel that are not flooded (arrows).

a

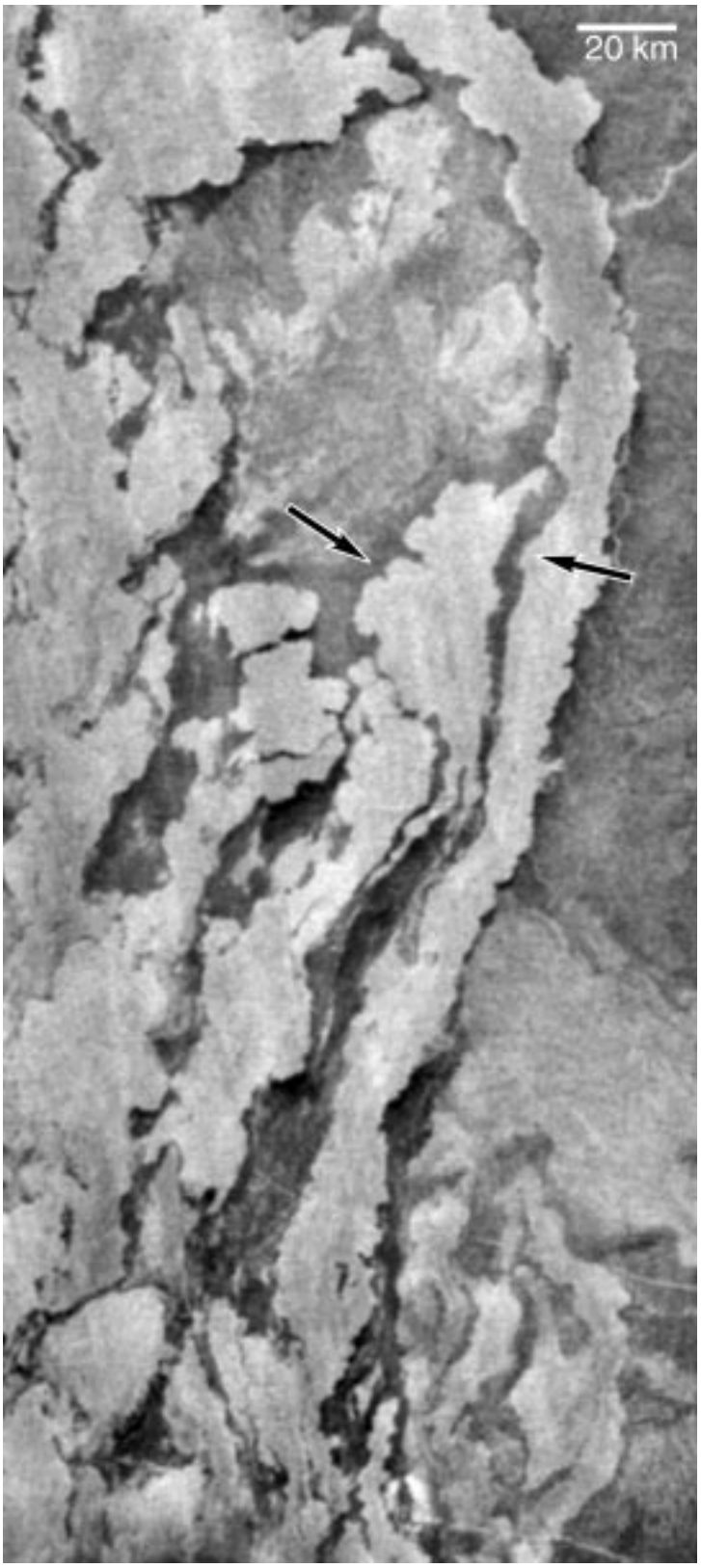

b

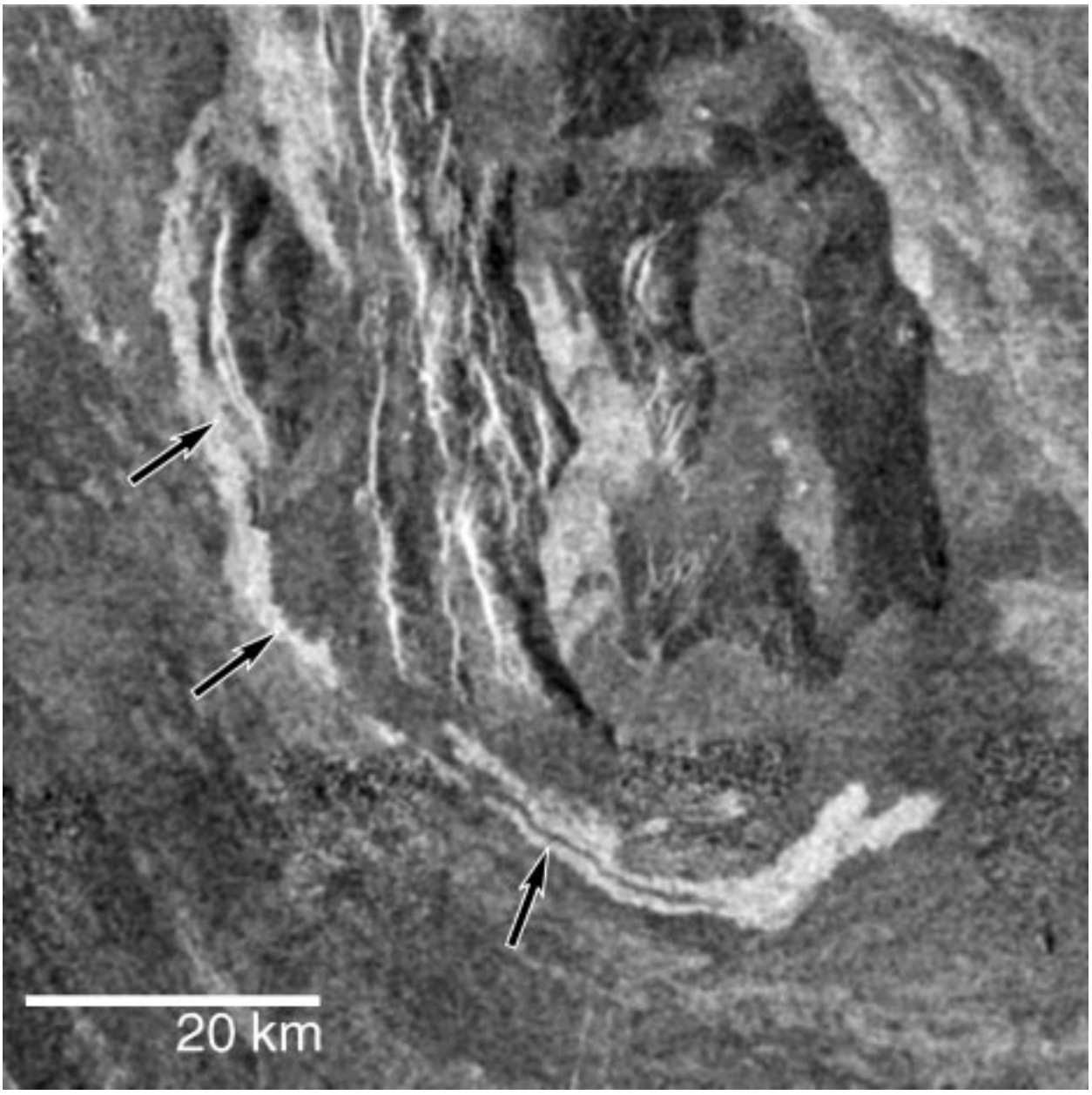

Figure 4.7. (continued)

4.5.4. Flow Branching

The lava flow fields display branching within both lobes and channels. Some lobe branching morphologies observed in Magellan 75 m/pixel data suggest simple flow emplacement, especially near source regions (Figures 4.3, 4.8a). This is consistent with higher extrusion rates expected near the vent, which tend to produce simple flows [Walker, 1972]. Other branching morphologies suggest compound flow emplacement (Figure 4.8b) based on the interpretation that different portions of the lobe flow front were contemporaneously active, though in some cases flows may be responding to topography that is too small to resolve in the Magellan altimetry data. It should be noted that the ability to definitively distinguish between simple and compound flows is limited due to the resolution of the dataset and the nature of radar data. Lobes in many places are divisible into flow units down to the limits of resolution, suggesting that compound flow emplacement may be widespread. This would, in fact, be expected of Venusian flow fields by analogy to terrestrial pahoehoe flows, which are emplaced in a compound manner at the meter-scale (orders of magnitude smaller than resolvable features in the Magellan dataset).

In some locales, distributary flow morphologies appear to be associated with a local source (Figure 4.9). This local source could be a flank vent associated with a minor rift, as is suggested for the example shown in Figure 4.9a, or a lava tube, as interpreted for the example shown in Figure 4.9b. The ability to differentiate between the two types of sources is limited by the resolution of the Magellan SAR data.

a

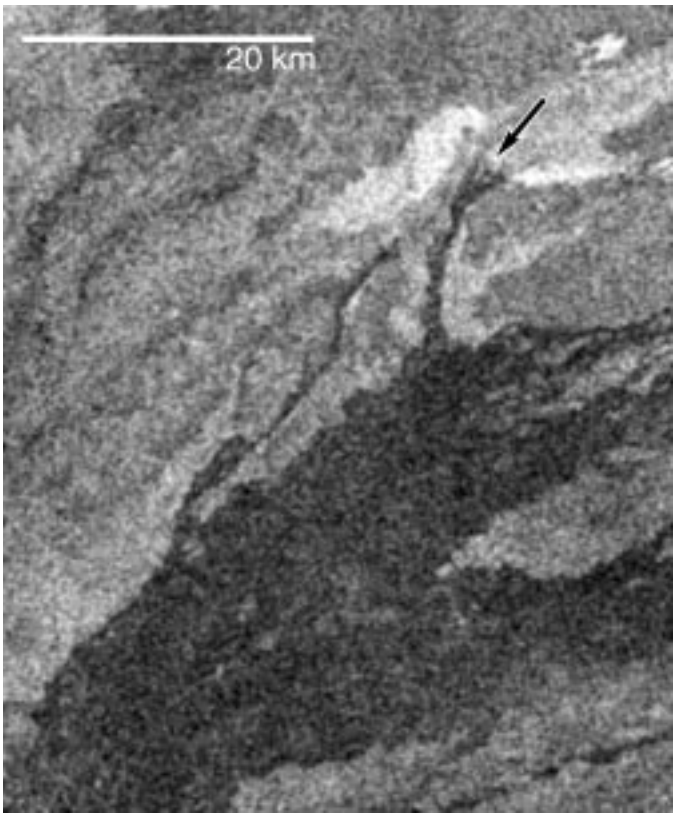

Figure 4.8. Examples of branching morphologies. (a) Radar-dark lava within Zipaltonal Fluctus displays multiple, overlapping lobes and several scales of branching; flow direction is to the N and E. Two narrow lobes that branch northward are presumably channeled by preexisting topography, one of which displays branching near its distal end (arrow) that is suggestive of simple flow emplacement. (b) Flow branching in radar-bright lobe at Var Mons is suggestive of emplacement as a compound flow; flow direction is SE to NW. This branching morphology suggests that different portions of the lobe flow front (arrows) were active rather than advancing as a single simple lobe. Westernmost branch follows margin of an ~39 km diameter dome that both superposes and is partially buried by Var Mons flows.

b

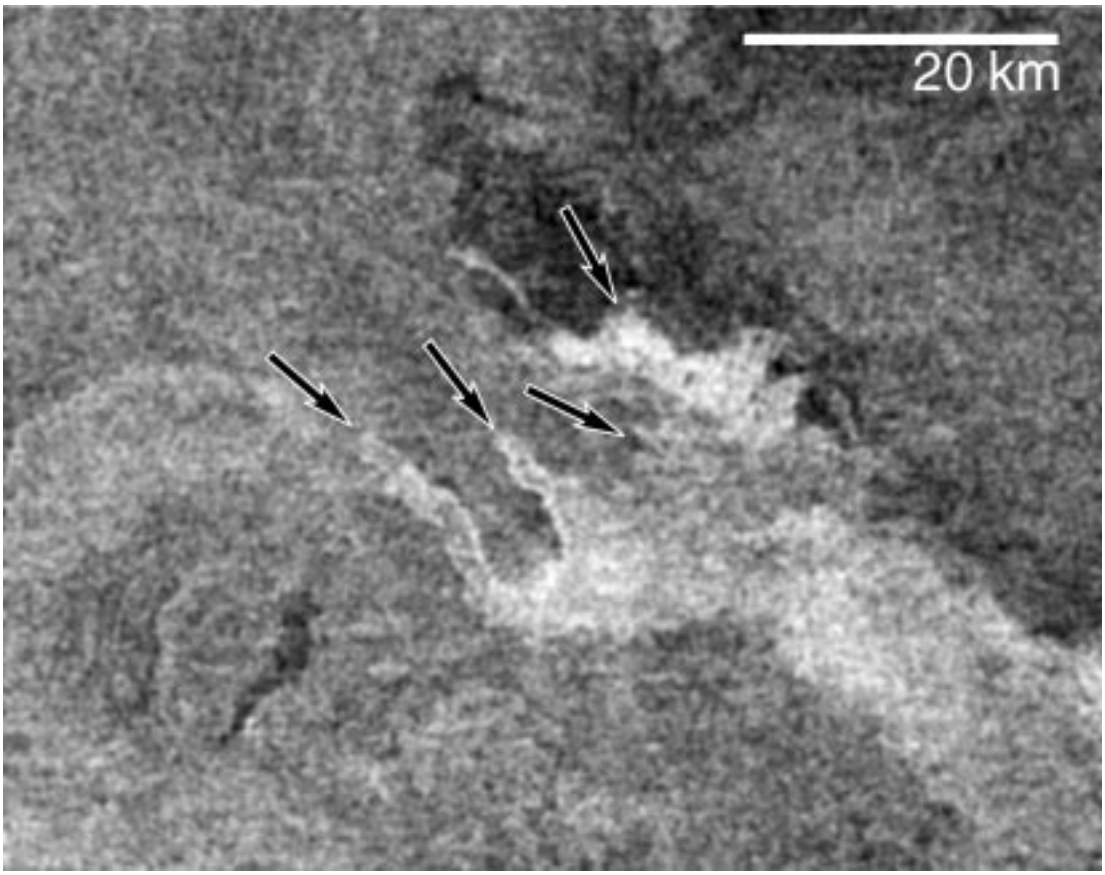

Figure 4.8. (continued)

a

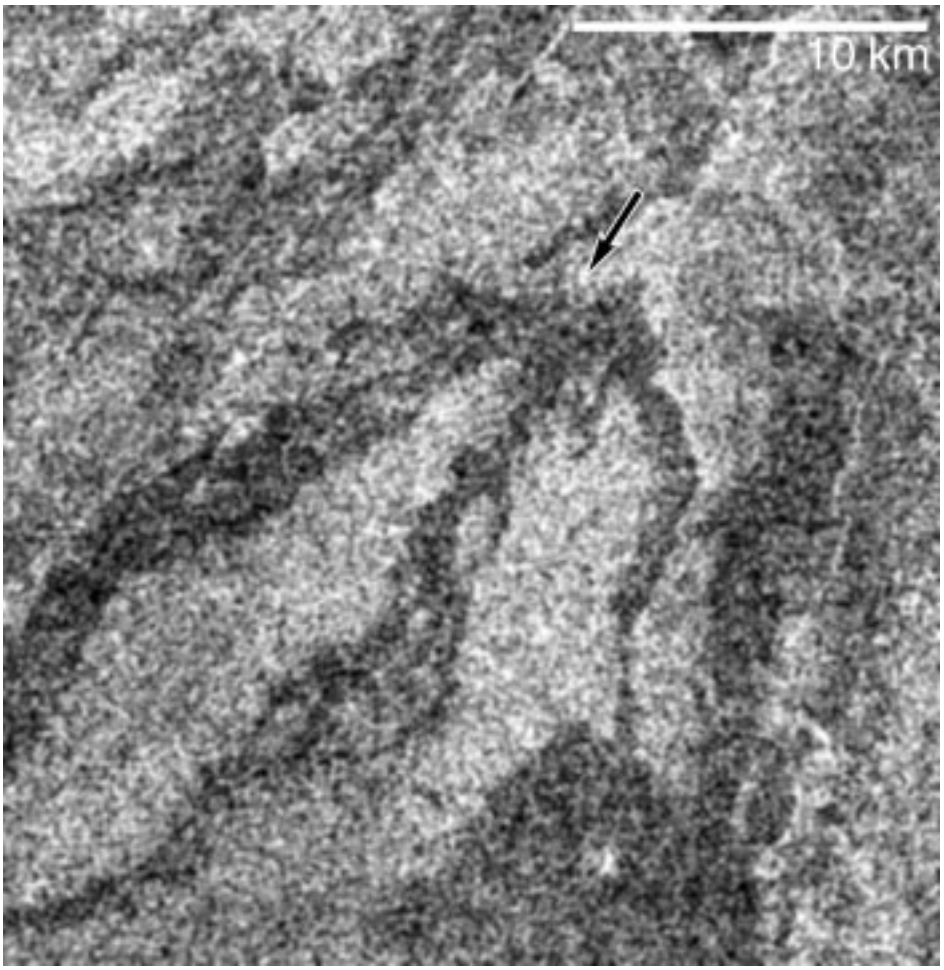

Figure 4.9. Distributary morphologies associated with a local source. (a) Radar-dark distributary at Var Mons displays a source area (indicated by arrows) that is elongated transverse to the downslope direction, suggesting that the vent may be a small flank rift. (b) Distributary morphology of radar-bright flow at Var Mons, suggestive of tube-fed emplacement based on the morphologic similarity to terrestrial lava tube breakouts, the apparent point source, and the lack of evidence for a flank vent (local source indicated by arrow).

b

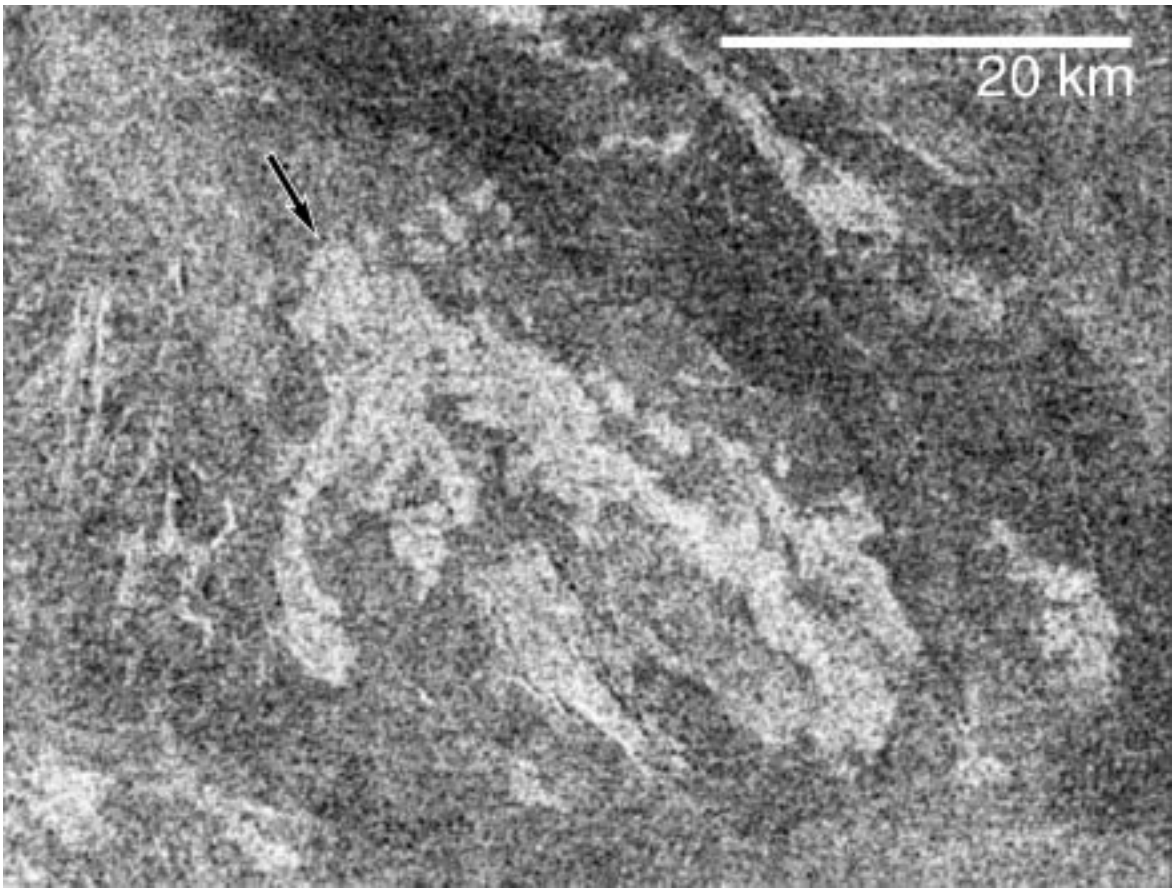

Figure 4.9. (continued)

4.5.5. Flow Stratigraphy and Topographic Effects

Gross topographic effects are evident in the tendency for narrow lobes to be emplaced on relatively steep slopes (proximal region), whereas broader lobes are associated with shallower slopes (distal region) (Figure 4.2). Qualitative assessment of the influence of topography on lava emplacement suggests that flows are responding to a smaller scale of topography than that represented in the Magellan GTDR.

Flow units within the Venusian flow fields commonly display multiple overlapping relationships at a given locality (Figures 4.5b, 4.10), suggesting that flow field emplacement was complex rather than developing during a few discrete events. For radar-bright lobes, the high degree of overlap and the general lack of flow deflection indicate that the scale of topography to which these flows respond is generally larger than the thickness of individual flow units. Radar-dark flows appear to be much more responsive to topography (Figures 4.7, 4.8a) and to the presence structural features (Figure 4.11). These relationships suggest a correlation between radar brightness and flow rheology, specifically that the radar-dark units are less viscous (and less thick), although post-emplacement modification may alter the final surface roughness of flow units (see section 4.5.2 for discussion).

It is expected that radar-facing margins will be brighter than those facing away from the radar if flows have appreciable thickness, although the minimum flow thickness required to produce this effect will vary depending on the margin profile and the imaging geometry. This effect is not observed within any of the flow fields examined, nor are flow thicknesses sufficient to be observed in Magellan altimetry. These observations indicate that individual flow lobes are relatively thin, consistent with previous estimates (e.g. 10-30 m for portions of Mylitta Fluctus

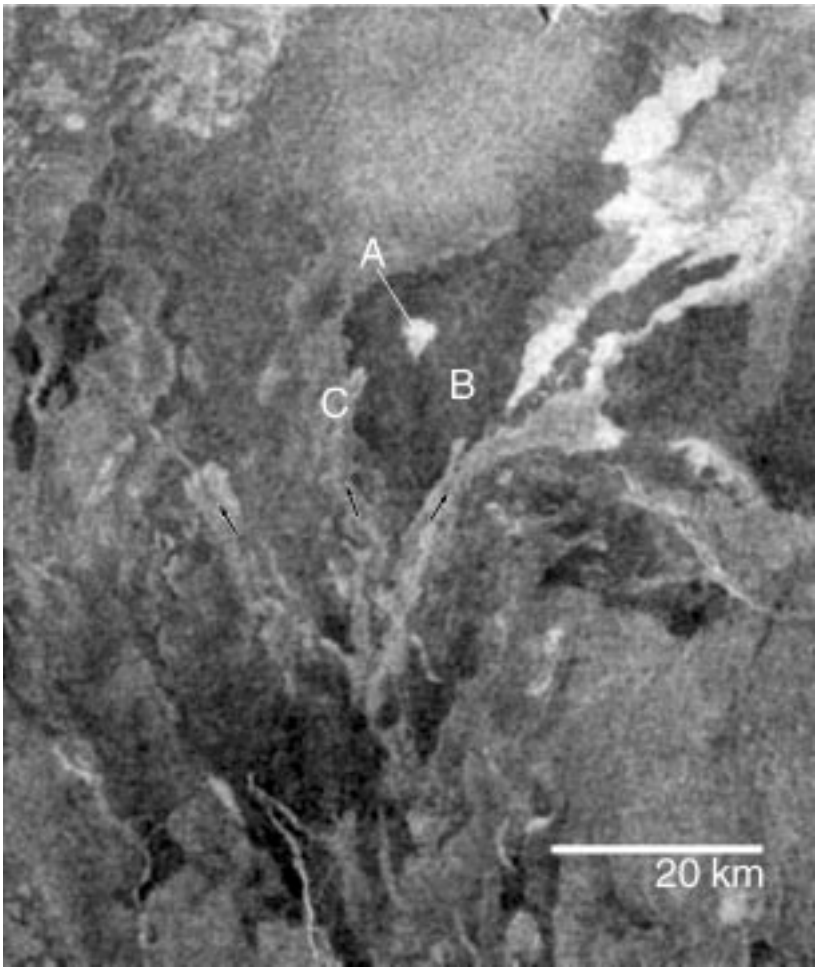

Figure 4.10. Radar-bright kipuka (*A*) near the base of Tuli Mons, surrounded by a dark flow (*B*), which was subsequently covered by flows of intermediate radar-brightness (*C*, arrows indicate flow direction) that contain channels.

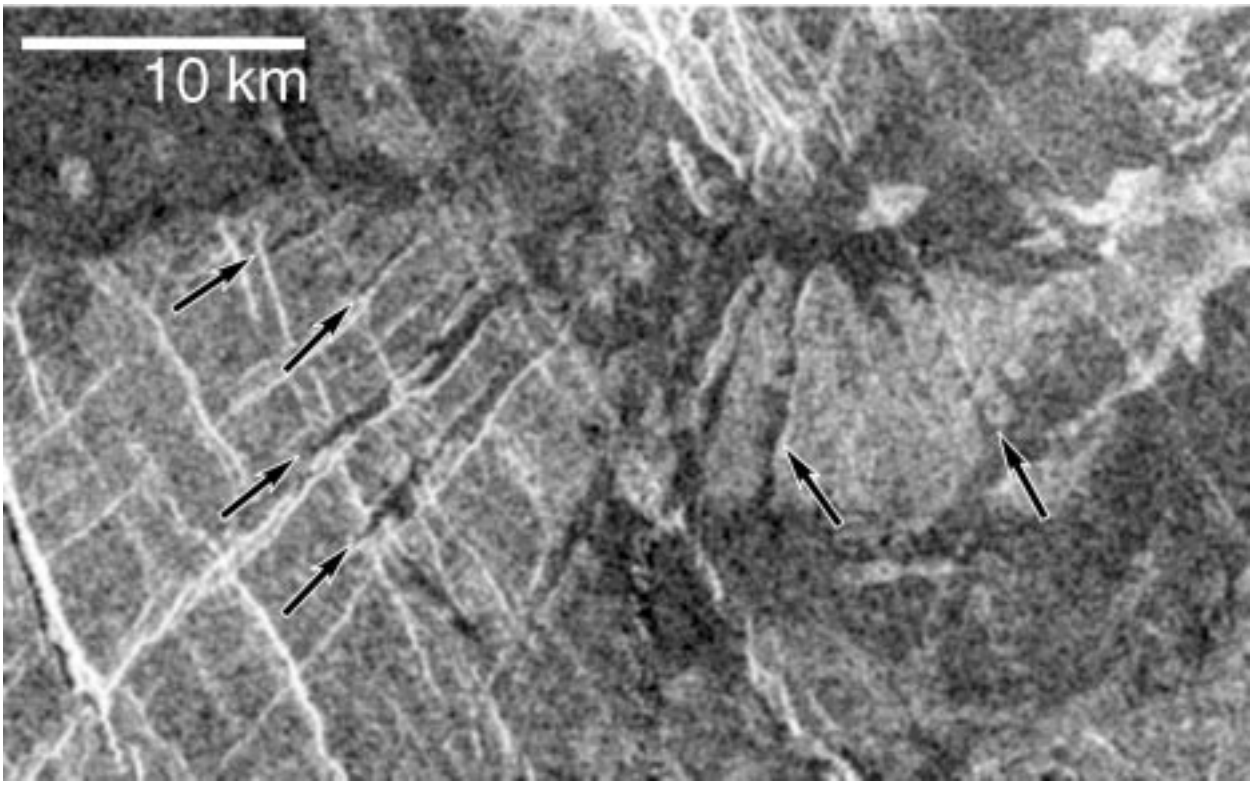

Figure 4.11. Radar-dark flows channeled along rift-related graben (arrows labeled *fl*) at Zipaltonal Fluctus. Variable offsets of surface fractures (resulting in radar brightness changes; arrows labeled *r*) indicate that volcanic resurfacing and tectonic processes were active over extended, overlapping periods of time (see text for discussion).

[Roberts et al., 1992]). Preliminary modeling suggests that the lack of a bright radar-facing margin places an upper limit of ~15 m on flow thickness for the flow fields examined [Kreslavsky and Vdovichenko, 1997].

Based on the flow stratigraphy, no temporal progression in emplacement style is observed, suggesting that the full suite of observed flow morphologies may form throughout flow field development. This finding is consistent with eruptive histories of terrestrial and other Venusian volcanic centers [Stofan et al., 2001].

4.5.6. Spatially Associated Features

In addition to complex intra-flow field stratigraphy, lava flows exhibit complex superposition relationships with other features that are spatially related to the flow fields. Small shields and/or lava domes are commonly associated with the flow fields and typically range from 2-10 km diameter. Small edifices display a wide range of morphologies at various scales (Figure 4.6). At the large scale, edifices may display margins that are scalloped or smooth and lobate, and may have summits that are peaked or flat, and display one or more pits. At the small scale, surfaces may be rough or smooth at the radar wavelength. Some shields and domes are covered by flows, whereas others appear to be superposed on the flow fields. At a few locations within the flow fields, flows appear to be emplaced both before and after construction of an individual edifice (Figures 4.8b, 4.12), although in most cases temporal relationships are ambiguous.

Other features, such as coronae (Figure 4.2e), paterae (Figure 4.2c), and rifts (Figures 4.2a,b,d,e), have developed preceding, during, and/or after flow field development. Temporal relationships are frequently unclear, and the chronology of feature formation may be complex.

a

Figure 4.12. Formation of volcanic constructs during flow field development. (a) Intermediate edifice (indicated by arrow, ~20 km diameter) with radial fractures at its center and radial flows on its surface superposes some flows at Zipaltonal Fluctus and is partially covered by subsequent flows. Margins of the construct are discernible along its western and southern edges, and are buried by radar-dark to -intermediate flows elsewhere. (b) Two small domes are interpreted to be superposed on flows from Tuli Mons and covered by subsequently emplaced lava flows, although relative age relationships are difficult to determine. Interpretive map shows proposed original flow and dome margins from which temporal relationships have been derived, arrows indicate flow direction.

b

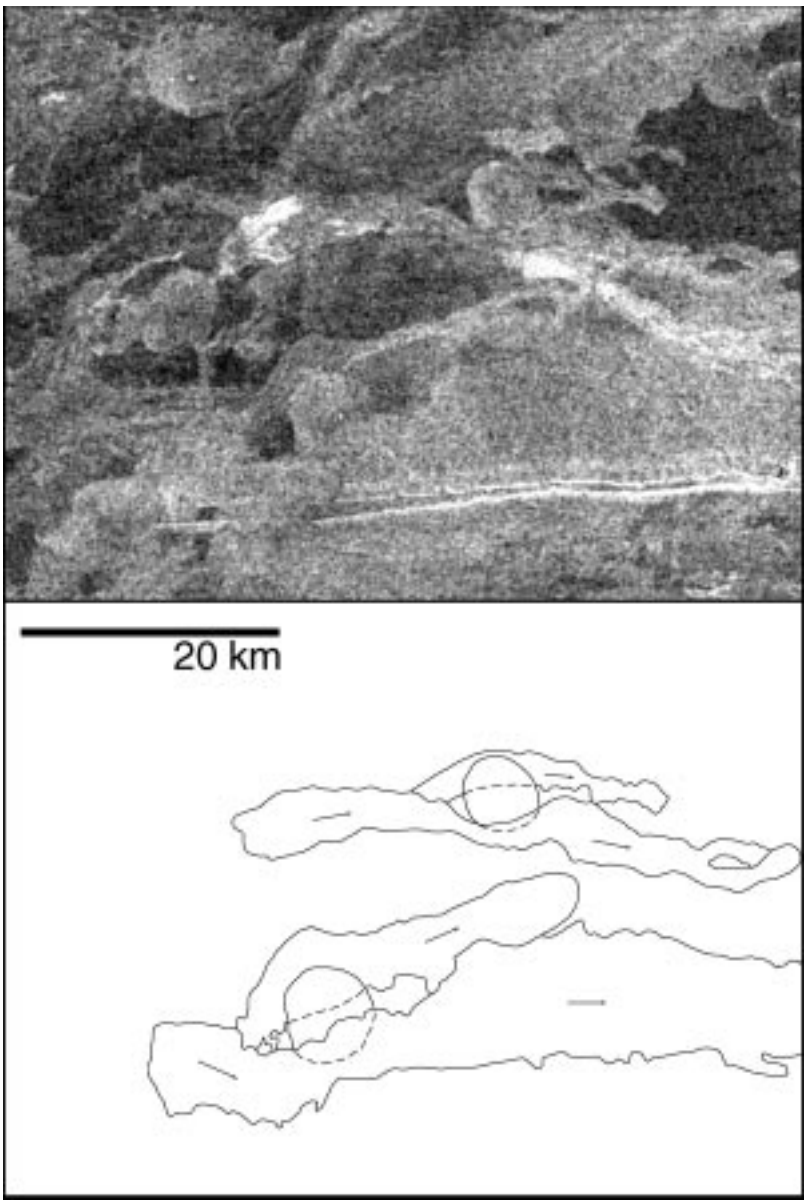

Figure 4.12. (continued)

For example, along an individual trend, some rifts associated with the Zipaltonal Fluctus proximal region display differences in radar brightness that are spatially correlated with lava flows (Figure 4.11). This appearance is interpreted to indicate that portions of these fractures were periodically resurfaced as the fractures developed, producing differences in the fracture offset along an individual trend. More generally stated, this indicates that eruptions occurred periodically over the duration of rifting, suggesting that both volcanic and tectonic activity occurred over protracted durations. All of the flow fields examined superpose volcanic plains units locally, although only the uppermost flow field surface may be inferred to be younger than the plains.

4.5.7. Radar Backscatter Characteristics and Comparison to Terrestrial Lava Flows

Radar backscatter characteristics of flow units within the five Venusian flow fields are compared, using data averaged over a 3×3 pixel grid to provide representative values (Figure 4.13). The flow fields display a significant range of backscatter coefficients between the roughest and smoothest surfaces, from ~16 to 24 dB over a 1-4° range of incidence. Although each flow field displays numerous radar-bright and -dark flows, the actual calibrated radar backscatter coefficients vary, showing a dependence on the incidence angle. This behavior is characterized by the empirically-derived formula of Muhleman [1964], which describes Venus' average surface backscatter coefficient as a function of incidence angle (Figure 4.13) [see also Pettengill et al., 1988; Ford and Plaut, 1993; Campbell, 1995]. Each of the Venusian flow fields examined in the current study displays lobes with higher and lower radar backscatter coefficients with respect to incidence angle than the global average. Although Figure 4.13 suggests a

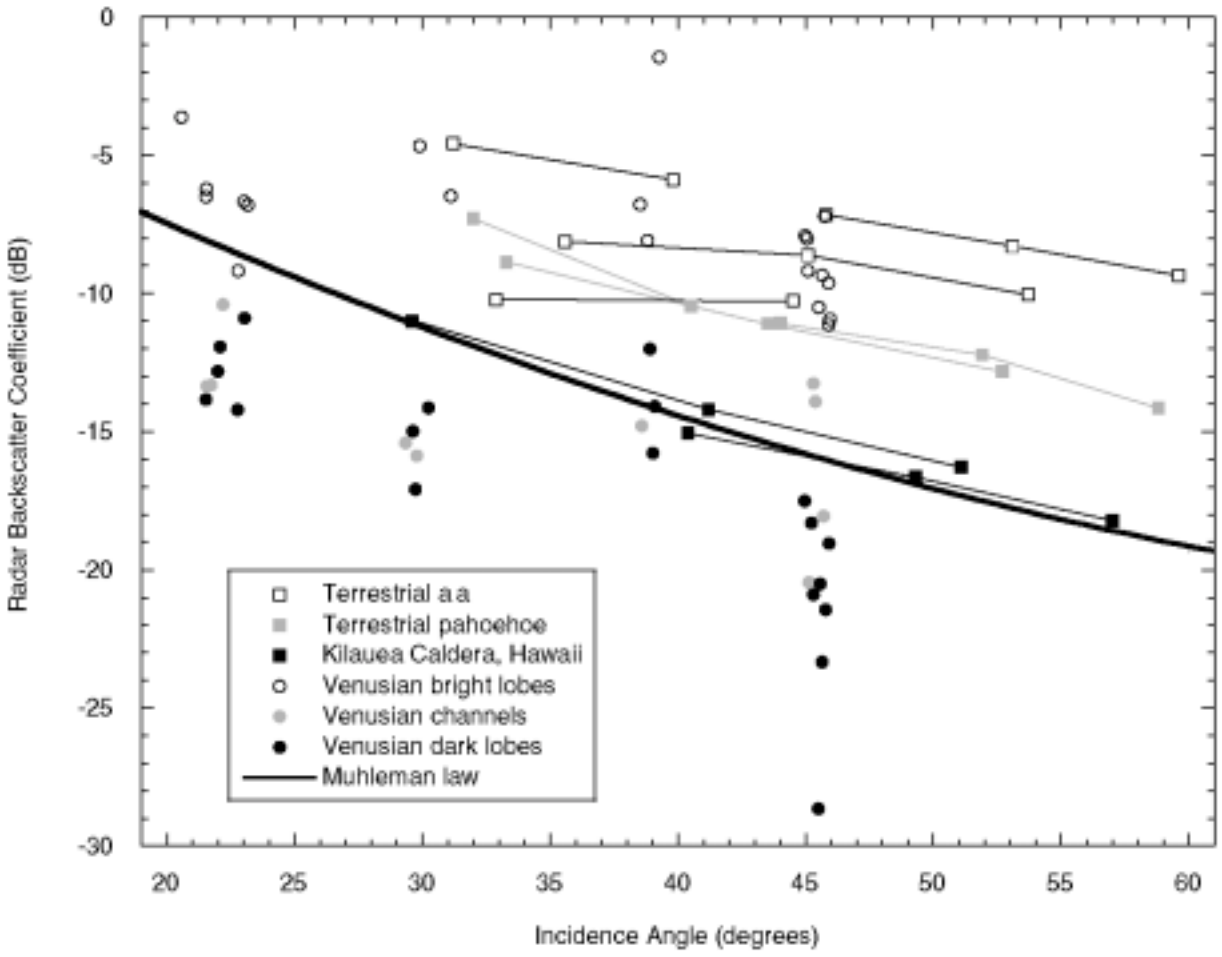

Figure 4.13. Radar backscatter coefficient vs. incidence angle for venusian flow fields and terrestrial flow surfaces. Venus data are averaged 3×3 pixel grids collected for each of the flow fields as part of this study. Terrestrial values are averaged AIRSAR data [Plaut, 1991; Plaut et al., 2002], interpolated from C- and L-bands (5.6 and 24 cm, respectively) to S-band (12.6 cm) wavelength; lines connecting points indicate flow surfaces imaged at multiple incidence angles. The Muhleman [1964] law represents the average scattering for the surface of Venus with respect to incidence angle.

dichotomy between radar-bright and -dark flows, lobes within each flow field display a continuum of radar backscatter coefficients. Channels within the flow fields tend to have intermediate to low radar backscatter coefficients.

Venusian lava flow features are typically orders of magnitude larger than their terrestrial counterparts [e.g. Guest et al., 1987; Pinkerton and Wilson, 1994; Byrnes and Crown, 2001]. This may result from higher effusion rates and volumes, higher eruption temperatures, lower viscosity due to lava chemistry, lower erupted crystal content, and/or the high atmospheric temperature and pressure; these differences are also expected to affect the surface roughness of the lava flows [e.g. Wilson and Head, 1983; Head and Wilson, 1986; Head et al., 1992; Bridges, 1997; Stofan et al., 2001].

In order to compare radar backscatter characteristics of Venusian flow features with those of terrestrial lava flows, AIRSAR (airborne multipolarization, multifrequency synthetic-aperture radar) data were utilized for lava flows in and around Kilauea Caldera (Kilauea Volcano, Hawai'i, USA) [Plaut et al., 2002] and from Pisgah Crater (Mojave Desert, California, USA) [Plaut, 1991]. This analysis compares Magellan SHH data that have been averaged over 3×3 pixel grids with AIRSAR data that derives SHH values using a linear interpolation of pixel-averaged CHH (5.7 cm) and LHH (25 cm) data (Figure 4.13). For a given incidence angle, the Venusian flows have lobes that display similar to lower radar backscatter coefficients than the terrestrial flows. This is significant for interpretation of morphologic analogs. For example, dark-surfaced lobes with bright margins are interpreted to be sheet flows whose margins have undergone significant deformation, on average over the spatial extent of the individual pixels. Higher backscatter coefficients associated with the flow margins may result from minor deformation across an entire pixel, small areas of significant surface roughness averaged with

smooth surfaces, or some intermediate case. Deformation probably resulted from increased flow viscosity due to cooling. As an alternative to deformation, flow margins may display higher backscatter coefficients due to an abundance of rough-surfaced breakouts along the lobe periphery. The range of radar backscatter coefficients are also significant because they indicate that the lava flow fields examined in this study have similar surface characteristics to flows at other Venusian volcanic centers [e.g. Campbell and Campbell, 1992; Campbell and Rogers, 1994], suggesting that the emplacement processes for the flow fields examined herein may be common on Venus.

4.6. Conclusions

Analyses of the morphology, stratigraphy, and surface roughness properties of five Venusian lava flow fields were conducted to investigate flow field emplacement processes and the development of volcanic centers. The flow fields all display digitate morphologies and exhibit shallow slopes (maximum slopes 0.10-2.35° over 100 km baselines) over large areas (~80,000 to 820,000 km^2). Flow field surfaces display complex patterns due to emplacement of abundant, typically radar-dark channels and numerous radar-dark, -intermediate, and -bright lobes of various sizes and planform morphologies. Flow field surfaces tend to show the greatest variation in radar brightness within proximal regions, and surfaces of individual lobes within the flow fields may display uniform or varied radar brightness. However, at the Magellan FMAP wavelength and pixel size (12.6 cm, 75 m/pixel), individual flow lobes are similar or smoother than terrestrial lava flows. The Venusian flow fields display similarities in radar backscatter patterns and planform morphologies to terrestrial lava flow fields, although the larger scale and

larger range in surface roughness of Venusian features suggest that simple analogies may not be sufficient.

The flow fields developed through emplacement of both simple and compound flow lobes, based on lobe morphologies and branching patterns. In addition to surface-fed lava extending directly from vent regions, the presence of tube-fed flows is suggested by distributary morphologies from local sources within the flow fields and the presence of discontinuous channels. Flow inflation may have also occurred within medial and distal portions of some flow fields, as lobes displaying discrete zones of increased radar brightness are observed. Alternatively, these zones may be attributed to differences in emplacement conditions across a flow lobe.

The flow fields display a variety of lobe and channel morphologies, characterized by variations in branching, surface roughness patterns, and margin sinuosity. Channels commonly show radar-dark surfaces with adjacent radar-bright levees. Several lines of evidence suggest that flow lobes within the five selected flow fields are relatively thin (less than a few tens of meters), such as the high degree of lobe overlap, lack of flow deflection by preexisting flows (for radar-bright lobes), and absence of lobe margin radar brightness differences due to the radar look direction. Some correlation appears to be present between radar brightness and planform morphology, flow thickness, and insensitivity to underlying topography, suggesting that increased radar backscatter may be indicative of higher flow viscosities, although post-emplacement modification (such as by flow inflation) complicates this relationship. This interpretation is further supported by the tendency of radar-dark flows to occur in proximal regions and in channel systems, where we expect hotter, less viscous flows to have been emplaced.

The selected Venusian volcanic centers developed compound flow fields with complex emplacement histories, indicated by overlapping relationships of numerous, discrete lobes and channel networks. Complicated superposition relationships within the flow fields and with associated features, such as shields, domes and coronae, suggest the volcanic centers were active over protracted durations. The uppermost flow surfaces are among the youngest geologic units locally, although flow fields both bury tectonic features and are deformed by tectonic activity. The development of these flow fields does not indicate any evolutionary trend in eruptive styles within a flow field, nor any consistent temporal sequence relative to other tectonic or volcanic features.

Chapter 5

Constraints on lava flow emplacement derived from radar remote sensing: Comparison of lava flow fields on Earth and Venus

5.1. Introduction

Lava flow fields are common on large, rocky bodies in the solar system. Understanding flow field emplacement is necessary for accurate assessment and effective mitigation of lava flow hazards, and may be used to constrain volcanic resurfacing in other planetary environments. Examination of extra-terrestrial flow fields is important for understanding the geologic history of those bodies, and provides a comparison to flow fields on Earth that may be used to refine volcanologic models. In particular, lava flow fields on Venus are a particularly useful planetary analog because they are young (relative to those on the Moon and Mercury), are well exposed (relative to those on Mars), and because Venus is similar in size and composition to the Earth (relative to Io and Triton).

The objectives of this research are to further previous characterizations of surface units within the Mauna Ulu lava flow field (Kilauea Volcano, Hawai'i) [Byrnes and Crown, 2001; Byrnes et al., 2002], to document relationships between surface unit characteristics and radar remote sensing signatures, and to use the documented relationships to better understand Venusian volcanism, based on the analysis of Byrnes and Crown [2002]. Field observations were made to determine cm- to m-scale surface characteristics associated with different lava flow units and to relate these characteristics to radar remote sensing data. Analyses of radar data utilized recently acquired AIRSAR (airborne Synthetic Aperture Radar) datasets. These datasets provide a means to extend the spectral coverage of a previous study within the Mauna Ulu flow field, which was based on field observations coupled with visible- and thermal-wavelength data

analyses [Byrnes et al., 2002]. The current study also further develops a field and remote sensing approach to mapping and interpreting the emplacement of complex volcanic surfaces.

5.2. Background

The emplacement of compound lava flow fields is complex. Flow units display complicated sequences of interfingered and overlapping lobes emplaced under varying conditions during the development of the flow field. Modification of the flow surface during and after emplacement of the lobes further complicates interpretations of flow emplacement that are based on the resulting flow field surface. Modification takes place in many forms and at various scales, including weathering and coating of the flow surface [e.g. Kahle et al., 1988], spallation of the surface crust [e.g. Wilmoth and Walker, 1993], and lava flow inflation [e.g. Walker, 1991; Hon et al., 1994].

Inflation is the vertical growth of a flow unit due to continued influx of lava beneath the surface crust. Hon et al. [1994] observed that pahoehoe lobe morphologies may be modified due to the processes of coalescence and inflation [see also Walker, 1991; Cashman and Kauahikaua, 1997]. Pahoehoe toes that are emplaced individually may coalesce with other toes to form broad, flat sheets; evidence of this is preserved in some localities where subdued ropes and partial toe margins are preserved on the surfaces of sheets [Byrnes and Crown, 2001]. Inflation is commonly most significant in portions of the flow field that have relatively horizontal (<2°) underlying slopes, but typically occurs to various extents throughout the medial and distal portions of flow fields [Swanson, 1973; Hon et al., 1994]. Inflation at relatively small scales produces cracks and offsets in sheets and tilted slabs of surface crust in toey lobes. Pahoehoe

flow fields also display evidence of flow inflation at larger scales in the form of tumuli, which are roughly domical inflation features typically several meters high and meters to tens of meters wide [Walker, 1991; Rossi and Gudmundsson, 1996; Anderson et al., 1999].

5.3. The Mauna Ulu flow field

The Mauna Ulu satellitic shield is located on the upper east rift zone of Kilauea Volcano. Lasting from May 1969 to July 1974, the Mauna Ulu eruption represented the longest-lived, near-continuous rift zone activity that had been documented for Kilauea Volcano up to that time [Tilling et al., 1987]. Two episodes of activity from Mauna Ulu and local vents emplaced an ~61 km^2 flow field, developing an extensive lava tube network that fed flows over 12 km from the vent region to the Pacific Ocean [Swanson, 1973; Holcomb, 1976, 1987; Swanson et al., 1979; Tilling et al., 1987]. Holcomb [1987] illustrates the medial to distal distribution of inflated tube-fed pahoehoe, described by Swanson [1973] as dense, hummocky pahoehoe produced from lava tubes. Proximal (near-vent) pahoehoe flows were surface-fed (shelly or fountain-fed), and 'a'a is distributed throughout the flow field [Swanson, 1973; Holcomb, 1976, 1987].

5.4. Field characterization of the Mauna Ulu flow field

5.4.1. Previous field characterization of Mauna Ulu surface units

A recent characterization of lava flow surface units utilized field investigations and remote sensing analyses to constrain emplacement of the flow field [Byrnes et al., 2002]. These field studies provided descriptions of units in terms of morphology and color, context within the flow field and local stratigraphic relationships, and vesicularity, crust spallation, phenocryst

abundance, and microtopography. The study analyzed flow units previously described by Swanson [1973] and Byrnes and Crown [2001] as well as transitions between those units.

Byrnes and Crown [2001] and Byrnes et al. [2002] describe four pahoehoe surface units that dominate the medial portion of the Mauna Ulu flow field and that have characteristic morphologies produced by local flow emplacement conditions. Unit I exposures typically have morphologies at the dm- to m-scale that are flat or display ropy, channelized zones, and range from individual sheets to composite surfaces composed of coalesced toes and sheets. The unit generally exhibits relatively low degrees of crust spallation (areas where the outer glassy rind has flaked off). Surfaces display bronzy, glassy crusts, as well as areas where the crust has spalled, which are locally concentrated in portions that have undergone deformation due to folding or inflation. Unit II morphologies consist of lobes of toe networks displaying low degrees of spallation, and may be smooth or display small, ropy, channelized zones. Unit II surface crusts and spallation surfaces are similar to those of unit I.

Unit III lobes consist of toe networks that are dark and may be smooth (at the dm-scale), ropy, or platy. Toes tend to be more equant, lobes are thicker, and crust spallation is more prevalent relative to toes of unit II. Unit III exposures are generally the last unit emplaced locally, based on flow stratigraphy, and are fed as breakouts from inflated portions of other pahoehoe surface units as well as from interior zones of 'a'a lobes. Unit IV exposures are typically large and commonly bound by levees. They display highly disrupted surfaces composed of jumbled plates and slabs exhibiting textures associated with units I, II, and III that are intermixed with 'a'a clinkers. 'A'a surfaces typically lack glass, may be dark gray to red, and are rough at the mm- to dm-scale.

Other varieties of pahoehoe observed within the Mauna Ulu flow field included surface-fed and transitional units. The fountain-fed pahoehoe units are generally large and display a relatively smooth, bronzy, glassy surface crust and a range of morphologies consistent with emplacement as sheets, channels, and large (m-scale), elongate toes. Shelly pahoehoe displays a similar bronzy appearance, although it is not typically as smooth and glassy. Shelly pahoehoe may be emplaced as sheets or toes, is typically hollow beneath the upper few centimeters, and is transitional to a disrupted (unit IV-type) surface with collapse of the crust. Intermediate units that display transitions to both surface-fed varieties were also observed, indicated by Swanson [1973] to have formed from low (<100 m) lava fountains.

Further investigation of these units is required to assess the significance of lava flow inflation as well as document larger-scale (dm to m) characteristics, which affect backscatter properties of radar remote sensing data. Analysis of the flow field using radar data will provide a quantitative assessment of surface unit roughness as well as allow for comparison to a recent investigation of flow morphologies observed in Magellan radar data for several Venusian lava flow fields [Byrnes and Crown, 2002].

5.4.2. Methodology

In the current study, field observations were made to document surface parameters related to the emplacement and post-emplacement modification of flow surfaces in order to further the surface characterization of Byrnes and Crown [2001] and Byrnes et al. [2002] as well as to provide a comparison to radar remote sensing data. These observations took place over a large portion of the flow field. Specific sites were selected that represent typical unit exposures as well as the range of morphologies and surface textures observed (Figure 5.1). The selected study sites range

in size from ~7 to 3000 m^2 and include 15 exposures of unit I, 10 exposures of unit II, 7 exposures of unit III, 4 exposures of unit IV, and 4 'a'a exposures (Table 5.1), which were geolocated using a high-resolution (~10 cm horizontal accuracy) differential Global Positioning System (dGPS; see Figure 5.1 and Appendix A). Descriptions of each site were compiled, including local surface units present, topographic characteristics, and a semi-quantitative assessment of fracturing and inflation. Topographic characterization included a qualitative description of the exposure surface at the cm- to m-scale as well as a measurement of the maximum relief displayed over a 1-m horizontal distance within the unit. Each pahoehoe unit was also characterized in terms of the scale and degree of fracturing and apparent inflation that had occurred. Surface fractures and unit inflation were assessed at the scale of toes (small-scale), small lobes and channels (intermediate-scale), and large lobes and tumuli (large-scale), and described as being displayed to a minor, moderate, or significant degree. Because fracturing is ubiquitous at the surface of 'a'a lobes, they do not preserve a continuous surface crust and inflation is not apparent. Observations were also made of near-vent surface-fed pahoehoe units, for comparison with the other surface units presented herein.

5.4.3. Results

Topographic characteristics are related to the primary emplacement morphology and secondary modification of the surface units. Primary morphologies include sheets (unit I), toe networks (units II and III) forming "monolayer" and "centrally ridged" lobes, and disrupted channels (unit IV) (see Crown and Baloga [1999] for discussion of toe network morphologies). Secondary modification occurs by such processes as inflation, drainage followed by crust

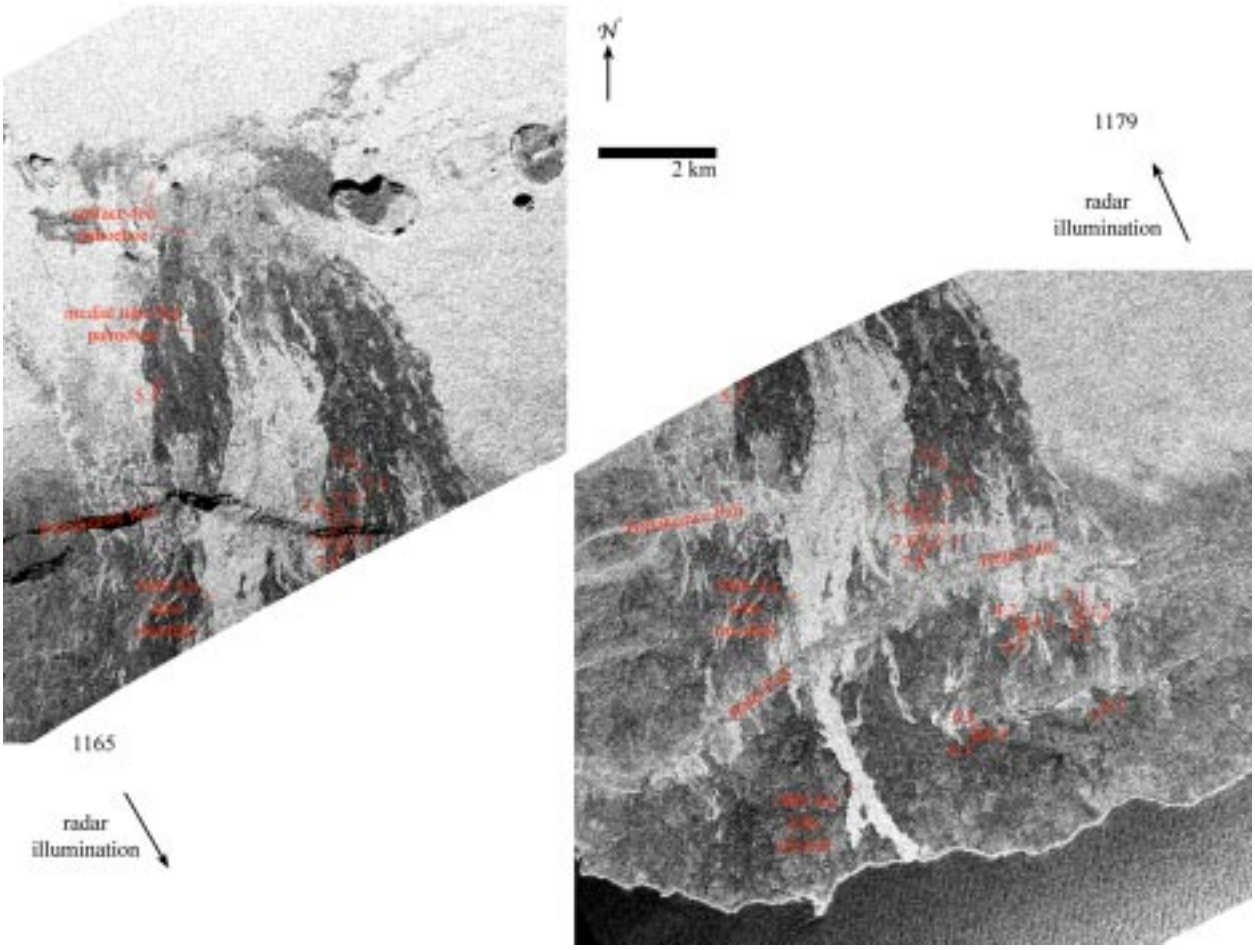

Figure 5.1. Location map of study sites and areas sampled to compare radar backscatter statistics within the Mauna Ulu flow field. Left panel shows the 1165 flight line and the right panel shows the 1179 flight line. Radar illumination direction is indicated for each dataset.

Table 5.1. Field characterization of surface units

site	maximum relief (cm)	fracturing[◊]	inflation[◊]	crust spalled (%)[#]
Unit I				
3.1.d	25	small[2] and intermediate[2]	small[1] and intermediate[1]	10
3.2.a	22	small[2] and intermediate[2]	small[1] and intermediate[1]	5
3.2.b[†]	34	—	—	90
3.3.a	30	small[2]	small[1]	5
4.1.c	15	small[2-3] and intermediate[2-3]	intermediate[2]	5
4.3.b	37	small[2] and intermediate[2]	small[2]	40
6.1.a	80	intermediate[2] and large[2]	small[1] and large[2]	60
6.3.a	20	intermediate[1-2]	none	20
6.4.a	13	intermediate[3]	large[2-3]	70
6.5.a	24	intermediate[2]	large[3]	80
7.1.aA	16	small[1]	none	<5
7.2.a	50	small[2] and intermediate[2]	small[2] and intermediate[2]	10
7.3.a	21	small[3] and intermediate[2]	small[1], intermediate[2], and large[1]	10
7.4.a	35	intermediate[2]	intermediate[2]	10
7.6.a	16	intermediate[2]	intermediate[2]	20
mean	29 ± 12	—	—	29 ± 18
range	13 - 80	small to large	none to large	<5 - 90
Unit II				
3.1.a	55	—	small[1]	20
4.1.b	20	small[3] and intermediate[2]	small[1], intermediate[2], and large[2]	50
5.1.a	19	small[2]	none	20
6.1.a1	28	—	—	50
7.1.aC	41	small[1-2]	small[1] and intermediate[2]	20
7.2.a1	60	intermediate[2]	small[2]	70
7.4.a1	35	small[1] and intermediate[2]	small[1] and intermediate[2]	50
7.5.aA	25	intermediate[2]	intermediate[2]	—
7.6.a1	14	—	—	10
7.7.a	22	intermediate[1]	intermediate[1]	10
mean	32 ± 13	—	—	33 ± 19
range	14 - 60	small to intermediate	none to large	10 - 70

[◊]see text for description of scales at which fracturing and inflation occur

[1]minor degree of inflation/fracturing at scale indicated

[2]moderate degree of inflation/fracturing at scale indicated

[3]significant degree of inflation/fracturing at scale indicated

[#]values from *Byrnes et al.* [2002]

[†]unit I exposure at site 3.2.b displays a ropy, channelized sheet surface (rather than the more typical flat sheet surface)

Table 5.1. (continued)

site	maximum relief (cm)	fracturing[◊]	inflation[◊]	crust spalled (%)[#]
Unit III				
3.1.b	93	—	small[1] and intermediate[1]	90
4.1.a	50	small[2]	small[2]	80
4.2.a	100	small[1] and intermediate[2]	small[1-2]	80
4.2.b	80	small[1] and intermediate[3]	small[1] and intermediate[3]	90
5.1.b[‡]	100	intermediate[2]	intermediate[2]	70
7.1.aB	54	intermediate[2]	none	40
7.5.aC	30	—	—	70
mean	72 ± 24	—	—	74 ± 12
range	30 - 100	small to intermediate	none to intermediate	40 - 90
Unit IV				
3.3.b	56	small[1]	none	—
4.3.a	84	intermediate[2]	intermediate[2]	—
7.1.aD	50	—	—	—
7.5.aB	30	—	—	—
mean	55 ± 15	—	—	—
range	30 - 84	small to intermediate	none and intermediate	—
'a'a				
6.3.b	115	—	—	—
7.1.aE	35	—	—	—
7.6.a2	25	—	—	—
7.8.a	50	—	—	—
mean	56 ± 32	—	—	—
range	25 - 115	—	—	—

[◊]see text for description of scales at which fracturing and inflation occur

[1]minor degree of inflation/fracturing at scale indicated

[2]moderate degree of inflation/fracturing at scale indicated

[3]significant degree of inflation/fracturing at scale indicated

[#]values from *Byrnes et al.* [2002]

[‡]a breakout of higher viscosity lava at site 5.1.b displays 54 cm maximum relief

collapse, and unit remobilization. Together, primary emplacement and secondary modification may produce topographically complex surfaces. For example, Figure 5.2 illustrates an uninflated unit I sheet, which displays a typical flat, bronzy, glassy surface with minimal crust spallation. Figure 5.3 shows a nearby exposure of unit I that displays an intermediate scale of inflation and from which a small, uninflated unit III lobe emanates. Figure 5.4 provides an example of large scale inflation of a unit I exposure, producing a tumulus from which a large, uninflated unit III exposure is fed. Not all inflation increases surface roughness, however. Figure 5.5 illustrates an example of pahoehoe toes and small sheets that experienced coalescence and small-scale inflation during emplacement, resulting in a broad, relatively flat unit I surface.

A summary of the field characterization is provided in Table 5.1. The average maximum relief measured at the selected sites increases from unit I (29 cm) and unit II (32 cm) to unit IV (55 cm) and 'a'a (56 cm) to unit III (72 cm). All of the selected pahoehoe sites display surface fractures. Units I-IV display small- to intermediate-scale fracturing, and unit I additionally displays fracturing at the large scale. The scale and degree of fracturing reported for unit IV does not include the fractures that are responsible for forming the slabs of disrupted pahoehoe within the unit, which are ubiquitous. Fractures appear to be predominantly associated with flow inflation (at small, intermediate, and large scales; Figures 5.3-5.4) and cooling (at the small scale; Figure 5.2). Apparent inflation is more variable among the pahoehoe units, observed at small, intermediate, and large scales for units I and II, small and intermediate scales for unit III, and at the intermediate scale for unit IV. No inflation was apparent for at least one exposure of each variety of pahoehoe unit.

Figure 5.2. Uninflated unit I sheet. Arrow labeled *c* points out polygonal cooling cracks that are present across the upper crust of the exposure.

Figure 5.3. Inflated unit I sheet (*I*), from which a lobe of dark, unit III toes emanates (*III*).

Figure 5.4. Tumulus of unit I, from which an uninflated unit III lobe emanates. Note the upturned slab (*s*), which was presumably emplaced as a horizontal unit I sheet.

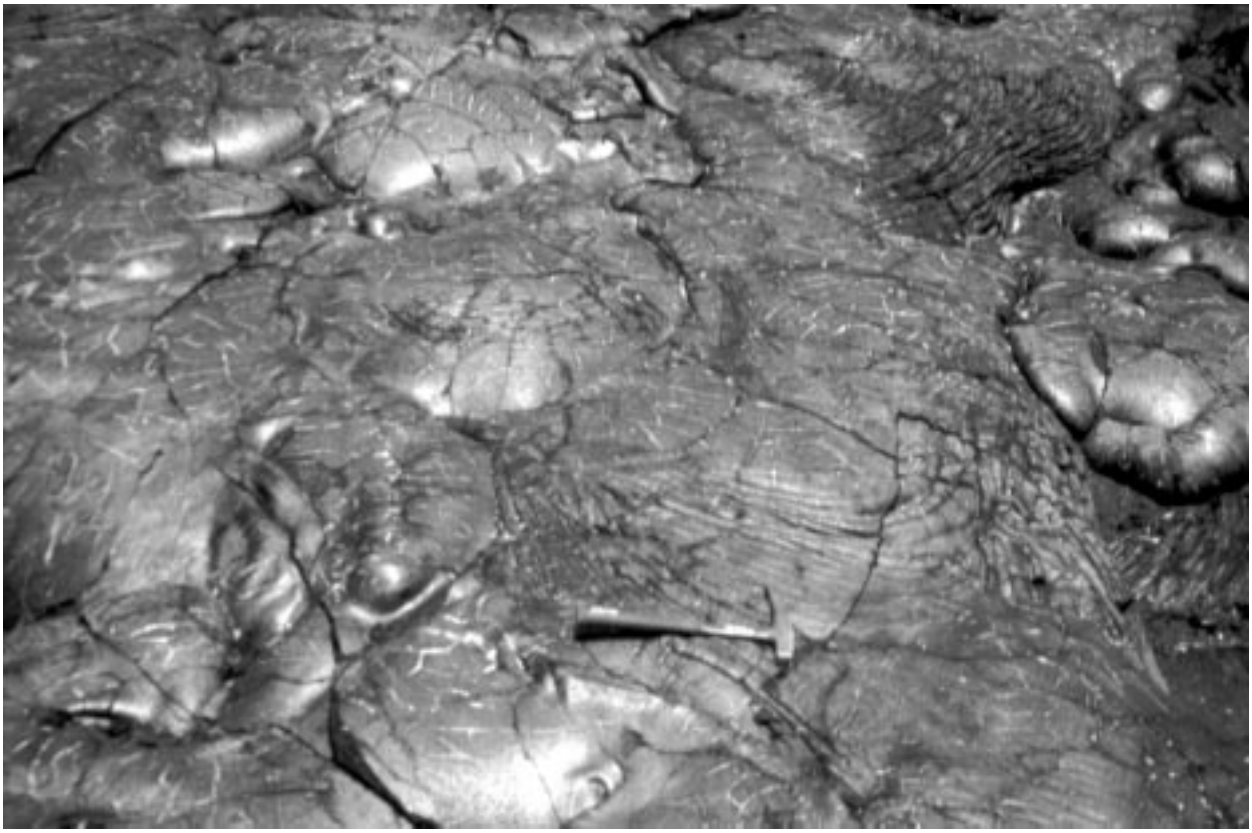

Figure 5.5. Unit I exposure, formed by coalescence and small-scale inflation of toes and small sheets.

Surface-fed pahoehoe units were also observed for comparison with the tube-fed pahoehoe units. The maximum relief associated with shelly pahoehoe units is typically related to collapse of the surface crust and is commonly several dm (Figure 5.6). Maximum relief for fountain-fed pahoehoe is predominantly controlled by the unit morphology (sheet, toe network, or channel) and may be >2 m for drained channels (Figure 5.7). Fractures commonly form on shelly pahoehoe and are associated with collapse of the surface crust. Fractures are not generally significant for fountain-fed pahoehoe units. Inflation is typically not associated with the surface-fed pahoehoe units, which is consistent with an overall trend of increasing inflation progressively downflow from the vent.

5.4.4. Significance

The surface units examined in this study display a wide range in topographic characteristics and in style and degree of fracturing and inflation. These three parameters are largely related, as most of the fracturing appears to be associated with inflation, which also accounts for much of the unit topography. Fracturing and inflation produce secondary features in that these processes modify surface units after the primary formation of a unit crust. For this reason, the development of surface unit topography is complex. The degree of fracturing and inflation provide information about the local supply of lava during and after initial emplacement of the unit. The lack of large-scale fracturing and inflation of unit III is consistent with previous observations that unit III typically emanates as breakouts from inflated portions of other units [Byrnes and Crown, 2001; Byrnes et al., 2002]. Furthermore, unit III typically appears to have had relatively low local supply rates and higher flow viscosity during emplacement, both of

Figure 5.6. Shelly pahoehoe in the proximal region. Mauna Loa is in the background, and a portion of Pu'u Huluhulu is visible along the right edge of the image.

Figure 5.7. Drained, fountain-fed channel in the proximal region of the flow field.

which would tend to hinder flow inflation. The limited inflation observed for unit IV may be related to the formation of this unit through the remobilization of primary tube-fed pahoehoe units (I-III). The remobilization may be associated (at least initially) with inflation, but if this is the case the record of inflation is not preserved in the resultant unit IV exposures.

Table 5.1 also includes the degree of spallation reported by Byrnes et al. [2002] (expressed as a percent of the surface crust that has been spalled vs. intact). The mean values of percent crust spalled and maximum relief (in cm) appear to be correlated. In general, units that have undergone a greater degree of crust spallation have also had more extensive inflation, which commonly produces offsets along fractures. Spallation tends to increase with increasing degree of inflation, but shows no clear correlation with scale of inflation.

5.5. Radar-wavelength characterization of the Mauna Ulu flow field

5.5.1. Radar remote sensing of volcanic surfaces

Radar data have been used to characterize volcanic surfaces and distinguish them from surfaces such as playa surfaces on Earth [e.g. Campbell et al., 1993] and fluidized impact ejecta [e.g. Johnson and Baker, 1994] and debris aprons on Venus [e.g. Bulmer and Guest, 1996]. Analyses of volcanic surfaces include delineation of lava flow textures and surface roughness [e.g. Greeley and Martel, 1988; Gaddis et al., 1989, 1990; Campbell and Campbell, 1992; Plaut, 1991; Plaut and Arvidson, 1992; Bruno and Taylor, 1995; Campbell and Shepard, 1996; Byrnes and Crown, 2002], distinguishing lava flows from pyroclastic deposits [e.g. Gaddis et al., 1989], and mapping topography as well as detecting changes in topography using radar interferometry [e.g. Zebker et al., 1992, 1996; Rowland et al., 1999]. These studies demonstrate that radar

responds to differences in surface roughness, incidence angle, and dielectric constant (a material property), and that wavelength, polarization, and resolution of the radar significantly affect data interpretation.

5.5.2. The AIRSAR datasets

AIRSAR is the NASA/JPL airborne multipolarization, multifrequency Synthetic Aperture Radar instrument [Zebker et al., 1992; see also JPL AIRSAR documents available at http://airsar.jpl.nasa.gov/documents/instrument.htm]. The instrument may be run in one of two modes of data collection: 1) POLSAR, in which full-polarization data are collected at C-band (5.7 cm), L-band (24 cm), and P-band (68 cm) wavelengths; and 2) TOPSAR, in which C-band is used to create a digital elevation model (DEM) onto which the other bands are projected and with which the other bands are corrected. TOPSAR data includes a local radar incidence angle map, calculated as the angle between the radar look direction and the normal to each surface element in the DEM. Two TOPSAR flight lines that were acquired October 11-12, 2000 during the PacRim II mission are examined in the current analyses.

5.5.3. Methodology

The L-band data for both flight lines were synthesized for HH (horizontal transmit-horizontal receive) and VV (vertical transmit-vertical receive) polarization combinations from the compressed Stokes matrix format using the Synthesize AIRSAR Data module of the ENVI software package (the Environment for Visualizing Images, Research Systems Inc.). The radar incidence data were scaled from DN to angle (in degrees), other data were scaled using dataset header information: C-band VV polarization (CVV) data were scaled using the "General Scale

Factor" and the DEM was scaled using the elevation increment and offset. The LHH, LVV, CVV, DEM, and incidence angle data were coregistered with dGPS data taken in the field during November 1999 and July 2001, as well as with the supervised classification of Byrnes and Crown [2001]. Warping of the bands was required to reproject the radar data to the WGS84 spheroid because the AIRSAR DEMs are projected onto a spherical approximation of the WGS84 spheroid, in reference to a peg point (refer to the AIRSAR Integrated Processor Documentation – Data Formats, version 0.15, available at http://airsar.jpl.nasa.gov/data/data_format.pdf). Warping of the radar data utilized a second-order polynomial and nearest neighbor resampling (in order to preserve original data values).

Average radar backscatter coefficients were calculated for the four tube-fed pahoehoe units defined for the medial portion of the Mauna Ulu flow field by using data masks created from the supervised classification of Byrnes and Crown [2001] with subsampled AIRSAR data. This analysis follows the methodology of Byrnes et al. [2002] and allows comparisons between the radar data and previously analyzed visible and thermal-infrared data. The mean values represent an average of 60255 pixels for unit I, 35315 pixels for unit II, 16182 pixels for unit III, and 13046 pixels for unit IV. Mean backscatter coefficients were also calculated for proximal surface-fed pahoehoe, additional exposures of medial tube-fed pahoehoe, medial 'a'a, and distal 'a'a (Figure 5.1, see also Appendix A). The surface-fed pahoehoe mean represents 20817 pixels of the proximal region in the area from which statistics were calculated for the previous analysis using ASTER data [Byrnes et al., 2002]. The additional medial tube-fed pahoehoe represents 22509 pixels of the portion of the Mauna Ulu flow field that was found to be smoothest at the small-scale (mm to cm), based on thermal infrared remote sensing [Byrnes et al., 2002]. The medial and distal 'a'a values represent 19044 and 17487 pixels, respectively, of the large 1969

'a'a lobe for which statistics were calculated (for the distal portion) in the analysis of Byrnes et al. [2002].

In order to provide a comparison to the previous Venusian flow field study of Byrnes and Crown [2002], SHH (12.6 cm, HH polarization combination) backscatter values were interpolated from the available AIRSAR data. To do this, an assumption was made that the ratio of CHH to CVV backscatter is equal to the ratio of LHH to LVV backscatter:

$$(1) \qquad \frac{\mathrm{CHH}}{\mathrm{CVV}} = \frac{\mathrm{LHH}}{\mathrm{LVV}}$$

SHH backscatter may be derived from CHH and LHH backscatter using a linear interpolation:

$$(2) \qquad \mathrm{SHH} = \mathrm{LHH} + \left[\left(\frac{11.4}{18.4}\right) \times (\mathrm{CHH} - \mathrm{LHH})\right]$$

following the methodology of Byrnes and Crown [2002]. Solving equation (1) for CHH backscatter and substituting into equation (2) yields an SHH backscatter coefficient interpolated from CVV, LHH, and LVV data:

$$(3) \qquad \mathrm{SHH} = \mathrm{LHH} + \left[\left(\frac{11.4}{18.4}\right) \times \left(\left(\frac{\mathrm{CVV} \times \mathrm{LHH}}{\mathrm{LVV}}\right) - \mathrm{LHH}\right)\right]$$

5.5.4. Results

Mean LHH backscatter coefficients calculated for this study are shown as a function of mean incidence angle in Figure 5.8, as are averaged AIRSAR backscatter values presented by

Plaut [1991] for lava flows at Pisgah Crater (Mojave Desert, California, USA) and Plaut et al. [2002] for lava flows of Kilauea Volcano. The lowest mean backscatter coefficient of the units sampled in this study is associated with medial tube-fed pahoehoe, followed successively by unit I, unit II, unit III, unit IV, surface-fed pahoehoe, medial 'a'a, and finally distal 'a'a. Note that the average incidence angle of the sampled units ranges from 41.7° to 60.3°. The pahoehoe units analyzed herein display LHH backscatter coefficients that are intermediate in value (-12.5 to –20.8 dB) as well as in range of values (ΔdB=8.3) relative to other pahoehoe surfaces (-10.2 to –17.6 dB, ΔdB=7.4 dB) and Kilauea Caldera surfaces (-14.6 to –27.6 dB, ΔdB=13 dB) analyzed by Plaut [1991] and Plaut et al. [2002]. 'A'a surfaces examined herein display lower, and a smaller range of, backscatter coefficients (-10.2 to -12.0 dB, ΔdB=1.8 dB) than other 'a'a surfaces (-5.2 to -10.6 dB, ΔdB=5.4 dB) examined by Plaut [1991] and Plaut et al. [2002]. Examination of the radar scenes indicates that superposition relationships are typically ambiguous.

Mean interpolated SHH backscatter coefficients derived in this study are shown as a function of mean incidence angle in Figure 5.9, as are averaged Venusian lava flow surfaces presented by Byrnes and Crown [2002]. The Mauna Ulu surface units display the same trend of increasing SHH backscatter that was calculated for LHH backscatter. The Mauna Ulu pahoehoe interpolated SHH backscatter coefficients calculated herein (-11.6 to –18.2 dB) are comparable to values for Venusian channels (-10.4 to –20.5 dB) and dark lobes (-10.9 to –28.6 dB), but display a smaller range of coefficients (ΔdB=6.6 vs. 10.1 and 17.7, respectively). Mauna Ulu 'a'a surfaces are comparable (-9.5 to –11.3 dB) to the lower end of values for Venusian bright lobes (-1.5 to –11.1 dB), but also display a more restricted range of backscatter coefficients (ΔdB=1.8 vs. 9.6). It should also be noted that all of the Mauna Ulu surface units display mean backscatter coefficients that are greater than the mean Venus surface (Figure 5.9).

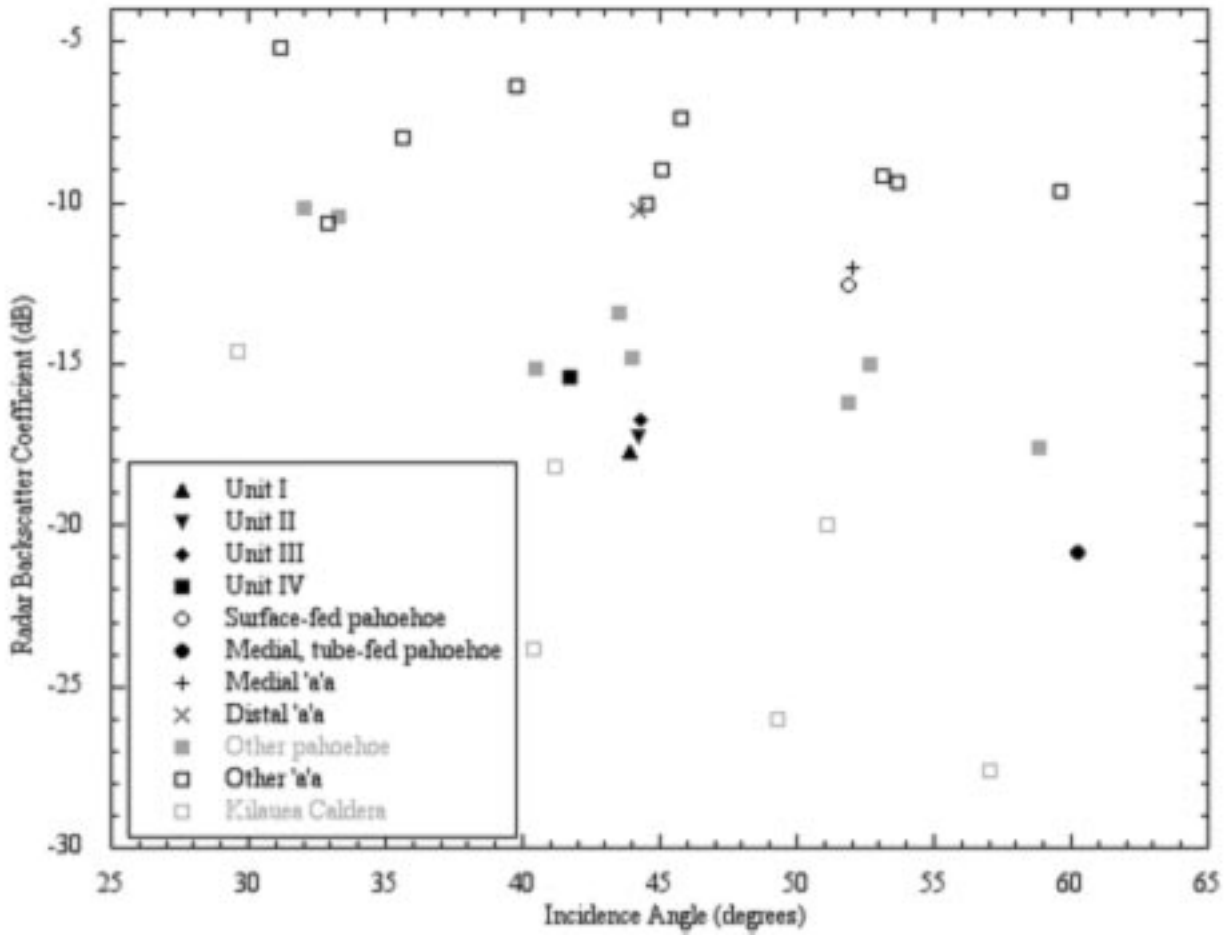

Figure 5.8. Comparison of AIRSAR LHH data of the surface units investigated herein and other pahoehoe, other 'a'a, and Kilauea Caldera flows of Plaut [1991] and Plaut et al. [2002].

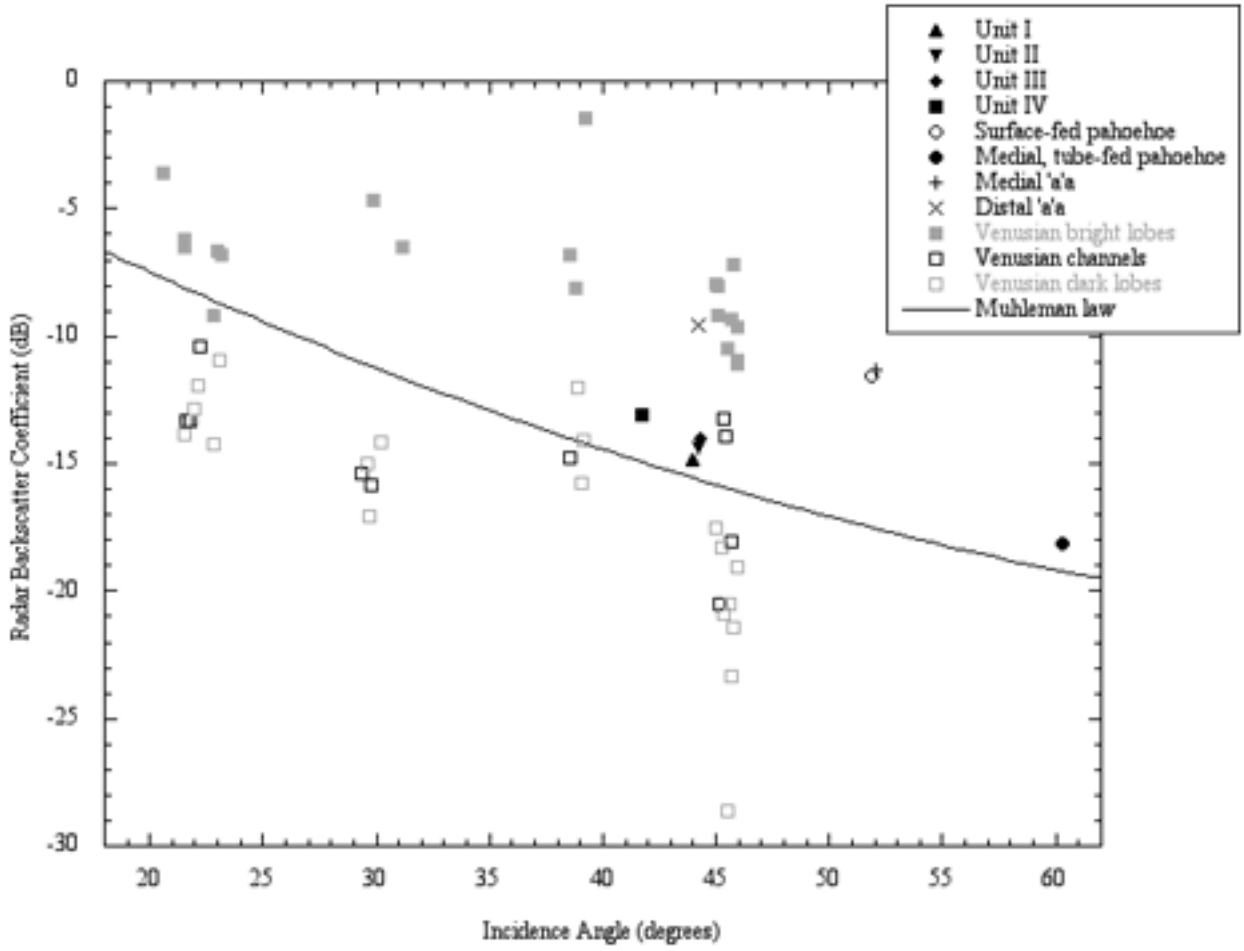

Figure 5.9. Comparison of AIRSAR interpolated SHH data with Venusian SHH data of Byrnes and Crown [2002].

5.5.5. Significance

The Mauna Ulu surface units examined in this study display differences in mean backscatter coefficients over a ~20° range of mean incidence angles (Figures 5.8-5.9). Because the dielectric constant of the Mauna Ulu basalt flows should be relatively constant, differences in radar backscatter may reasonably be expected to result from differences in surface roughness (at the scale of the radar wavelength) and incidence angle. It should be noted that incidence angle is important locally (relative to the radar wavelength) rather than at the larger scale at which incidence angle is normally measured; incidence angle is commonly measured relative to a DEM, such as for TOPSAR, or relative to a spheroid, such as for Magellan. This is significant with respect to inflation. Small-scale inflation will produce small surface fractures that will increase the overall radar roughness of a unit, whereas large-scale inflation may turn up large slabs that will act as local very-low-incidence surface facets (corner reflectors) if oriented properly with respect to the direction of radar illumination.

For Venus, a simple empirical relationship between radar backscatter and incidence angle was formulated by Muhleman [1964]. The "Muhleman law" (Figure 5.9) represents the average Venus surface with respect to incidence angle [see also Pettengill et al., 1988; Ford and Plaut, 1993; Campbell, 1995]. Terrestrial volcanic surfaces imaged at multiple radar incidence angles do not display this simple relationship [e.g. Plaut, 1991; Plaut et al., 2002; see Figure 5.8]. Given the overall trend of radar backscatter vs. incidence displayed in Figure 5.8, it is likely that the medial tube-fed pahoehoe is more comparable (but still lower) in roughness to unit I. The remaining difference in surface roughness may be due to less inflation and mixed-unit pixels. In general, inflation is less above Holei and Poliokeawe Pali, which translates to lower backscatter coefficients. Also, because the pahoehoe surface unit exposures within the Mauna Ulu flow field

are typically smaller than the 5 m/pixel AIRSAR resolution, it is expected that the mean values calculated in this study average together multiple surface units. The tube-fed pahoehoe in the medial portion of the flow field above Holei and Poliokeawe Pali (Figure 5.1) is composed of superposed sheets with small, relatively sparse tumuli, so AIRSAR pixels sample a more homogeneous surface than that below Holei Pali, where unit I sheets are adjacent to unit II and III toes, unit IV channels, and lobes of 'a'a. Units I-III have similar mean backscatter coefficients and incidence angles, although field observations and measurements (Table 5.1) suggest that unit III is actually rougher than is indicated by Figure 5.8 and that the unit III backscatter coefficient averaged in smoother (unit I and II) surfaces. Unit IV is expected to likewise have a higher actual surface roughness than the mean value indicates due to mixed pixels. The surface-fed pahoehoe is significantly rougher than the other pahoehoe examined herein. Field observations suggest that this radar signature is due to rough, fractured shelly pahoehoe (Figure 5.6) and the presence of corner reflectors, such as walls of drained, fountain-fed channels (Figure 5.7). The medial and distal 'a'a pixels represent the roughest surfaces examined in this study. Although the difference in backscatter coefficients between the medial and distal portions of the 1969 'a'a lobe is exaggerated by the difference in incidence angle, the data suggests that the 'a'a flow surface was increasingly disrupted as the lobe advanced.

The similarity in radar backscatter (with respect to incidence angle) of the surface units examined herein and the basaltic lava flow surfaces examined by Plaut [1991] and Plaut et al. [2002] suggests that these surfaces are representative of Hawaiian subaerial basalt flows. The significantly wider range of backscatter coefficients displayed by the Venusian flow fields examined by Byrnes and Crown [2002] indicates that those flows were emplaced over a wider range of conditions and/or subject to a greater range of post-emplacement modification. Given

that the resolution of the Magellan SAR data is ~100 m/pixel, pixels represent significantly larger areas than the AIRSAR pixels and therefore pixels are expected to be correspondingly more mixed. This suggests that the Venusian flows display an even greater range of surface roughness than is indicated by the data (Figure 5.9 and Byrnes and Crown [2002]). The range of surface roughness for Venusian flows is also interesting because of the suggested correlation between radar brightness and flow rheology. Specifically, it was observed that relatively radar-bright flows tend to be thicker and less responsive to underlying topography. This is consistent with radar-bright terrestrial 'a'a flows, which tend to be thick, have a high flow viscosity, and be less responsive to underlying topography relative to pahoehoe flows.

5.6. Discussion

The surface units examined herein display differences in fracturing of the surface crust that is largely related to flow inflation and which affects radar backscatter. The units also display differences in radar backscatter coefficients related to surface roughness. Because unmodified surface crusts of pahoehoe units I, II, and III tend to be smooth at the dm-scale and increased inflation of the units corresponds to increasing backscatter coefficients, it is suggested that inflation fractures are largely responsible for the radar roughness of these three surface units. Unit IV and 'a'a are rough due to surface disruption that had occurred during flow, and shelly pahoehoe is rough due to collapse of the surface crust. The fact that unit IV and 'a'a surfaces display higher mean backscatter coefficients than unit III, but unit III has a higher measured average maximum relief than either of those units (Table 5.1), suggests that the radar backscatter is dominated by the average roughness of the unit rather than the most significant roughness

element within a pixel. For this reason, backscatter coefficients of mixed pixels are expected to represent an average of the surfaces sampled rather than being dominated by relatively smooth or rough units. Larger pixels will typically sample more unit surfaces, so it is expected that, for a given area, the range of backscatter coefficients will be reduced as the data resolution is degraded. Given the nature of mixed pixels, it is unlikely that radar data will be able to distinguish the suite of surfaces in a compound flow field produced by a range of primary emplacement morphologies that have been modified to various extents.

Radar is useful for constraining the range of possible surfaces that are present within a flow field, and may be used with morphologic information to provide reasonable interpretations for emplacement of units that are much larger than the pixel size. Furthermore, radar may be used to constrain the extent of inflation within the flow field if independent information about primary morphologies is available, such as from visible-wavelength remote sensing data.

Several important implications for Venusian lava flow fields may be derived from these analyses. Because radar backscatter appears to be dominated by the average unit roughness, the Venusian backscatter coefficients are most likely representative of typical flow surfaces rather than spatially-limited roughness elements within each pixel. Since the footprint of individual Magellan pixels is relatively large, it is likely that they commonly sample multiple lava surfaces. This suggests that the range of surface roughness for Venusian lava flows is even greater than that indicated by Figure 5.9 (Byrnes and Crown [2002]) and other investigators [e.g. Campbell and Campbell, 1992, Campbell and Rogers, 1994]. Furthermore, the significance of secondary modification (in the forms of inflation and remobilization) on radar backscatter suggests that these processes may be significant on Venus as well. Such secondary disruption may be a mechanism by which very smooth-surfaced (low backscatter coefficient) flow units are modified

to produce significantly rougher surfaces, yielding a wide range of radar signatures. This is consistent with the observation of Byrnes and Crown [2002] that radar-dark Venusian flows are most common in proximal regions, and the field observation reported herein that Mauna Ulu proximal flow units tend to lack inflation features. The difference in proximal flow-unit backscatter coefficients displayed at Mauna Ulu and the Venusian complexes is attributed to the role of exsolved gas, which produces fountain-fed flows and gas-charged shelly pahoehoe in the terrestrial subaerial environment and is not expected to be significant in the high-atmospheric-pressure environment of Venus [e.g. Head and Wilson, 1986]. Addressing why flows on Venus may have experienced greater degrees of modification than terrestrial flows requires further modeling.

5.7. Conclusions

The surface units examined in this study display a wide range in the three related parameters fracturing, inflation, and dm- to m-scale topography, reflecting differences in local supply of lava within the Mauna Ulu lava tube system during and after emplacement of the units. The small-scale (mm to cm) characteristics of the units are related to the larger-scale (dm to m) characteristics in that areas that had been subject to a greater degree of inflation tend to display more extensive spallation of the flow crust and more significant fracturing and offset of the unit surface. The units display inflation and fracturing at a variety of scales. The average maximum relief measured at the selected sites increases from unit I (29 cm) and unit II (32 cm) to unit IV (55 cm) and 'a'a (56 cm) to unit III (72 cm). Observations were also made of surface-fed pahoehoe and indicate that these units are typically not inflated. The maximum relief associated

with shelly pahoehoe units (commonly several dm) is typically related to collapse of the surface crust, whereas the maximum relief of fountain-fed pahoehoe is predominantly controlled by the unit morphology and may be >2 m for drained lava channels.

The surface units examined herein also display a range of mean backscatter coefficients related to differences in radar roughness (cm- to dm-scale) and larger (m-scale) roughness elements that serve as corner reflectors. The differences in radar backscatter between the various units is attributed to differences in flow disruption of the surface during emplacement, flow unit inflation during and following emplacement, and collapse of the unit following emplacement. The radar data, supported by the field observations, indicate that the flow units increase in roughness from unit I, followed successively by unit II, unit III, unit IV, surface-fed pahoehoe, medial 'a'a, and finally distal 'a'a . The correlation observed in the field between small-scale (mm to cm) and larger-scale (dm to m) roughness is also evident in the AIRSAR radar data relative to the ASTER and MASTER thermal infrared data previously reported [Byrnes et al., 2002], supporting the correlation between lava flow inflation and crust spallation. Given the resolution of AIRSAR vs. Magellan data and the nature of mixing of radar signatures from various unit surfaces, the Venusian lava flow fields examined previously by Byrnes and Crown [2002] are composed of flows that were likely emplaced over a wider range of conditions and/or subject to a greater range of post-emplacement modification than terrestrial flows. This suggests that, despite gross morphologic similarities between terrestrial and Venusian flow lobes, simple models of the development of lava flow fields on Venus that are based on terrestrial subaerial basalt flow fields may not be sufficient. Furthermore, the ambiguity related to superposition relationships discernible in the radar data indicates that care is required in interpreting stratigraphy on Venus.

Chapter 6

Summary and Conclusions

This dissertation presents an examination of lava emplacement processes that has been carried out in order to understand the development of lava flow fields in different planetary settings. The work was accomplished through the detailed characterization of surface units within flow fields. The development of a compound flow field has been found to be extremely complex, being influenced by factors that characterize a given eruptive event (such as eruption temperature, lava composition, and the rate, history, and duration of supply) and factors that affect emplacement locally (such as topography and substrate, and the cooling, vesiculation, degassing, and crystallization history of the lava). After initial formation of the surface crust, flow units may be modified over a range of scales, by processes such as inflation, crust spallation and collapse, and unit remobilization, yielding a wide range of surfaces. The Mauna Ulu compound flow field and five Venusian lava flow fields (Turgmam Fluctus, Zipaltonal Fluctus, the Tuli Mons/Uilata Fluctus flow complex, the Var Mons flow field, and Mylitta Fluctus) have been examined and compared in order to understand volcanic resurfacing on the Earth and Venus.

An initial study [Byrnes and Crown, 2001] defined four varieties of tube-fed pahoehoe, which represent different emplacement histories and can be identified in the field and remote sensing datasets based on color, surface texture (roughness and presence or lack of glassy crust), and morphology. The distribution of these units, mapped using an automated supervised classification technique, indicates a contrast in complexity between flow field margins and interiors. Flow field margins are dominated by lobate sheets (unit I) and toe networks (unit II). Flow field interiors show the full range of unit morphologies and textures identified because

sheet and toe flow regimes occur (producing units I and II), flow may be concentrated enough to form channels (unit IV), and these regions may serve as storage areas for later breakouts (unit III). These units show a limited correlation to pre-Mauna Ulu topography based on the mean slopes calculated. Unit IV disrupted surfaces typically associated with channels occur on steeper pre-eruption slopes than the sheets and toe networks of units I and II. Factors other than topography also affect surface unit emplacement, however, such as storage within the subsurface distributary network that may later feed viscous late-stage units (unit III). The overall distribution of surface units within the study area is not directly related to the largest scale of lava tubes previously mapped.

The initial study was extended using additional field investigations with spaceborne and airborne visible and thermal-infrared remote sensing datasets covering the whole Mauna Ulu flow field. This study characterized the small-scale (mm to cm) nature of tube-fed pahoehoe (units I-IV), surface-fed pahoehoe (shelly and fountain-fed), 'a'a, and transitions between these units. Based on field observations, visible-wavelength characteristics of the surface units are dependent on the color, abundance of glassy surface crust, and nature of dm-scale undulations and larger-scale irregularities. Emissivity (derived from thermal-infrared data) reflects variations in glass abundance and small-scale roughness and may be used to calculate the abundance of small-scale surface roughness elements (such as vesicles), which is related to the thermal and degassing history of the lava. The wide range in characteristics observed in the field may be used to infer flow regimes and cooling histories and indicate that each of the units may be produced under a range of conditions, consistent with the gradational nature of the units observed within the flow field. Extending the initial study to the entire flow field also allowed for characterization of various regions within the flow field. The proximal region is

characterized by surface-fed shelly and fountain-fed pahoehoe that is relatively homogeneous, except for those flows nearest the vent that are subjected to alteration due to continued degassing. These units are emplaced as large sheets and toes and signify relatively high lava supply rates. Medial and distal portions of the flow field display 'a'a and tube-fed pahoehoe. 'A'a becomes more common in association with the steep pali, due to the increased lava strain rate caused by increased flow velocity. Tube-fed pahoehoe is emplaced as sheets, toes, and channels that display different small-scale surface characteristics due to differences in cooling, degassing, and crystal formation and/or settling. Tube-fed pahoehoe units (I-IV) display an overall trend of increased small-scale surface roughness toward the flow field margins and away from the vent, suggested to result from cooling and flow disruption.

To provide a planetary comparison to the Mauna Ulu flow field, analyses of the morphology, stratigraphy, and surface roughness properties of five Venusian lava flow fields were conducted using Magellan SAR data to investigate flow field emplacement processes and the development of volcanic centers. The flow fields are large (~80,000 to 820,000 km^2 vs. ~61 km^2 for Mauna Ulu), display digitate morphologies, and exhibit shallow slopes. Flow field surfaces display complex patterns due to emplacement of abundant, typically radar-dark channels and numerous radar-dark, -intermediate, and -bright lobes of various sizes and planform morphologies. Flow field surfaces tend to show the greatest variation in radar brightness within proximal regions, and surfaces of individual lobes within the flow fields may display uniform or varied radar brightness. At the Magellan wavelength (12.6 cm) and FMAP pixel size (75 m/pixel), individual flow lobes are similar or smoother than terrestrial lava flows. The Venusian flow fields display similarities in radar backscatter patterns and planform morphologies to terrestrial lava flow fields, although the larger scale and larger range in surface roughness of

Venusian features suggest that simple analogies may not be sufficient. The flow fields appear to have developed through emplacement of both simple and compound flow lobes, based on lobe morphologies and branching patterns. In addition to surface-fed lava extending directly from vent regions, the presence of tube-fed flows is suggested by distributary morphologies from local sources within the flow fields and the presence of discontinuous channels. Flow inflation may have also occurred within medial and distal portions of some flow fields, as lobes displaying discrete zones of increased radar brightness are observed. Alternatively, these zones may be attributed to differences in emplacement conditions across a flow lobe. The flow fields display a variety of lobe and channel morphologies, characterized by variations in branching, surface roughness patterns, and margin sinuosity. Channels commonly show radar-dark surfaces with adjacent radar-bright levees. Several lines of evidence suggest that flow lobes within the five selected flow fields are relatively thin (less than a few tens of meters). Some correlation appears to be present between radar brightness and planform morphology, flow thickness, and insensitivity to underlying topography, suggesting that increased radar backscatter may be indicative of higher flow viscosities, although post-emplacement modification (such as by flow inflation) complicates this relationship. The uppermost flow surfaces are among the youngest geologic units locally, although complicated superposition relationships within the flow fields and with associated features (such as shields, domes and coronae) suggest the volcanic centers were developed over protracted durations.

Finally, a field and remote sensing study of the Mauna Ulu flow field was conducted in order to characterize radar signatures of surface units that could be correlated with ground observations. This study provides a complementary approach to the work presented in chapter 3 [Byrnes et al., 2002] for the purposes of data fusion, as well as a more direct means to compare

Mauna Ulu with the Venusian flow fields examined in chapter 4 [Byrnes and Crown, 2002]. The Mauna Ulu surface units were found to display a wide range in fracturing and inflation over a variety of scales, reflecting differences in local supply of lava within the Mauna Ulu lava tube system during and after emplacement of the units, and were also found to display a wide range of dm- to m-scale topography, reflecting primary emplacement morphologies and the influence of secondary modification. Small-scale (mm to cm) characteristics of the units are related to the larger-scale (dm to m) characteristics in that areas that had been subject to a greater degree of inflation tend to display more extensive spallation of the flow crust and more significant fracturing and offset of the unit surface. The range of cm- to m-scale topography is reflected in the differences in radar backscatter coefficients between the various units and is found to result from differences in disruption during flow, flow inflation, and surface collapse after emplacement. Given the resolution of AIRSAR vs. Magellan data and the nature of mixing of radar signatures from various unit surfaces, the Venusian lava flow fields examined previously by Byrnes and Crown [2002] are composed of flows that were likely emplaced over a wider range of conditions and/or subject to a greater range of post-emplacement modification than terrestrial flows.

Future work may further characterize the nature of volcanic deposits on rocky bodies in the solar system. Incorporation of terrestrial subaerial basaltic andesite and andesite will provide a compositional comparison to Hawaiian basalt flows, and incorporation of submarine basalt flows will provide a high-pressure, low-temperature example to serve as an intermediate between terrestrial subaerial flows and flows on Venus. Examination of volcanic deposits on Mars and Io will provide yet a wider range of planetary environments, as will examination of ancient

terrestrial komatiite flows. Finally, study of other varieties of volcanic deposits will provide a more holistic understanding of volcanism, a fundamental process in the solar system.

APPENDICES

Appendix A

Mauna Ulu study site locations

Sites listed in this appendix were geolocated using a Trimble differential Global Plositioning System (dGPS) to achieve ~10 cm accuracy. Refer to chapters 3 and 5 for additional information concerning the sites. Positions are reported in Eastings and Northings relative to a UTM zone 5 (North) projection, on a WGS84 spheroid.

Table A1. Mauna Ulu study site locations

location	site
274152.5 E, 2135702.5 N	3.1.a, unit II
274167.0 E, 2135682.0 N	3.1.b, unit III
274162.0 E, 2135684.5 N	3.1.b1, unit II (inlier to site 3.1.b)
274148.5 E, 2135724.5 N	3.1.c, unit IV
274134.0 E, 2135747.0 N	3.1.c1, unit II (inlier to site 3.1.c)
274152.0 E, 2135657.5 N	3.1.d, unit I
274130.5 E, 2135587.0 N	3.2.a, unit I
274204.5 E, 2135497.5 N	3.3.b, unit IV
274902.0 E, 2136061.0 N	3.7, unit III
274896.5 E, 2136003.5 N	3.9, unit III
274976.5 E, 2135840.5 N	3.12, 'a'a leveed channel
273191.0 E, 2135503.0 N	4.2, unit III (tumulus)
273241.0 E, 2135329.5 N	4.3, unit III
273231.5 E, 2135347.5 N	4.4, unit III
273251.0 E, 2135313.0 N	4.5, unit III
273059.0 E, 2134343.5 N	4.13, unit III
273012.5 E, 2134101.0 N	4.17, 'a'a and unit IV
268470.5 E, 2139543.0 N	5.1.a, unit II
274436.5 E, 2133929.0 N	6.1.a, unit I and II
274474.0 E, 2133868.5 N	6.2.a, P-type (blue-glassy) pahoehoe

Table A1. (continued)

location	site
272427.5 E, 2133669.5 N	6.3.a, unit I
272399.5 E, 2133706.0 N	6.3.b, unit III
272435.0 E, 2133572.5 N	6.4.a, unit I
272428.0 E, 2133519.0 N	6.5.a, unit I
272088.5 E, 2137709.5 N	7.1.a, unit I
271941.0 E, 2137664.5 N	7.1.a, unit III
271935.5 E, 2137652.0 N	7.1.a, unit III
271931.5 E, 2137661.0 N	7.1.a, unit II
271851.0 E, 2138156.0 N	7.2.a, unit I
271539.0 E, 2137380.5 N	7.3.a, unit I
271387.0 E, 2137336.0 N	7.4.a, unit II
271441.5 E, 2137129.5 N	7.5.a, unit IV
271489.5 E, 2136942.5 N	7.6.a, unit I
271628.0 E, 2136818.5 N	7.7.a, unit II
271526.0 E, 2136722.5 N	7.8.a, unit IV

Appendix B

Magellan radar calibration

Relative to the Muhleman [1964] empirically derived model, the backscatter coefficient (σ_0) of a pixel with a given DN may be calculated (in dB) by:

(1) $\sigma_0 = 0.2\ (DN - 101)$ [Ford and Plaut 1993, Campbell 1995]

To obtain the absolute backscatter coefficient, the above value must be adjusted by the addition of the following term, where q is incidence angle (in degrees):

(2) $$\frac{0.0118 \cos(\theta + 0.5)}{[\sin(\theta + 0.5) + 0.111 \cos(\theta + 0.5)]^3}$$ [Ford and Plaut 1993]

or, expressed in dB:

(3) $$10 \log \left(\frac{0.0118 \cos(\theta + 0.5)}{[\sin(\theta + 0.5) + 0.111 \cos(\theta + 0.5)]^3} \right)$$ [Campbell 1995]

yielding, from (3) and (1):

(4) $$\sigma_0 = 0.2\ (DN - 101) + 10 \log \left(\frac{0.0118 \cos(\theta + 0.5)}{[\sin(\theta + 0.5) + 0.111 \cos(\theta + 0.5)]^3} \right)$$

To apply this correction, the incidence angle is required for each pixel. Since incidence of the Magellan SAR is a function of latitude, image mosaics may be calibrated by applying a line-by-line correction. Incidence angle vs. latitude is provided at 1° latitude increments by Campbell [1995]. A second-order polynomial was fit to incidence vs. latitude (Φ) data for the latitude range covered by each image mosaic in this study, such that:

(5) $\theta = A\Phi^2 + B\Phi + C$

where A, B, and C are constants.

A linear scaling was used to obtain the latitude of each line in each image mosaic:

(6) $\Phi = (y/y_{max})\ (S-N) + (N)$

where y is the line number (starting at y=0), y_{max} is the maximum line number in the image, S is the southernmost latitude in the image, N is the northernmost latitude in the image, and latitudes south of the equator are expressed as negative numbers. Note that this is accurate for sinusoidal projections (as were used for the flow field mosaics in this study), but not all others, such as Mercator projections.

BIBLIOGRAPHY

Bibliography

Anderson, S.W., E.R. Stofan, S.E. Smrekar, J.E. Guest, and B. Wood, Pulsed inflation of pahoehoe lava flows: Implications for flood basalt emplacement, Earth Planet. Sci. Lett., 168, 7-18, 1999.

Baloga, S.M., and D.A. Crown, A stochastic approach to the emplacement of pahoehoe lava flows, Lunar Planet. Sci. Conf. XXVI, 69-70, 1995.

Baloga, S.M., and L.S. Glaze, Pahoehoe transport as a correlated random walk, Lunar Planet. Sci. Conf. XXXI, Abstract #1272, Lunar and Planetary Institute, Houston (CD-ROM), 2000.

Basilevsky, A.T., and J.W. Head, Global stratigraphy of Venus: Analysis of a random sample of thirty-six test areas, Earth, Moon, Planets, 66, 285-336, 1995.

Basilevsky, A.T., and J.W. Head, Geologic units on Venus: Evidence for their global correlation, Planet. Space Sci., 48, 75-111, 2000.

Brian, A.W., E.R. Stofan, and J.E. Guest, A new topographic rise on Venus: Characteristics and implications, Lunar Planet. Sci. Conf. XXX, Abstract #1579, Lunar and Planetary Institute, Houston (CD-ROM), 1999.

Bridges, N.T., Ambient effects on basalt and rhyolite lavas under Venusian, subaerial, and subaqueous conditions, J. Geophys. Res., 102, 9243-9255, 1997.

Bruno, B.C., and G.J. Taylor, Morphologic identification of Venusian lavas, Geophys. Res. Lett., 22, 1897-1900, 1995.

Bruno, B.C., G.J. Taylor, S.K. Rowland, P.G. Lucey, and S. Self, Lava flows are fractals, Geophys. Res. Lett., 19, 305-308, 1992.

Bruno, B.C., G.J. Taylor, S.K. Rowland, and S.M. Baloga, Quantifying the effect of lava rheology on lava-flow margins using fractal geometry, Bull. Volcanol., 56, 193-206, 1994.

Bulmer, M.H., and J.E Guest, Modified domes and associated debris aprons on Venus, in W.J. McGuire, A.P. Jones, and J. Neuberg (eds.), Volcano Instability on the Earth and Other Planets, Geol. Soc. Special Pub. 110, 349-371, 1996.

BVSP (Basaltic Volcanism Study Project), Basaltic volcanism on the terrestrial planets, Pergamon Press, New York, 1286 pp., 1981.

Byrnes, J.M., and D.A. Crown, Characteristics and distribution of pahoehoe units in the Mauna Ulu compound flow field, Lunar Planet. Sci. Conf. XXIX, Abstract #1455, Lunar and Planetary Institute, Houston (CD-ROM), 1998.

Byrnes, J.M., and D.A. Crown, Relationships between pahoehoe surface texture, topography, and lava tubes at Mauna Ulu, Kilauea Volcano, Hawai'i, Lunar Planet. Sci. Conf. XXX, Abstract #1298, Lunar and Planetary Institute, Houston (CD-ROM), 1999.

Byrnes, J.M., and D.A. Crown, Relationships between pahoehoe surface texture, topography, and lava tubes at Mauna Ulu, Kilauea Volcano, Hawai'i, J. Geophys. Res., 106, 2139-2151, 2001.

Byrnes, J.M., and D.A. Crown, Morphology, stratigraphy, and surface roughness properties of Venusian lava flow fields, J. Geophys. Res., in press, 2002.

Byrnes, J.M., D.A. Crown, and M.S. Ramsey, Thermal remote sensing characteristics of basaltic lava flow surface units: Implications for flow field evolution, Lunar Planet. Sci. Conf. XXXI, Abstract #1867, Lunar and Planetary Institute, Houston (CD-ROM), 2000.

Byrnes, J.M., M.S. Ramsey, and D.A. Crown, Emplacement of the Mauna Ulu flow field (Kilauea Volcano, Hawai'i): New insights from integrated field and remote sensing analyses, submitted to J. Volcanol. Geotherm. Res., 2002.

Campbell, B.A., Use and presentation of Magellan quantitative data in Venus mapping, U.S. Geol. Surv. Open-File Report 95-519, 1995.

Campbell, B.A., and D.B. Campbell, Analysis of volcanic surface morphology on Venus from comparison of Arecibo, Magellan, and terrestrial airborne radar data, J. Geophys. Res., 97, 16,293-16,314, 1992.

Campbell, B.A., and P.G. Rogers, Bell Regio, Venus: Integration of remote sensing data and terrestrial analogs for geologic analysis, J. Geophys. Res., 99, 21,153-21,171, 1994.

Campbell B.A., and M.K. Shepard, Lava flow surface roughness and depolarized radar scattering, J. Geophys. Res., 101, 18,941-18,951, 1996.

Campbell, B.A., R.E. Arvidson, and M.K. Shepard, Radar polarization of volcanic and playa surfaces: Applications to terrestrial remote sensing and Venus data interpretation, J. Geophys. Res., 98, 17,099-17,113, 1993.

Cashman, K.V., and J.P. Kauahikaua, Reevaluation of vesicle distributions in basaltic lava flows, Geology, 25, 419-422, 1997.

Crown, D.A., and S.M. Baloga, Pahoehoe toe dimensions, morphology, and branching relationships at Mauna Ulu, Kilauea Volcano, Hawai'i, Bull. Volcanol., 61, 288-305, 1999.

Crown, D.A., E.R. Stofan, and J.J. Plaut, Geology of the Guinevere Planitia quadrangle of Venus, Lunar Planet. Sci. Conf. XXV, 301-302, 1994.

Crown, D.A., J.M. Byrnes, and S.M. Baloga, Scale-dependent characteristics of Mauna Ulu pahoehoe flows, Lunar Planet. Sci. Conf. XXIX, Abstract #1376, Lunar and Planetary Institute, Houston (CD-ROM), 1998.

Crown, D.A., S.M. Baloga, and J.M. Byrnes, Emplacement of pahoehoe flow fields: Scale-dependent characteristics of Mauna Ulu flows, Lunar Planet. Sci. Conf. XXX, Abstract #1379, Lunar and Planetary Institute, Houston (CD-ROM), 1999.

Crown, D.A., J.M. Byrnes, and M.S. Ramsey, Mapping compound lava flow fields on planetary surfaces, EOS (Trans. Amer. Geophys. Union), suppl. 62, Abstract P32D-0566, 2001.

Crown, D.A., J.M. Byrnes, and S.M. Baloga, Scale-dependent characteristics of Mauna Ulu pahoehoe flows, in preparation, 2002a.

Crown, D.A., E.R. Stofan, and J.J. Plaut, Geologic map of the Guinevere Planitia Quadrangle (V-30), Venus, U.S. Geological Survey, in preparation, 2002b.

Ford, J.P., and J.J. Plaut, Magellan image data, in J.P. Ford, J.J. Plaut, C.M. Weitz, T.G. Farr, D.A. Senske, E.R. Stofan, G. Michaels, and T.J. Parker (eds.), Guide to Magellan Image Interpretation, JPL Publication 93-24, 7-18, 1993.

Francis, P., Volcanoes: A planetary perspective, Oxford University Press, New York. 443 pp., 1993.

Gaddis, L., P. Mouginis-Mark, R. Singer, and V. Kaupp, Geologic analyses of Shuttle Imaging Radar (SIR-B) data of Kilauea Volcano, Hawai'i, Geol. Soc. Am. Bull., 101, 317-332, 1989.

Gaddis, L.R., P.J. Mouginis-Mark, and J.N. Hayashi, Lava flow textures: SIR-B radar image texture, field observations, and terrain measurements, Photogram. Eng. Remote Sensing, 56, 211-224, 1990.

Gillespie, A.R., M.O. Smith, J.B. Adams, and S.C. Willis, Spectral mixture analysis of multispectral thermal infrared images, in E.A. Abbott (ed.), Proc. Sec. Therm. Infrared Multispectral Scanner (TIMS) Workshop, Jet Propulsion Lab. Pub. 90-55, 57-74, 1990.

Godinot, A., Comment on "Pipe vesicles in Hawaiian basaltic lavas: Their origin and potential as paleoslope indicators," Geology, 16, 90, 1988.

Greeley, R., Observations of actively forming lava tubes and associated structures, Hawai'i, Modern Geology, 2, 207-223, 1971.

Greeley, R., and L. Martel, Radar observations of basaltic lava flows, Craters of the Moon, Idaho, Int. J. Remote Sensing, 9, 1071-1085, 1988.

Guest, J.E., and E.R. Stofan, A new view of the stratigraphic history of Venus, Icarus, 139, 55-66, 1999.

Guest, J.E., C.R.J. Kilburn, H. Pinkerton, and A. Duncan, The evolution of flow fields: Observations of the 1981 and 1983 eruptions of Mount Etna, Sicily, Bull. Volcanol., 49, 527-540, 1987.

Guest, J.E., M.H. Bulmer, J. Aubele, K. Beratan, R. Greeley, J.W. Head, G. Michaels, C. Weitz, and C. Wiles, Small volcanic edifices and volcanism in the plains of Venus, J. Geophys. Res., 97, 15,949-15,966, 1992.

Head, J.W., and L. Wilson, Volcanic processes and landforms on Venus: Theory, predictions, and observations, J. Geophys. Res., 91, 9407-9446, 1986.

Head, J.W., L.S. Crumpler, J.C. Aubele, J.E. Guest, and R.S. Saunders, Venus volcanism: Classification of volcanic features and structures, associations, and global distribution from Magellan data, J. Geophys. Res., 97, 13,153-13,197, 1992.

Head, J.W., K.M. Roberts, L. Wilson, and H. Pinkerton, Lava flow-field morphological classification and interpretation: Examples from Venus, Lunar Planet. Sci. Conf. XXIV, 627-628, 1993.

Holcomb, R.T., Preliminary map showing products of eruptions, 1962-1974 from the upper east rift zone of Kilauea Volcano, Hawai'i, U.S. Geol. Surv. Misc. Field Studies, Map MF-811, scale 1:24,000, 1976.

Holcomb, R.T., Eruptive history and long-term behavior of Kilauea Volcano, in R.W. Decker, T.L. Wright, and P.H. Stauffer (eds.), Volcanism in Hawai'i, U.S. Geol. Surv. Prof. Pap. 1350, 261-350, 1987.

Hon, K., J. Kauahikaua, R. Denlinger, and K. Mackay, Emplacement and inflation of pahoehoe sheet flows: Observations and measurements of active lava flows on Kilauea Volcano, Hawai'i, Geol. Soc. Am. Bull., 106, 351-370, 1994.

Hook, S.J., A.R. Gabell, A.A. Green, and P.S. Kealy, A comparison of techniques for extracting emissivity information from thermal infrared data for geologic studies, Remote Sens. Environ., 42, 123-135, 1992.

Hook, S.J., J.J. Myers, K.J. Thome, M. Fitzgerald, and A.B. Kahle, The MODIS/ASTER airborne simulator (MASTER) – a new instrument for Earth science studies, Remote Sens. Environ., 76, 93-102, 2001.

Hutchinson, M.F., Calculation of hydrologically sound digital elevation models, Third International Symposium on Spatial Data Handling, Sydney, Columbus, Ohio, International Geographical Union, 1988.

Hutchinson, M.F., A new procedure for gridding elevation and stream line data with automatic removal of spurious pits, J. Hydrology, 106, 211-232, 1989.

Hutchinson, M.F., A locally adaptive approach to the interpolation of digital elevation models, Proc., Third International Conference/Workshop on Integrating GIS and Environmental Modeling, Santa Fe, NM, January 21-26, 1996, Santa Barbara, C.A., National Center for Geographic Information and Analysis, 1996.

Johnson, J.R., and V.R. Baker, Surface property variations in Venusian fluidized ejecta blanket craters, Icarus, 11, 33-70, 1994.

Jones, J.G., Pillow lava and pahoehoe, J. Geology, 76, 485-488, 1968.

Jones, J.G., Pillow lava and pahoehoe: A reply, J. Geology, 77, 732-734, 1969.

Kahle, A.B., and R.E. Alley, Separation of temperature and emittance in remotely sensed radiance measurements, Remote Sens. Environ., 42, 107-111, 1992.

Kahle, A.B., A.R. Gillespie, E.A. Abbott, M.J. Abrams, R.E. Walker, G. Hoover, and J.P. Lockwood, Relative dating of Hawaiian lava flows using multispectral thermal infrared images: A new tool for geologic mapping of young volcanic terranes, J. Geophys. Res., 93, 15,239-15,251, 1988.

Kauahikaua, J., K.V. Cashman, T.N. Mattox, C.C. Heliker, K.A. Hon, M.T. Mangan, and C.R. Thornber, Observations on basaltic lava streams in tubes from Kilauea Volcano, island of Hawai'i, J. Geophys. Res., 103, 27,303-27,323, 1998.

Keddie, S.T., and J.W. Head, Sapas Mons, Venus: Evolution of a large shield volcano, Earth, Moon, Planets, 65, 129-190, 1994.

Keddie, S.T., and J.W. Head, Formation and evolution of volcanic edifices on the Dione Regio rise, Venus, J. Geophys. Res., 100, 11,729-11,754, 1995.

Keszthelyi, L., and R. Denlinger, The initial cooling of pahoehoe flow lobes, Bull. Volcanol., 58, 5-18, 1996.

Kilburn, C.R.J., Patterns and predictability in the emplacement of subaerial lava flows and flow fields, in R. Scarpa and R.I. Tilling (eds.), Monitoring and Mitigation of Volcano Hazards, Springer-Verlag, Berlin, 491-537, 1996.

Kilburn, C.R.J., and R.M.C. Lopes, The growth of 'a'a lava flow fields on Mount Etna, Sicily, J. Geophys. Res., 93, 14,759-14,772, 1988.

Kirk, R.L., L.A. Soderblom, and E.M. Lee, Enhanced visualization for interpretation of Magellan radar data: Supplement to the Magellan special issue, J. Geophys. Res., 97, 16,371-16,380, 1992.

Kreslavsky, M.A., and R.V. Vdovichenko, Subresolution clinometry with Magellan radar images: Height of lava flow edges on Venus, Lunar Planet. Sci. Conf. XXVIII, 759-760, 1997.

Kruse, F.A., and K.S. Kierein-Young, Mapping lithology and alteration in the northern Death Valley region, California and Nevada, with the Thermal Infrared Multispectral Scanner (TIMS), in E.A. Abbott (ed.), Proc. Sec. Therm. Infrared Multispectral Scanner (TIMS) Workshop, Jet Propulsion Lab. Pub. 90-55, 75-81, 1990.

Lancaster, M.G., J.E. Guest, and K.P. Magee, Great lava flow fields on Venus, Icarus, 118, 69-86, 1995.

Lockwood, J.P., and P.W. Lipman, Holocene eruptive history of Mauna Loa volcano, in R.W. Decker, T.L. Wright, and P.H. Stauffer, (eds.), Volcanism in Hawai'i, U.S. Geol. Surv. Prof. Paper 1350, 509-535, 1987.

Lopes, R.M.C., and C.R.J. Kilburn, Emplacement of lava flow fields: Application of terrestrial studies to Alba Patera, Mars, J. Geophys. Res., 95, 14,383-14,397, 1990.
Macdonald, G.A., Pahoehoe, 'a'a, and block lava, Amer. J. Sci., 251, 169-191, 1953.
Magee, K.P., Formation and emplacement of large-volume flow units on Venus: Implications for the production of flood basalts and evolution of plume-related structures, Ph.D. dissertation, Brown Univ., Providence, RI, 298 pp., 1994.
Magee, K.P., and J.W. Head, Large flow fields on Venus: Implications for plumes, rift associations, and resurfacing, in R.E. Ernst and K.L. Buchan (eds.), Mantle Plumes: Their identification through time, Geol. Soc. Am. Special Paper 352, 81-101, 2001.
Moore, J.G., R.L. Phillips, R.W. Grigg, D.W. Peterson, and D.A. Swanson, Flow of lava into the sea, 1969-1971, Kilauea Volcano, Hawai'i, Geol. Soc. Am. Bull., 84, 537-546, 1973.
Muhleman, D.O., Radar scattering from Venus and the Moon, Astron. J., 69, 34-41, 1964.
Ondrusek, J., P.R. Christensen, and J.H. Fink, Mapping the distribution of vesicular textures on silicic lavas using the Thermal Infrared Multispectral Scanner, J. Geophys. Res., 98, 15,903-15,908, 1993.
Peterson, D.W., and D.A. Swanson, Observed formation of lava tubes, Studies in Speleo., 2, 209-222, 1974.
Peterson, D.W., and R.I. Tilling, Transition of basaltic lava from pahoehoe to 'a'a, Kilauea Volcano, Hawai'i: Field observations and key factors, J. Volcanol. Geotherm. Res., 7, 271-293, 1980.
Pettingill, G.H., P.G. Ford, and B.D. Chapman, Venus: Surface electromagnetic properties, J. Geophys. Res., 93, 14,881-14,892, 1988.
Philpotts, A.R., and C.L. Lewis, Pipe vesicles – An alternate model for their origin, Geology, 15, 971-974, 1987.
Pieri, D., The Advanced Spaceborne Thermal Emission and Reflectance Radiometer (ASTER) global volcanic mapping project, submitted to J. Volcanol. Geotherm. Res., 2002.
Pike, W.A., H.M. Frey, A.E. Krull, E.B. Grosfils, M.S. Gilmore, L.A. Reinen, and S.J. Kozak, Viscosity of Venusian lava flows: Constraints from fractal dimension and chemical composition, Lunar Planet. Sci. Conf. XXIX, Abstract #1055, Lunar and Planetary Institute, Houston (CD-ROM), 1998.
Pinkerton, H., and R.S.J. Sparks, The 1975 sub-terminal lavas, Mount Etna: A case history of the formation of a compound flow field, J. Volcanol. Geotherm. Res., 1, 167-182, 1976.
Pinkerton, H., and L. Wilson, Factors controlling the lengths of channel-fed lava flows, Bull. Volcanol., 56, 108-120, 1994.
Plaut, J.J., Radar scattering as a source of geological information on Venus and Earth, Ph.D. dissertation, Washington Univ., St. Louis, 342 pp., 1991.
Plaut, J.J., and R.E. Arvidson, Comparison of Goldstone and Magellan radar data in the equatorial plains of Venus, J. Geophys. Res., 97, 16,279-16,291, 1992.
Plaut, J.J., S.W. Anderson, D.A. Crown, E.R. Stofan, and J.J. van Zyl, The unique radar properties of silicic lava domes, J. Geophys. Res., in preparation, 2002.
Polacci, M., K.V. Cashman, and J.P. Kauahikaua, Textural characterization of the pahoehoe-'a'a transition in Hawaiian basalt, Bull. Volcanol., 60, 595-609, 1999.
Ramsey, M.S., and P.R. Christensen, Mineral abundance determination: Quantitative deconvolution of thermal emission spectra, J. Geophys. Res., 103, 577-596, 1998.

Ramsey, M.S., and J. Dehn, Spaceborne observations of the 2000 Bezymianny, Kamchatka eruption: The integration of high-resolution ASTER data into near real-time monitoring using AVHRR, submitted to J. Volcanol. Geotherm. Res., 2002.

Ramsey, M.S., and J.H. Fink, Mapping vesicularity of Hawaiian lava flows via thermal infrared remote sensing, Geol. Soc. Am. Cordilleran Sec. Abst. with Progs., 29:5, A58, 1997.

Ramsey, M.S., and J.H. Fink, Estimating silicic lava vesicularity with thermal remote sensing: A new technique for volcanic mapping and monitoring, Bull. Volcanol., 61, 32-39, 1999.

Ramsey, M.S., and L.P. Flynn, Strategies, insights, and the recent advances in volcanic monitoring and mapping with data from the Earth Observing System, submitted to J. Volcanol. Geotherm. Res., 2002.

Realmuto, V.J., Separating the effects of temperature and emissivity: Emissivity spectrum normalization, in E.A. Abbott (ed.), Proc. Sec. Therm. Infrared Multispectral Scanner (TIMS) Workshop, Jet Propulsion Lab. Pub. 90-55, 31-36, 1990.

Realmuto, V.J., K. Hon, A.B. Kahle, E.A. Abbott, and D.C. Pieri, Multispectral thermal infrared mapping of the 1 October 1988 Kupaianaha flow field, Kilauea Volcano, Hawai'i, Bull. Volcanol., 55, 33-44, 1992.

Roberts, K.M., J.E. Guest, J.W. Head, and M.G. Lancaster, Mylitta Fluctus, Venus: Rift-related, centralized volcanism and the emplacement of large-volume flow units, J. Geophys. Res., 97, 15,991-16,015, 1992.

Rosenberg, E., and G.E. McGill, Geologic map of the Pandrosos Dorsa Quadrangle (V-5), Venus, U.S. Geol. Surv. Geol. Invest. Ser. I-2721, scale 1:5,000,000, 2001.

Rossi, M.J., and A. Gudmundsson, The morphology and formation of flow-lobe tumuli on Icelandic shield volcanoes, J. Volcanol. Geotherm. Res., 72, 291-308, 1996.

Rowland, S.K., and G.P.L. Walker, Toothpaste lava: Characteristics and origin of a lava structural type transitional between pahoehoe and 'a'a, Bull. Volcanol., 49, 631-641, 1987.

Rowland, S.K., and G.P.L. Walker, Mafic-crystal distributions, viscosities, and lava structures of some Hawaiian lava flows, J. Volcanol. Geotherm. Res., 35, 55-66, 1988.

Rowland, S.K., and G.P.L. Walker, Pahoehoe and 'a'a in Hawai'i: Volumetric flow rate controls the lava structure, Bull. Volcanol., 52, 615-628, 1990.

Rowland, S.K., M.E. MacKay, H. Garbeil, and P.J. Mouginis-Mark, Topographic analyses of Kilauea Volcano, Hawai'i, from interferometric airborne radar, Bull. Volcanol., 61, 1-14, 1999.

Ruff, S.W., P.R. Christensen, P.W. Barbera, and D.L. Anderson, Quantitative thermal emission spectroscopy of minerals: A laboratory technique for measurement and calibration, J. Geophys. Res., 102, 14,899-14,913, 1997.

Salisbury, J.W., and D.M. D'Aria, Emissivity of terrestrial materials in the 8-14 μm atmospheric window, Remote Sens. Environ., 42, 83-106, 1992.

Saunders, R.S., A.J. Spear, P.C. Allin, R.S. Austin, A.L. Berman, R.C. Chandlee, J. Clark, A.V. DeCharon, E.M. De Jong, D.G. Griffith, J.M. Gunn, S. Hensley, W.T.K. Johnson, C.E. Kirby, K.S. Leung, D.T. Lyons, G.A. Michaels, J. Miller, R.B. Morris, A.D. Morrison, R.G. Piereson, J.F. Scott, S.J. Shaffer, J.P. Slonski, E.R. Stofan, T.W. Thompson, and S.D. Wall, Magellan mission summary, J. Geophys. Res., 97, 13,067-13,090, 1992.

Senske, D.A., G.G. Schaber, and E.R. Stofan, Regional topographic rises on Venus: Geology of Western Eistla Regio and comparison to Beta Regio and Atla Regio, J. Geophys. Res., 97, 13,395-13,420, 1992.

Stofan, E.R., J.E. Guest, and D.L. Copp, Development of large volcanoes on Venus: Constraints from Sif, Gula, and Kunapipi Montes, Icarus, 152,75-95, 2001.

Swanson, D.A., Pahoehoe flows from the 1969-1971 Mauna Ulu eruption, Kilauea Volcano, Hawai'i, Geol. Soc. Am. Bull., 84, 615-626, 1973.

Swanson, D.A., W.A. Duffield, D.B. Jackson, and D.W. Peterson, Chronological narrative of the 1969-1971 Mauna Ulu eruption of Kilauea Volcano, Hawai'i, U.S. Geol. Surv. Prof. Pap., 1056, 1-55, 1979.

Thomson, J.L., and J.W. Salisbury, The mid-infrared reflectance of mineral mixtures (7-14 μm), Remote Sens. Environ., 45, 1-13, 1993.

Tilling, R.I., R.L. Christiansen, W.A. Duffield, E.T. Endo, R.T. Holcomb, R.Y. Koyanagi, D.W. Peterson, and J.D. Unger, The 1972-1974 Mauna Ulu eruption, Kilauea Volcano: An example of quasi-steady-state magma transfer, in R.W. Decker, T.L. Wright, and P.H. Stauffer (eds.), Volcanism in Hawai'i, U.S. Geol. Surv. Prof. Pap. 1350, 405-469, 1987.

Vincent, R.K., and F. Thomson, Spectral compositional imaging of silicate rocks, J. Geophys. Res., 77, 2465-2472, 1972.

Vincent, R.K., F. Thomson, and K. Watson, Recognition of exposed quartz sand and sandstone by two-channel infrared imagery, J. Geophys. Res., 77, 2473-2477, 1972.

Walker, G.P.L., Compound and simple lava flows and flood basalts, Bull. Volcanol., 35, 579-590, 1972.

Walker, G.P.L., Pipe vesicles in Hawaiian basaltic lavas: Their origin and potential as paleoslope indicators, Geology, 15, 84-87, 1987.

Walker, G.P.L., Spongy pahoehoe in Hawai'i: A study of vesicle-distribution patterns in basalt and their significance, Bull. Volcanol., 51, 199-209, 1989.

Walker, G.P.L., Structure, and origin by injection of lava under surface crust, of tumuli, "lava rises", "lava-rise pits", and "lava-inflation clefts" in Hawai'i, Bull. Volcanol., 53, 546-558, 1991.

Walter, L.S., and J.W. Salisbury, Spectral characterization of igneous rocks in the 8- to 12-μm region, J. Geophys. Res., 94, 9203-9213, 1989.

Wentworth, C.K., and G.A. Macdonald, Structures and forms of basaltic rocks in Hawai'i, U.S. Geol. Surv. Bull., 994, 1-98, 1953.

Wilmoth, R.A., and G.P.L. Walker, P-type and S-type pahoehoe: A study of vesicle distribution patterns in Hawaiian lava flows, J. Volcanol. Geotherm. Res., 55, 129-142, 1993.

Wilson, L., and J.W. Head, A comparison of volcanic eruption processes on Earth, Moon, Mars, Io and Venus, Nature, 302, 663-669, 1983.

Yamaguchi, Y., A.B. Kahle, H. Tsu, T. Kawakami, and M. Pniel, Overview of Advanced Spaceborne Thermal Emission Reflectance Radiometer, IEEE Trans. Geosci. Remote Sens., 36, 1062-1071, 1998.

Zebker, H. A., S. N. Madsen, J. Martin, K. B. Wheeler, T. Miller, Y. Lou, G. Alberti, S. Vetrella, and A. Cucci, The TOPSAR interferometric radar topographic mapping instrument, IEEE Trans. Geosci. Remote Sens., 30, 933-940, 1992.

Zebker, H. A., P. Rosen, S. Hensley, and P.J. Mouginis-Mark, Analysis of active lava flows on Kilauea Volcano, Hawai'i, using SIR-C radar correlation measurements, Geology, 24, 495-498, 1996.

Zimbelman, J.R., Flow field stratigraphy surrounding Sekmet Mons volcano, Kawelu Planitia, Venus, EOS (Trans. Amer. Geophys. Union), suppl. 81, Abstract P52A-01, 2000.